RICE UNIVERSITY

Noise Spectroscopy and Electron Transport of Strongly Correlated Materials

by

Dale T. Lowder

A Thesis Submitted
in Partial Fulfillment of the
Requirements for

Doctor of Philosophy

Approved, Committee:

Douglas Natelson, Chair
Professor, Physics and Astronomy
Associate Dean for Research

Ming Yi
Associate Professor, Physics and
Astronomy

Aditya Mohite
Faculty Director, REINVENTS
William M. Rice Trustee Professor,
Chemical and Biomolecular Engineering
Professor, Materials Science and
NanoEngineering, Electrical and
Computer Engineering, and Chemistry

Houston, Texas
August, 2025

Abstract

Electron transport is largely well understood in materials where electron interactions are weak compared to electron motion. However, when electron interactions become dominant in strongly correlated materials, physics becomes significantly more complex, with conventional band theory failing to adequately describe emergent electronic behaviors. Mesoscopic measurements provide unique probes of the electronic properties in these intriguing states, offering insights that complement bulk measurements and theoretical predictions. This thesis discusses two strongly correlated states: heavy fermion Fermi liquids and strange metals. Heavy fermion Fermi liquids are often considered the simpler case within the strongly correlated spectrum, as quasiparticles offer useful quantitative frameworks for analysis despite their dramatically enhanced effective masses. The compounds $YbAl_3$ and $YbRh_2Si_2$ provide excellent platforms for quantitatively probing the coherence of heavy fermion states through magnetotransport measurements. $YbAl_3$ additionally exhibits anomalous low-temperature behavior in the electron-phonon energy loss rate Γ, which is observed through noise spectroscopy techniques that reveal more complicated interactions emerging at low temperatures. $YbRh_2Si_2$ offers the unique capability of probing differences between heavy fermion and strange metal states via magnetic field tunability, allowing for systematic investigation of the quantum phase transition between these exotic phases. Dilution refrigerator measurements of $YbRh_2Si_2$ have the potential to reveal and confirm the abrupt change in quasiparticle coherence through detailed magnetoresistance studies across the boundary between these two states. Further investigation of strange metals is essential for making more universal statements about the sudden reduction in quasiparticle behavior previously reported in strange metal states. To this end, a systematic attempt to fabricate another field-tunable strange metal, $Sr_3Ru_2O_7$, is documented along with practical insights on experimental approaches when work-ing with these exotic and often sensitive materials. Collectively, these mesoscopic transport studies of strongly correlated materials demonstrate the crucial role of detailed electronic measurements in developing a comprehensive understanding of the underlying complex physics that governs these fascinating quantum states.

Acknowledgments

First, I would like to thank my advisor, Dr. Douglas Natelson, for being my mentor throughout my graduate career. Doug has been an excellent mentor and is arguably one of the kindest advisors I have encountered during my tenure at Rice. He is a tremendous source of knowledge and has helped immensely in shaping my approach to thinking about science and physics beyond the scope of my research and laboratory work. For that, I am very grateful to have had Doug as my mentor.

Next, I would like to thank the members of the Natelson group whom I have worked with during my time here. I would like to thank Liyang, Loah, Charlotte, Xuanhan, Xifan, Yunxuan, and Mahdiyeh for training and teaching me when I first joined the lab, especially Liyang, who shared much of his knowledge with me as I began my own research projects. I would also like to thank all the other lab members —Renjie, Shusen, Gage, Kexin, Yuxin, Tanner, and Jiawei— who have helped through conversations and camaraderie throughout my PhD journey.

I would also like to thank all of my collaborators throughout my projects, who have provided both materials and knowledge essential to my research. I am very grateful to the Department of Energy for funding all of my research at Rice. I would also like to express my gratitude to the SEA staff for all there help and insight when it comes to many of the machines required to fabricate all of my devices.

Finally, I would like to thank all my friends whom I have encountered here at Rice. I would like to thank Luis, Diego, Sohail, Mason, Visal, Julian, and Jonathan, who joined the PhD program at the same time as me and maintained friendships throughout our coursework and beyond. I would also like to thank all the other physics friends I have met through Valhalla and various other venues: Collin, Osvaldo, Karthik, Max, Mounica, Dorian, and Ivy. I would also like to thank all of Valhalla for being a great place to meet many new friends and take a step back from the trials and tribulations for some relaxing time bartending and hanging outwith friends. Lastly, I would like to thank anyone and everyone with whom I have had conversations over the past six years, whether about research, hobbies, or just how the week is going. Every single conversation has been helpful in getting to this point in my life, and I appreciate all of you.

Contents

Abstract i

Acknowledgments iii

List of Figures xiv

1 Introduction 1

1.1 Thesis Outline 2

2 Solid State Background 4

2.1 Bulk Conduction 4

2.1.1 Bloch States 6

2.1.2 Phonon States 10

2.2 Length Scales in Metals 14

2.3 Landauer-Büttiker Formalism 16

2.4 Universal Conductance Fluctuations 20

2.5 Weak Localization 21

3 Strongly Correlated Materials 24

3.1 Heavy Fermions 24

3.2 Strange Metal 27

4 Electronic Noise 30

4.1 Thermal Noise 30

4.1.1 Thermal Noise vs. Bias in a Nanowire 33

4.2 **$1/f$** "Flicker" Noise 35

4.3 Shot Noise 38

4.3.1 Single Barrier Tunneling Shot Noise 40

4.3.2 The Fano Factor 42

5 Experimental Methodology **46**

5.1 Device Fabrication 46

5.1.1 Photo/ Electron-beam Lithography 46

5.1.2 Deposition 52

5.1.3 Etching 56

5.2 Resistance Measurements 57

5.2.1 Resistance 58

5.2.2 Van der Pauw Method 61

5.2.3 Cryogenic Systems 63

5.3 Noise Spectroscopy 64

5.3.1 Setup 64

5.3.2 Measurement & Calibration 68

6 Subcoherence Quasiparticle Properties in $\mathbf{YbAl_3}$ Nanostructures **71**

6.1 Device Fabrication 72

6.2 Device Quality Measurements 74

6.3 Magnetoresistance Measurements and Analysis 76

6.4 Johnson Noise Measurements & Analysis 79

6.5 Conclusion 84

7 Observations of Quasiparticle Loss in $\mathbf{YbRh_2Si_2}$ **86**

7.1 Previous Results: Shot Noise Measurements 87

7.1.1 Device Fabrication 88

7.1.2 Shot Noise Results 89

7.2 Current Results 90

7.3 Conclusion 93

8 Misfortunes of $Sr_3Ru_2O_7$ Nanowires **94**

8.1 Standard Fabrication: EBL 96

8.2 Alternative Fabrication 1: Focused Ion Beam 98

8.3 Alternative Fabrication 2: 3D Photolithography 100

8.4 Conclusions and Insights 102

9 Conclusions **103**

Bibliography **105**

A Future Projects **116**

B Noise Data Analysis **119**

C Step-by-Step Noise Data Collection **121**

List of Figures

2.1 1D periodic potential centered on the atoms(ion cores) and spaced by the lattice spacing a 7

2.2 a) Energy dispersion of a free electron. b) Energy dispersion in a crystal lattice showcasing a band gap E_g of forbidden energy values. . 10

2.3 1D chain of atoms connected by springs with a $L = Na$ massless rod connecting the leftmost atom to the rightmost atom fulfilling the Born-von Karman boundary conditions. 11

2.4 1D diatomic chain of atoms with spring constant within the basis being K and the spring constant between bases being G. 12

2.5 Phonon modes of the diatomic 1D chain. The upper branch is the optical phonon and the lower branch is the acoustic phonon 13

2.6 A gold wire. A zoomed in look reveals that it is broken up into ~ 20 nm size grains. Further zoom reveals the grains are composed of face-centered cubic atoms spaced $a \sim 4$ Å 14

2.7 Ballistic conductor with a left and right contact with chemical potentials μ_L and μ_R respectively. The lower plot contains an energy dispersion curve showcasing left-moving and right-moving electrons with colors indicating electrons moving from left to right (red) and right to left (blue). 16

2.8 Fermi-Dirac occupation probability at four different temperatures 0,5,10,20 K with chemical potential $\mu = 10$ meV. As $T \rightarrow 0$, the Fermi function approaches a step function. 17

2.9 Universal conduction data from a $MnBi_2Te_4$ thin film device showcasing overlapping UCF signals. Field swept to the right(left) is indicated by red(black) data. Differences result from altering disorder as field is swept 21

2.10 Diagram showcasing the shape of near zero field a) weak anti-localization magnetoconductance and b) weak localization magnetoconductance. 22

3.1 schematic diagram showcasing the hybridization of the conduction electrons wihtt 4f-electrons in a Kondo lattice. 25

3.2 Diagram showcasing how f-electrons (red) interact with conduction electrons (blue) in the Kondo effect with arrows indicating spin. a) Conduction electrons screen the localized f-electrons magnetic moment above T_K. b) Conduction electrons interact with f-electrons and f-electrons hybridize and become itinerant below T_K. 26

3.3 Schematic diagram showcasing the emergence of a quantum critical state from a QCP. 28

4.1 a) Voltage-squared vs. resistance component for various types of conductors. b) Apparent power vs. temperature, for various wire resistances. 31

4.2 Diagram of two resistors connected by a transmission line of length ℓ. 31

4.3 Noise data showing fits on a) 50μm wire b) $5 \times 10\mu$m wires in series and c) $30\times \sim 1\mu$m wires in series. The inset shows the temperature profile for each wire configuration. 34

4.4 Representative data on InSb samples showcasing the $1/f$ noise dependence on frequency and bias. 36

4.5 Evolution of the Fano factor as a function of nanowire length. 43

4.6 Electron distribution in a nanowire system in the regime $L_\phi < L < L_{e-e}$(solid black line) and $L_{e-e} < L < L_{e-ph}$(dashed blue line). Distribution from contact pad 1 to nanowire to contact pad 2. . 45

5.1 PMMA 495 film thickness v spin speed plot for different resist solutions. 47

5.2 PL and EBL exposure and development process. 48

5.3 Examples of a) over and under exposure (top view) and b) over and under development (side view). 49

5.4 Example of EBL point grid and exposure. 50

5.5 a) Single layer b) double layer resist after development and deposition. 52

5.6 Example of E-beam evaporation mechanism. 54

5.7 Example of Plasma sputtering mechanism. 55

5.8 RIE process flow. 56

5.9 DC resistance measurement setup with a voltage source and the sample as the blue block. The source,voltage amplifier, and current amplifier used are Stanford Research DS345,SR560,SR570 respectively. 59

5.10 AC resistance measurement setup with an AC voltage source with the sample as the blue block. Lock-ins used are Signal Recovery Model 7270 and 7265 60

5.11 Example of valid connection setups for a VdP measurement with a) arbitrary polygonal and b) rectangular sample. 61

5.12 Circuit diagram of the low-frequency noise measurement setup. The dashed line indicates the components within a Faraday cage. Sample is indicated by the blue device. Amplifier chains consist of an LI-75A followed by an SR560 in differential and single modes. The oscilloscope used is the Picoscope 4262. 64

5.13 Noise probe **1)** Vacuum cap with LEMO connection. **2)** Stainless steel rod with low-temperature wires inside connected to the vacuum cap via spring. **3)** Sample holder insertion. **4)** Thermal connection to the PPMS bottom (electrically isolated). **5)** Sample holder. 67

5.14 Example of calibration data using a test 1 kΩ resistor with noise taken at temperature values of 3, 5, 7, 10, 20, 30, 50, 100, and 200 K. 68

6.1 Film stacking information. a) Stacking diagram of the $\mathrm{YbAl_3}$ films. Resistivity data of b) a mixed $\mathrm{YbAl_3}$ (YA 20 nm/LA 1.6 nm/Al 1.2 nm) stack showing difference from c) a pure $\mathrm{LuAl_3}$ resistivity showcasing how the $\mathrm{YbAl_3}$ features dominate the electronic properties at low-T. 73

6.2 Image of a representative $\sim 30\mu$m $\mathrm{YbAl_3}$ via scanning electron microscopy (SEM) 74

6.3 a) Resistivity of unpatterned film and a representative wire of $\mathrm{YbAl_3}$. b) Magnetoresistance data with field going into the plane of the film in all except at 10 K. Curves shifted for clarity 75

6.4 a, b) MG data with the linear-in-B background subtracted for 154 nm and 168 nm wide devices respectively at various temperatures below 3 K. WAL is observed at low fields and UCF is observed at higher fields at representative temperatures, $T = 0.2, 1, 2$ K. c, d) MR data with fits from Eq. 6.2 superimposed. e) Coherence length as a function of temperature from fits from Eq. 6.2. 76

6.5 a) Noise vs. bias current in a 265 nm wide wire with fits to Eq. 6.5. b) Calculated Γ vs substrate temperature T for same wire. Error is comparable to marker size. 80

6.6 a) Density of states (DOS) corresponding to Yb $4f$ states at different temperatures. The inset zooms in the DOS at the range of [-8, -4] eV. b) DOS of Yb $4f$ states close to the Fermi level E_F ([-0.5, 0.5] eV). c) Hybridization function of Yb $4f$ states at the energy range of [-0.5, 0.5] eV. 82

6.7 a) Phonon band structure and phonon DOS of $YbAl_3$ with resolved contributions from Al and Yb. The frequencies corresponding to the distortion modes G and R are marked on the phonon band structure, with the atomic displacements illustrated on the right panel. The imaginary b) and real parts c) of self-energy difference ($\Sigma^{ph} - \Sigma^{cn}$) corresponding to $J = 7/2$ between the perturbed cell (Σ^{ph}) and the unperturbed cell (Σ^{cn}) at $T = 20$ and 200 K for modes G and R. . . . 83

7.1 Phase diagram showcasing emergence of strange metallicity from a QCP @ $B \approx 0.7$ T when $B \parallel c$-axis. The line in the line diagram indicates the transition temperature $T^*(B)$ at $B \perp c$-axis 86

7.2 $YbRh_2Si_2$ nanowire and pads defined for shot noise measurements with an additional image to view the wire quality at increased magnification. 88

7.3 Noise vs. bias current for a a) $YbRh_2Si_2$ and b) Au wire at 4 temperatures $T = 10, 7, 5, 3$ K. YRS data is shown to be suppressed below the expected F while Au conforms well to a $F = 1/3$ 89

7.4 Fano factors of YRS wire and Au wire as a function of temperature. Side panels offer a visual representation of quasiparticle interaction in relation to specific values of the $F = 0$, $1/3$, $\sqrt{3}/4$. 90

7.5 a) MR measurements up to 4 K for $B \parallel c$ and $B \perp c$. b) $R(T)$ down to 3 K. 91

7.6 a) $R(T)$ data showing flattening at $T \approx 300$ mK due to thermalization. Guiding lines help indicate linearity from strange metal (black) and flat region from thermalization (pink). b) MR data at the effective 300 mK and 1 K. 92

8.1 Phase diagram of the exponent α in the equation $\rho = \rho_0 + AT^\alpha$ showcasing emergence of strange metallicity from a QCP @ $B \approx 7.8$ T when $B \parallel c$-axis 94

8.2 a) X-ray diffraction data of SR)327 samples showcasing peaks corresponding to SRO327, red dashed lines, SRO214, blue dashed lines, and the substrate LSAT, black dashed lines. Data is of several samples offset from one another for clarity and colored such that red curves are the highest quality, blue is mixed with SRO214, and black curves which are of low quality mixed with SRO4310. b) Temperature dependent resistivity data at 4 different magnetic fields parallel to the c-axis, $B = 0, 3, 6, 9$ T, showcasing the evolution from Fermi liquid T^2-behavior to the strange metal T-behavior in the representative high quality film JK22012 95

8.3 Image of the SRO327 surface after exposure to a 100kV e-beam from the Elionix system. 96

8.4 Plots of scattering calculations at several column voltages for EBL. Of note is the decreased scattering as voltage is increased resulting in a increase in resolution. 97

8.5 a) Normalized R vs. T for the unpatterned film, film after 10kV exposure(and deposition of pads), and the nanowire fabricated via etching at 8 T, $B \parallel c$-axis . b) Raw noise data of the final fabricated nanowire showing a large $1/f$ presence across the whole noise spectra. 97
8.6 a) Pattern design for a FIB outline of a SRO327 nanowire with a zoom in of the actual wire. Black lines indicate where material is removed via FIB. b) Atomic force microscopy (AFM) image of failed test example of FIB process on SiO_2. 99
8.7 a) Raw noise data of a 2 μm wide photolithographically defined wire. b) Image of the 3D design of the 100 nm x 10 μm nanowire with triangular anchors for stability all 1 μm. 101

A.1 Resistivity vs. temperature of $CeCoIn_5$ showcasing the strange metal behavior below $T \approx 40$ K. 116
A.2 Voltage vs. temperature showcasing shifting of the superconducting transition of FeSe. 117

Introduction

In standard conductors, the mechanisms for electron transport are governed by weak electron-electron (e-e) interactions compared to the electrons' interactions with the lattice. In these materials, band theory provides good estimates of electronic properties. However, when e-e interactions become stronger, these models begin to break down and electron kinetics become more complicated. Materials that display strong e-e interactions are referred to as strongly correlated materials.

Strongly correlated materials come in many different varieties, and fully studying every variation would require decades of meticulous research. To that end, this thesis focuses on two particular classifications: heavy fermion Fermi liquids and strange metals. These two types of strong correlations are discussed in this thesis in the context of two sets of measurements: magnetoresistance and noise spectroscopy. These measurements are performed on fabricated devices using thin films of strongly correlated materials, allowing for mesoscopic analysis of their electronic properties.

Heavy fermion Fermi liquids are materials in which coherent quasiparticles are inferred, but usually not directly tested, to explain the conductive properties of the Fermi liquid. Mesoscopic conductance effects such as weak antilocalization and universal conductance fluctuations can be measured via magnetoresistance measurements of fabricated nanowires to probe the coherence of the quasiparticles. Noise measurements have also led to inferring an anomalous temperature dependence of the electron-phonon (e-ph) coupling in heavy fermion systems.

Unlike the for heavy fermion Fermi liquids, strange metals seemingly cannot be properly explained under the framework of independent quasiparticles. Previous shot noise measurements have been conducted to test for the existence of quasiparticles in these materials. New measurements are being performed to continue testing the existence, or lack thereof, of quasiparticles via mesoscopic magnetoresistance and further noise measurements at lower temperatures, where the state of the materials can be tuned between a Fermi liquid and a strange metal for direct comparison.

1.1 Thesis Outline

The following four chapters of this thesis provide background information on the materials and methods used. Chapter 2 provides a background in conduction in conductors and introduces the concepts relevant to conduction in mesoscale devices. Chapter 3 provides a brief explanation and examples of both heavy fermion and strange metal materials via experiments and theoretical models. Chapter 4 serves as theoretical background on the different types of noise encountered in measurements and their origins. Finally, Chapter 5 provides a detailed explanation of experimental methodology. It opens with a general explanation of fabrication techniques as well as how to consider all the parameters when attempting to fabricate and how they can affect the final outcome, with the hope that this could be used as a general reference for future students new to device fabrication. Next, it explains in detail the various resistance-type measurements that are performed in this thesis and the cryogenic measurement setup in which 90% of measurements are conducted. Finally, this chapter discusses the noise measurement setup and rough data collection procedure, with more information found in Appendix B.

The next three chapters of this thesis contain the bulk of the experiments performed on heavy fermion and strange metal materials. Chapter 6 discusses magnetoresistance and noise measurements in the heavy fermion Fermi liquid $\mathrm{YbAl_3}$. The magnetoresistance measurements are used to determine the coherence of the heavy fermion quasiparticles found in the Fermi liquid state at low temperatures. The noise measurements detail the anomalous temperature evolution of the e-ph coupling and connect these observations to theoretical models. Chapter 7 details previous shot noise measurements performed in the Natelson lab on the strange metal $\mathrm{YbRh_2Si_2}$ to determine the fate of quasiparticles in the strange metal phase and discusses current measurements being conducted to expand upon these results. The current measurements seek to use magnetoresistance measurements at lower temperatures than the previous measurements to measure both the Fermi liquid regime and the strange metal regime in the same sample. In addition, repetition of the previous measurements at these lower temperatures is being set up through collaborative efforts. The last of the three chapters, Chapter 8, describes an attempted study of the strange metal $Sr_3Ru_2O_7$ with the goal of achieving a more universal statement about the strange metal state. This chapter describes the failed fabrication attempts to create nanowires of the strange metal and offers further fabrication ideas that exceeded the current capabilities of both thin film growth of $Sr_3Ru_2O_7$ and fabrication at Rice.

Chapter 9 serves to summarize all the findings of the three studies on heavy fermion Fermi liquids and strange metal materials and directs readers toward the potential future studies that are discussed in more detail in Appendix A.

Solid State Background

This thesis covers measurements of electrons at both the macroscopic scale and quantum scale. Here, the basics needed to understand conduction from the macro scale to the quantum scale will be covered. The discussion will begin with the fundamentals of macroscopic conduction in crystals, then transition into discussion of the limits of the macroscopic model, and then into quantized conductance shown via the Landauer-Büttiker model. Additionally, discussion of some relevant mesoscale quantum effects will be covered using topics introduced.

2.1 Bulk Conduction

Any discussion of electron conduction should begin with the fundamental definitions of Ohm's law[1]: the current (I) through a resistor is proportional to voltage difference across the resistor (ΔV) by the resistance (R).

$$\Delta V = IR \tag{2.1}$$

R is considered to be constant in Ohm's law and can be defined by a more fundamental quantity, resistivity (ρ):

$$R = \rho \frac{L}{A} \tag{2.2}$$

with L being the length of the wire parallel to the current path and A being the cross-sectional area perpendicular to the current path.

Redefining Eq. 2.1 in terms of ρ, or more frequently its inverse, conductivity (σ), gives a geometrically independent and more general statement:

$$\mathbf{J} = \frac{1}{\rho}\mathbf{E} = \sigma\mathbf{E} \tag{2.3}$$

with **J** being the current density and **E** being the applied electric field.

The natural next question to ask is: where does conductivity in materials originate? Paul Drude[2] offered a solution in the form of considering all the electrons in a metal as a non-interacting gas. Drude made the assumption that all the electrons move at speed v, in the absence of any applied fields, in random directions. This gives an average velocity of the electrons to be zero. Additionally, since they are non-interacting, the electrons can only interact with the lattice through which they flow, scattering off defects in the metal. These scattering events will occur elastically and have a probability of occurring within time τ of $1/\tau$. Here, τ is the average time between collisions, and with the electron's speed v, the average length traveled by the electrons between collisions can be defined as $\ell = v\tau$. These are the fundamental assumptions of the Drude model.

If an external electric field **E** is applied to the material, the electrons will experience a force defined as:

$$\mathbf{F} = -e(\mathbf{E}) \tag{2.4}$$

with e being the charge of the electron. This results in the electrons experiencing am average drift velocity:

$$\mathbf{v}_d = -\frac{e\mathbf{E}}{m_e}\tau \tag{2.5}$$

with the velocity imparted by **E** defined as the drift velocity $\mathbf{v}_d$ and m_e being the mass of a single electron. Current density can then be defined using the electron density n:

$$\mathbf{J} = -ne\mathbf{v}_d = \frac{ne^2\tau}{m_e}\mathbf{E} \tag{2.6}$$

Using the redefinition of Ohm's law from Eq. 2.3, it can be seen that the conductivity is defined in the context of electrons as:

$$\sigma = \frac{ne^2\tau}{m_e} \tag{2.7}$$

Thus giving a fundamental definition of the macroscopic quantity of conductivity.

This definition is derived from classical considerations, which normally break down as limits approach the quantum scale of electrons. This classical definition works very well in many cases but fails to explain many other properties of electrons by only considering them as particles.

2.1.1 Bloch States

In reality, electrons can't be considered as just particles; they need to be treated as waves as well. Felix Bloch describes this very well in crystals with his Bloch theorem. As opposed to the classical picture that the atoms making up the lattice are just holding the electrons in place, Bloch offers the additional caveat that each atom provides a potential and that this potential is periodic with the lattice and affects the electrons as such.

This periodicity is such that the atoms are defined by lattice vector **R** such that the potential behaves as $V(\mathbf{r}+\mathbf{R}) = V(\mathbf{r})$. This can also be represented via a translation operator:

$$T_{\mathbf{R}}f(\mathbf{r}) = f(\mathbf{r}+\mathbf{R}) \tag{2.8}$$

With this, a wavefunction ($\psi(\mathbf{r})$) can be defined that describes the electron based on the Schrödinger equation:

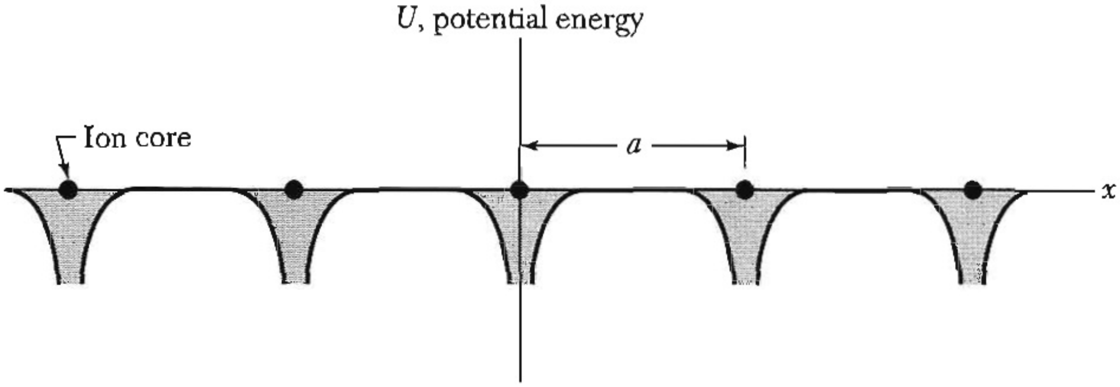

Figure 2.1 : 1D periodic potential centered on the atoms(ion cores) and spaced by the lattice spacing a

[3, Reproduced]

$$H\psi(\mathbf{r}) = \left(\frac{\hbar^2 k^2}{2m_e} + V(\mathbf{r})\right)\psi(\mathbf{r}) = E\psi(\mathbf{r}) \tag{2.9}$$

With $\mathbf{k} = x_1\mathbf{b}_1 + x_2\mathbf{b}_2 + x_3\mathbf{b}_3$ representing the wavevector, a quantity analogous to momentum in classical mechanics that contains information on the lattice in reciprocal space ($\mathbf{b}_i$), or momentum-space. Since $V(\mathbf{r})$ is periodic, this means that $T_{\mathbf{R}}$ commutes with H and can be applied to $\psi(\mathbf{r})$ such that:

$$T_{\mathbf{R}}\psi(\mathbf{r}) = \psi(\mathbf{r}+\mathbf{R}) = c(\mathbf{R})\psi(\mathbf{r}) \tag{2.10}$$

Translations performed in repetition should be able to be done in any order since the translation operator commutes with itself. This means that the eigenvalues can be represented as:

$$c(\mathbf{R}+\mathbf{R}') = c(\mathbf{R})c(\mathbf{R}') = c(\mathbf{R}')c(\mathbf{R}) \tag{2.11}$$

Additionally, the translation operator also needs to maintain renormalizability in the wavefunction. These two statements imply that the operator should be unitary and additive for successive periodic translations. Indeed that is the case, and $c(\mathbf{R})$ is described in a way that contains information about the lattice via $\mathbf{k}$:

$$c(\mathbf{R}) = e^{\mathbf{ik}\cdot\mathbf{R}} \tag{2.12}$$

Now applying the translation operator onto the wavefunction gives:

$$T_{\mathbf{R}}\psi(\mathbf{r}) = e^{\mathbf{ik}\cdot\mathbf{R}}\psi(\mathbf{r}) \tag{2.13}$$

which is the crux of Bloch's theorem.

If it's now assumed that there is a periodic function, $u_k(\mathbf{r}) \equiv e^{-i\mathbf{k}\cdot\mathbf{r}}\psi(\mathbf{r})$, that satisfies Bloch's theorem, then a single-particle wavefunction can be immediately defined as a plane wave multiplied by a function with the periodicity of the lattice.

$$\psi(\mathbf{r}) = e^{\mathbf{ik}\cdot\mathbf{r}}u_k(\mathbf{r}) \tag{2.14}$$

This wave function serves to describe the single particle states of electrons, called Bloch electrons in a weak periodic potential as modulated plane waves. In the case of stronger potentials felt by electrons near the ion cores the electrons can be broken up into two groups: those localized to the ion core and those that participate in the chemical bindings the neighboring atoms. The electrons that are considered localized don't move around in free space like the conduction electrons, which are considered to be extended states that propagate throughout the material. Disruptions in the lattice periodicity can act to scatter the Bloch electrons, or conduction electrons, and in certain situations this can trap the electron in a localized state. These disruptions in periodicity can come in the form of impurities or defects within the lattice itself.

To begin thinking about the allowed energy (E) levels and $\mathbf{k}$ values, some boundaries will need to be defined to solve Eq. 2.9. The Born-von Karman boundary conditions assume that ψ has the same periodicity as the lattice. Assuming that the atoms are spaced by $\mathbf{a}_i$ and there can be N_i number of atoms away from each other in the ith direction, then:

$$\psi(\mathbf{r} + N_i\mathbf{a}_i) = \psi(\mathbf{r}) \tag{2.15}$$

Given the knowledge of the orthogonality of the lattice spacing $\mathbf{a}_i$ and the reciprocal lattice spacing $\mathbf{b}_i$ ($\mathbf{a} \cdot \mathbf{b} = 2\pi$), Bloch's theorem states that:

$$e^{\mathrm{i}N_i\mathbf{k}\cdot\mathbf{a}_i} = e^{2\pi\mathrm{i}N_i x_i} = 1 \tag{2.16}$$

This equation defines the x_i values of $\mathbf{k}$. Eq. 2.16 can only hold true if $N_i x_i$ is a whole number, meaning that:

$$x_i = \frac{j_i}{N_i}, \quad j_i = 1, 2, 3, ..., N_i \tag{2.17}$$

This means that $\mathbf{k}$ can only have certain allowed values, equal to the number of lattice sites in one direction.

$$\mathbf{k} = \sum_{i=1}^{3} \frac{j_i}{N_i}\mathbf{b}_i \tag{2.18}$$

To understand this revelation, consider a region in k-space that contains a set of points that form the smallest volume around the origin called the first Brillouin zone. This zone describes the entire lattice in k-space and can be understood as a repeating volume throughout the crystal. Now for each unique $\mathbf{k}$, of which there are N in a Brillouin zone, there are several different energy solutions. These energies are differentiated by a band index n. As $\mathbf{k}$ extends past the first Brillouin zone, due to periodicity, they map back to $\mathbf{k}$ values in the first Brillouin zone but increase to the next band index. This results in energy bands E_n separated by forbidden regions that can't contain solutions pictured in Fig. 2.2.

This band structure, in the absence of e-e interaction, always fills from lower

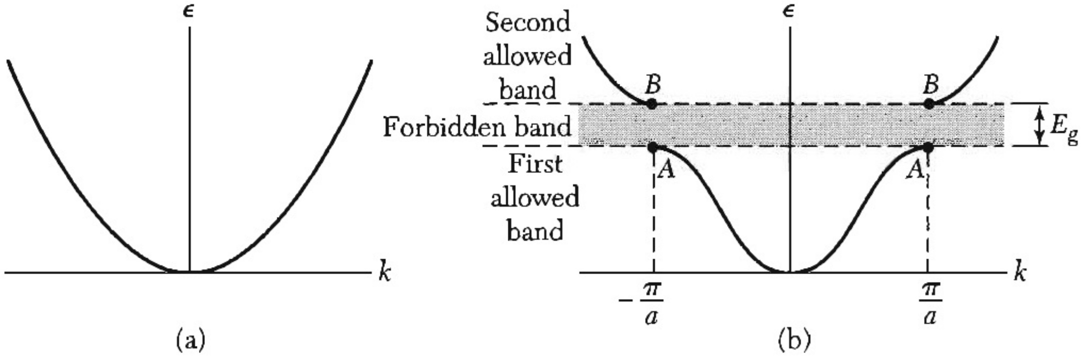

Figure 2.2 : a) Energy dispersion of a free electron. b) Energy dispersion in a crystal lattice showcasing a band gap E_g of forbidden energy values.
[3, Reproduced]

to higher energy and when coupled with counting of electrons is the determinant of whether a materials is insulating or conducting. With the idea of energy bands resulting from electrons in a lattice, it is important now to consider what is happening to the lattice itself and the energy levels it introduces by bringing vibrations into the picture.

2.1.2 Phonon States

The Bloch picture assumes that the lattice is stationary and only considers the movement of the electrons throughout the lattice, thus producing these electron energy bands. In reality, the lattice can move and the vibrational waves have their own band structure of $\hbar\omega(\mathbf{k})$. This movement, through vibration modes, can be quantized and referred to as phonons in crystal lattices. But how do these phonon modes appear?

The classical picture is the best place to begin. Assume there is a 1D chain of N atoms, each with mass M, connected to each other by springs, of spring constant K, and spaced a apart from one another. To preserve the periodicity of the lattice, assume that the farthest left atom is connected to the farthest right atom by a massless rod of length Na as seen in Fig. 2.3. The potential of this picture can be described by:

$$V = \frac{1}{2}K\sum_n [u(na) - u((n+1)a)]^2 \tag{2.19}$$

Here, n denotes an atom from a predetermined origin and $u(na)$ describes displacement from an atom's equilibrium position.

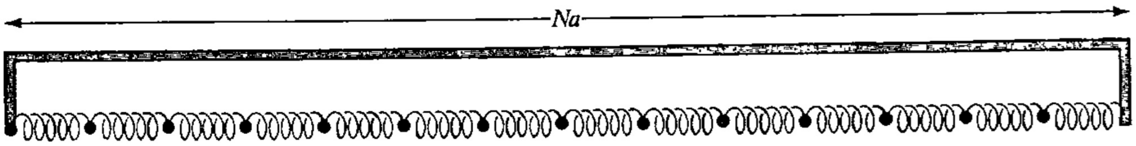

Figure 2.3 : 1D chain of atoms connected by springs with a $L = Na$ massless rod connecting the leftmost atom to the rightmost atom fulfilling the Born-von Karman boundary conditions.
[4, Reproduced]

The equations of motion are then defined as:

$$M\ddot{u} = -\frac{\partial V}{\partial u(na)} = -K\sum_n [2u(na) - u((n-1)a) - u((n+1)a)] \tag{2.20}$$

This describes the motion of each atom. Adding in the periodicity, such that $u(Na) = u(0)$, determines the form of u:

$$u(na, t) \propto e^{\mathrm{i}(kx - \omega t)} \tag{2.21}$$

ω is the frequency at which the atom oscillates. Using the same argument from Eq. 2.16 shows that k is of the form:

$$k = \frac{2\pi}{a}\frac{n}{N} \tag{2.22}$$

Upon substituting Eq. 2.21 into Eq. 2.20:

$$-M\omega^2 e^{\mathrm{i}(kx-\omega t)} = -Ke^{\mathrm{i}(kx-\omega t)}[2 - e^{-\mathrm{i}ka} - e^{\mathrm{i}ka}] \tag{2.23}$$

$$= -4Ke^{\mathrm{i}(kx-\omega t)} \sin^2\left(\frac{1}{2}ka\right) \tag{2.24}$$

A solution for ω in terms of k can be found:

$$\omega(k) = 2\sqrt{\frac{K}{M}}\left|\sin\left(\frac{1}{2}ka\right)\right| \tag{2.25}$$

If one instead assumes a lattice with a basis of two atoms as seen in Fig. 2.4, $\omega(k)$ takes on multiple values now and adds a new phonon mode to the dispersion relation.

$$\omega^2 = \frac{K+G}{M} \pm \frac{1}{M}\sqrt{K^2 + G^2 + 2KG\cos ka} \tag{2.26}$$

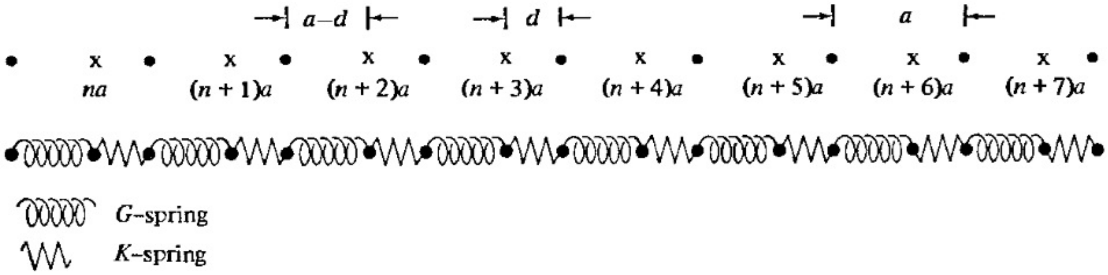

Figure 2.4 : 1D diatomic chain of atoms with spring constant within the basis being K and the spring constant between bases being G.
[4, Reproduced]

The two possible solutions for ω create two phonon modes or branches. The higher energy of the two is the optical branch. The motion of the optical mode can be considered as the atoms of the basis in each unit cell moving out of phase with from its neighboring cells by ka. The acoustic phonon from the monatomic example can be observed as well. The acoustic phonon motion can be thought of as all the atoms oscillating in sync together along the chain.

Taking this example case and applying a more quantum mechanical approach

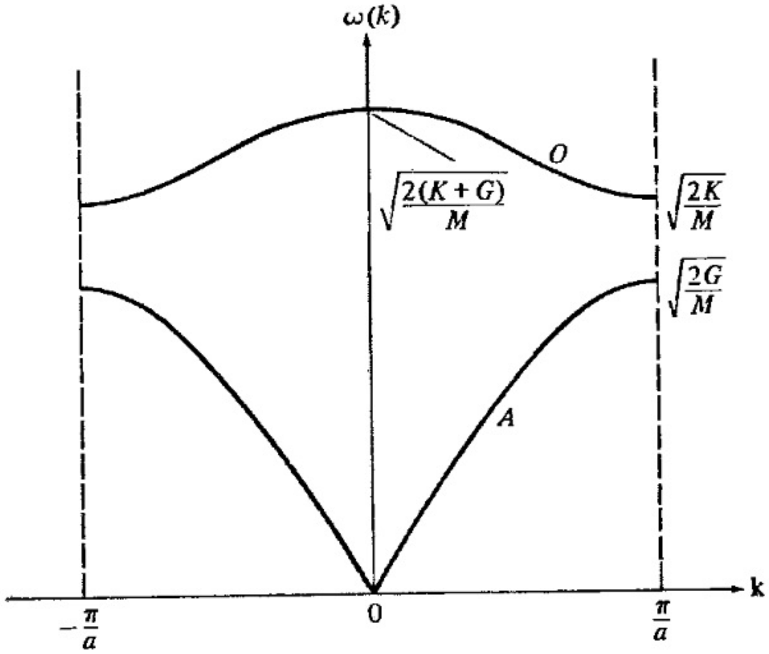

Figure 2.5 : Phonon modes of the diatomic 1D chain. The upper branch is the optical phonon and the lower branch is the acoustic phonon
[4, Reproduced]

gives a quantized energy, normally $E = \hbar\omega$.

$$E = \sum_{ks} \left(n_{ks} + \frac{1}{2} \right) \hbar\omega(k) \tag{2.27}$$

Again the energy contains forbidden regions between the different bands similarly to the electron case. These phonon modes can play an important role in conduction as well as in how crystals behave at low temperatures. Importantly, if the electron energy bands begin to become of comparable magnitude to the phonon energy bands, there can be strong energy transfer between the two. This results in increased e-ph scattering, which is the medium for energy transfer between the two!

2.2 Length Scales in Metals *

With the basics of classical conduction and the introduction of electron and phonon energy bands covered, it's useful to discuss what happens to electrons moving through a material at various length scales. To begin the discussion of the different length scales, consider a polycrystalline gold wire of length L and diameter d such that $L \gg d$. An electron moving through this gold wire will encounter scattering events throughout the crystal. As mentioned in Section 2.1, the length over which an electron doesn't encounter a scattering event is referred to as the mean free path ℓ in the periodic lattice. These scattering events occur when electrons encounter defects of some kind. One such common defect in polycrystalline gold occurs when electrons run into a grain boundary. Grains define regions of the crystallinity with a particular crystallographic orientation. The orientation differs as the grain boundary is crossed resulting in an increased scattering rate at the boundary. Gold grain sizes are $\sim 20-40$ nm and, in the case of metals, make for a decent approximation of ℓ, in the absence of phonons.

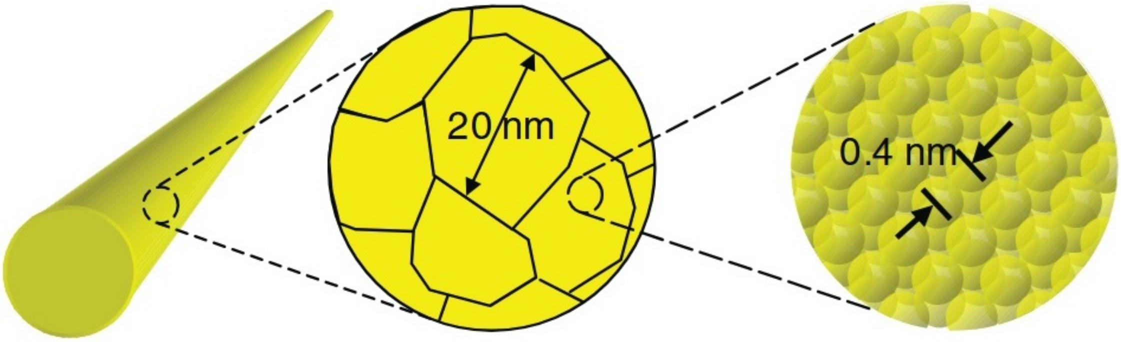

Figure 2.6 : A gold wire. A zoomed in look reveals that it is broken up into $\sim$ 20 nm size grains. Further zoom reveals the grains are composed of face-centered cubic atoms spaced $a \sim 4$ Å

[5, Reproduced]

Moving away from the classical picture to the wave-like nature of the quantum mechanical picture of the conduction electron, we can examine their quantum proper-

---

*Values in this section are taken from Nanostructures and Nanotechnology[5] ties. Since electrons are wave-like, they should have an effective wavelength. Indeed they do — the effective wavelength of the conduction electrons is called the Fermi wavelength $\lambda_F \approx 5$ Å, though this value depends on the electron density. In addition to having wavelengths, wave-like electrons also carry phases. Therefore, if electrons interact with one another when they are out of phase by π radians they can interfere destructively. The phase of the electrons gets affected by other electrons and phonons. The scale over which an electron can travel while ing its well-defined phase is the coherence length L_ϕ. In the case of gold at room temperature $L_\phi \sim 1-2$ nm.

Electrons can also physically interact with each other via Coulomb scattering processes. In metals such as gold, this is characterized by the Thomas-Fermi screening length $r_{TF} \sim 4$ Å. This length determines the proximity of electrons to one another at which they begin to feel the interaction of neighboring electrons. As mentioned in the previous section, phonons can also result in scattering events involving electrons even in defect-less crystals. The vibrations of the lattice can create dipole moments that interact with the conduction electrons on a length scale referred to as the e-ph scattering length L_{e-ph}. This interaction is very important and plays a large role in energy transfer — both electrical and heat conduction — of electrons. In metals such as gold at low temperatures ~ 3 K one can expect a scattering length of $L_{e-ph} \sim 2$ μm.

If the length of the gold wire is less than L_ϕ the electron can travel without encountering scattering events. In this regime, electron transport is said to be ballistic, as opposed to the diffusive model when $L > L_\phi$. Resistance is often considered to be the result of electron interactions with the lattice and other electrons so one would naively think that in the ballistic regime with no scattering, resistance would go to zero. While that may be true for the wire, in reality there are contacts with electrodes connected to them to measure these wires. The interface between the contacts and the electrodes has its own resistance that gets added to the total preventing its resistance from becoming zero in a 2-terminal measurement setup. Taking a more in-depth look into the quantum mechanical nature of transport in the ballistic regime is helpful to understand what exactly is going on in the gold wire and its contacts.

2.3 Landauer-Büttiker Formalism

To begin with the quantum mechanical picture of conduction, consider a narrow ballistic conductor of length $L \ll \ell$ connected at each end to classical contacts. This model was introduced by Rolf Landauer in 1957[6] and later formalized by Datta[7] and Ferry & Goodnick[8] in the late 1990s. The conductor is considered to be 1D, for ease, and contains energy subbands, as shown in the plot in Fig. 2.7, spaced far apart compared to thermal energy k_BT, with k_B being the Boltzmann constant. Additionally, like the Bloch wave discussion, the electrons are assumed to be non-interacting and is therefore the model is a single-particle model. We can define the number of occupied modes (propagating electron states) at any given energy E as $M(E)$.

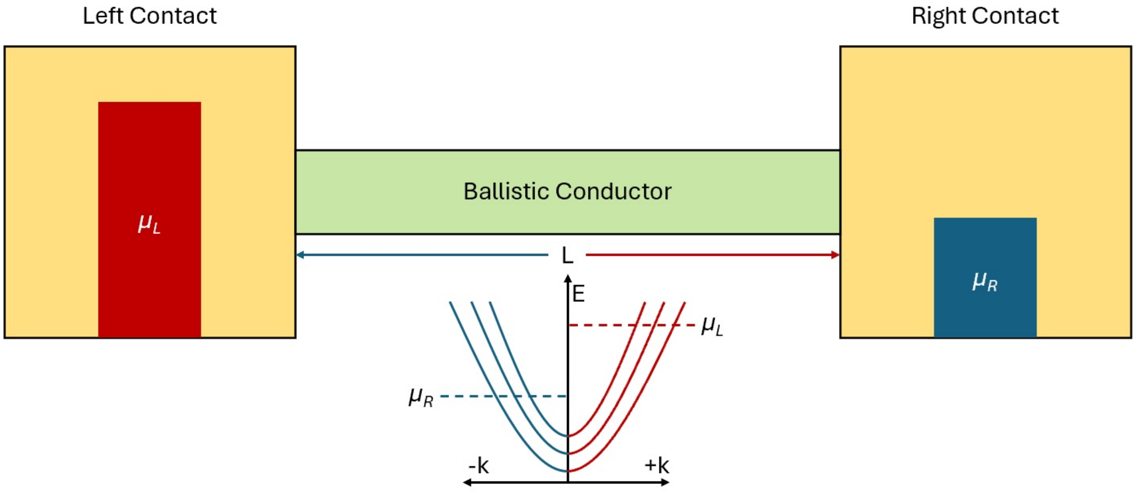

Figure 2.7 : Ballistic conductor with a left and right contact with chemical potentials μ_L and μ_R respectively. The lower plot contains an energy dispersion curve showcasing left-moving and right-moving electrons with colors indicating electrons moving from left to right (red) and right to left (blue).

The contacts in the model are considered as electron reservoirs that do not permit reflections at their interfaces. They also each have a chemical potential μ_L and μ_R for the left and right contacts,, respectively. Due to the lack of reflection at the contact interface, all right-moving ($k > 0$) electrons in the conductor originate from the left contact and are at energy μ_L. A similar statement can be made for left-moving ($k < 0$) electrons. If a bias is applied across the device, a difference in the chemical potential between the left and right contacts will be observed, which in turn results in the movement of the electrons. The net flux by right-moving and left-moving electrons can then be used to define the current. The probability of occupation can be defined by the quantum mechanical Fermi-Dirac function $f(E, T, \mu) = \frac{1}{e^{(E-\mu)/k_B T)}+1}$. The right-moving current is then defined as:

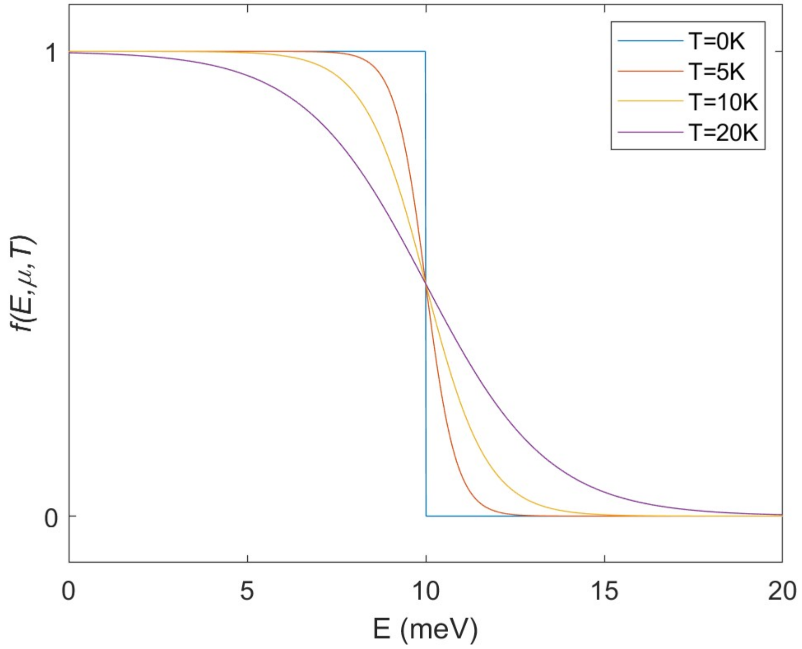

Figure 2.8 : Fermi-Dirac occupation probability at four different temperatures 0,5,10,20 K with chemical potential $\mu = 10$ meV. As $T \rightarrow 0$, the Fermi function approaches a step function.

$$I_+ = -\frac{e}{L} \sum_k v(E(k)) f_+(E, T, \mu_L) M(E(k) \tag{2.28}$$

With $v \equiv \frac{1}{h}\frac{\partial E}{\partial k}$ being the semi-classical velocity of the electrons. In 1D k-space, the solutions ψ are spaced by $\frac{2\pi}{L}$, therefore each k contains $\frac{L}{2\pi}$ states that can be occupied. This gives the density of states $\nu = \frac{L}{2\pi}\frac{dk}{dE}$. Abusing some definitions of calculus allows the statement that $\frac{\partial E}{\partial k}dk \rightarrow dE$ is true, which means that we can convert the sum over k and partial differential in Eq. 2.28 into an integral over energy by using the ν with an added factor of 2 to cover the electron spin-1/2 degeneracy.

$$I_+ = -\frac{2e}{h}\int_0^\infty f_+(E, T, \mu_L)M(E)dE \tag{2.29}$$

It makes logical sense to define the left-moving electrons similarly:

$$I_- = -\frac{2e}{h}\int_0^\infty f_-(E, T, \mu_R)M(E)dE \tag{2.30}$$

Assuming a positive bias is placed on the right contact to create the difference in chemical potential seen in Fig. 2.7 implies that the net current is $I = I_+ - I_-$. If $T = 0$, f simplifies to a step function at μ (Fig. 2.8). The integral then simply resolves to values at μ_L and μ_R for I_+ and I_-, respectively, giving I:

$$I = -\frac{2e}{h}M(\mu_L - \mu_R) \tag{2.31}$$

Because V can be defined in terms of the μs and e, the solution can be expressed in terms of V, $V = -(\mu_L - \mu_R)/e$:

$$I = \frac{2e^2}{h}MV \tag{2.32}$$

This net positive current exists because μ_L is higher than μ_R, which results in preferentially more occupied modes going from left to right. Given that Ohm's law defines the relationship between I and V involving conductance G, the conductance of the ballistic conductor is:

$$G = \frac{2e^2}{h} M \tag{2.33}$$

This is known as the Landauer formula. The Landauer formula offers several interesting insights. First, the finite value of G implies a non-zero resistance R. Considering that the conductor is a ballistic conductor and should therefore have $R = 0$, the finite conductance results from the conductor–pad interface. The contact pads have a large number of electronic modes such that $M_R, M_L \gg M$. This results in very few modes being able to couple and transmit through the conductor, causing most to be reflected, which causes interference, resulting in a non-zero resistance! Second, the implication that G is dependent on the number of modes M of the conductor means that there are quantized steps that the conductance takes defined as:

$$G_0 = \frac{2e^2}{h} \tag{2.34}$$

This dependence on modes makes it simple to generalize away from the ballistic conductor example. Instead of simply guaranteeing the passage of electrons when modes are available, the electrons have a probability of being transmitted through the conductor. The electrons that pass through do so with a probability $\mathcal{T}$, which is defined as the transmittance. This gives a fairly accurate representation of 2-terminal nanoscale conductance:

$$G = \frac{2e^2}{h} M\mathcal{T} \tag{2.35}$$

Moving forward with this interpretation, if we invert G to R and know that the sum of resistances in series should result in each resistance source, the resistance of the system can be shown as follows:

$$R = \frac{h}{2e^2M}\frac{1}{\mathcal{T}} = \frac{h}{2e^2M} + \frac{h}{2e^2M}\frac{1-\mathcal{T}}{\mathcal{T}} \tag{2.36}$$

The first term indicates the contact resistances from the ballistic case, and the second term introduces the conductor resistance via scattering.

This idea of the contact resistance begs the question: is there a way to bypass it and obtain the "true" resistance of the conductor? The answer is yes, by introducing two additional probes between the current probes that apply no current but measure voltage. This allows a direct measurement of the conductor resistance between the voltage probes, resulting in what is commonly known as a 4-terminal measurement!

2.4 Universal Conductance Fluctuations

Continuing with the idea of scattering events and transmission relating to overall conduction in materials, at mesoscopic scales these scattering events are often locked and unique to each device. As an electron moves through the conductor, it has many possible paths with different scattering events along each path. These paths result in changes in the phase of the electrons and cause the electron to interfere with itself due to this phase difference. If a known parameter is tuned and causes changes in this interference, it results in fluctuations in the conductance $\langle \delta G \rangle_{rms}$ of the mesoscopic device. As the temperature of the device approaches zero, these fluctuations approach a familiar value: $\langle \delta G \rangle_{rms} \sim \frac{2e^2}{h} = G_0$, the quantum of conductance seen in the previous section! These fluctuations are reproducible within the same device and are known as universal conductance fluctuations (UCF).

This is commonly seen when measuring mesoscopic conductance while sweeping the magnetic field. As the field is swept, it tacks on a phase to the electrons via the Aharonov-Bohm effect, causing the shift in phase to change the fluctuations. Since UCF originates from scattering events from fixed disorder, in the simplest case, as the field is swept back and forth, the fluctuations will overlap as seen in Fig. 2.9.

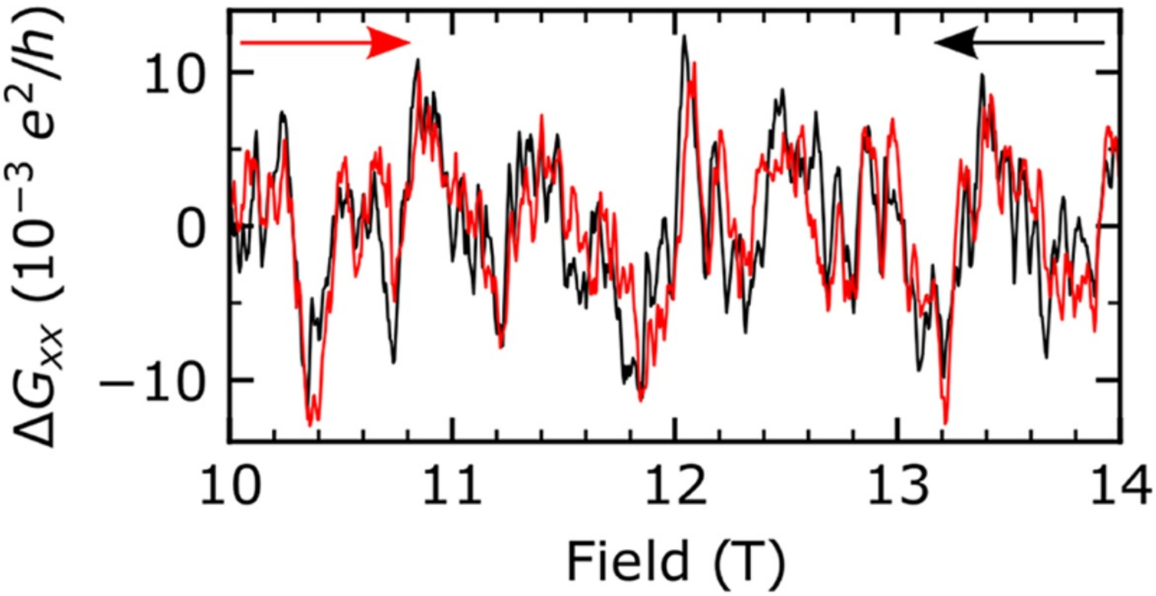

Figure 2.9 : Universal conduction data from a $\mathrm{MnBi_2Te_4}$ thin film device showcasing overlapping UCF signals. Field swept to the right(left) is indicated by red(black) data. Differences result from altering disorder as field is swept
[9, Reproduced]

Measurements of UCF in B-field contain a characteristic field scale that is determined by calculating the auto-correlation function of the conductance as a function of field.

$$F(\Delta B) = \langle g(B)g(B+\Delta B)\rangle - \langle g\rangle, \qquad g \equiv \frac{G}{G_0} \tag{2.37}$$

This field scale is related to L_ϕ, discussed in Section 2.2. The exact relationship between the field scale depends heavily on dimensionality and the strength of the spin-orbit interaction. More specific calculations will be shown in the discussion of $\mathrm{YbAl_3}$ in Chapter 6.

2.5 Weak Localization

In addition to UCF appearing in mesoscopic magnetoconductance (MG) measurements, another effect called weak localization (WL) can be observed in materials as well. Much like UCF, WL results from changes in phase due to scattering events associated with disorder in the lattice. However, in the case of WL, the scattering events result in back-scattering in a closed loop around a region of disorder. In the same vein as UCF and because of the nature of quantum mechanics, the phase picked up from a spinless electron scattering is the same if the electron travels either clockwise or counterclockwise around the loop. This causes the back-scattered phases to interfere constructively but in the opposite direction of the electron's intended direction, resulting in a reduction of conductance.

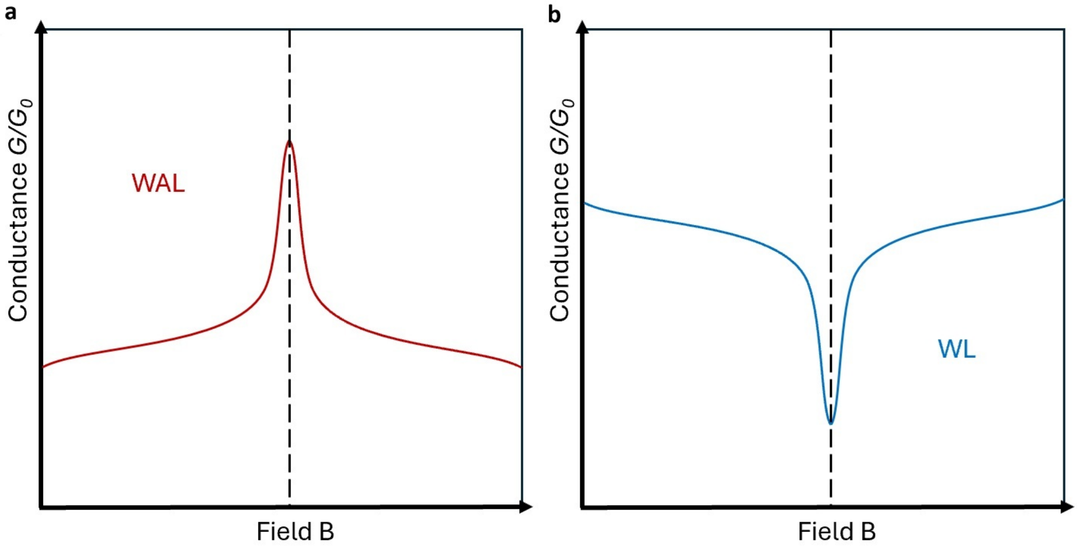

Figure 2.10 : Diagram showcasing the shape of near zero field a) weak anti-localization magnetoconductance and b) weak localization magnetoconductance.

As B-field is applied to the system, flux is threaded through the loop resulting from the localization, and phase is again added but results in a differing phase between the two paths. This results in a decay in the WL effect as B is increased, further separating the phases of the CW and CCW paths until they no longer consistently contribute to the overall conductance. This causes the conductance to increase as B is increased fairly sharply, once again with a characteristic field scale. Also once again, this characteristic field scale is related nontrivially to L_ϕ, with exact functional form varying once again with dimensionality and spin-orbit coupling strength. Both

UCF and WL result from describing trajectories of electrons that remain coherent for long enough to scatter through the system due to the mesoscopic scale of devices used to measure these effects.

This idea of spin-orbit coupling shows up in both cases but has a more prominent effect on WL than UCF. Spin-orbit coupling refers to the interaction between the band electron and the orbitals of the lattice defect at which the scattering event is taking place. This interaction again results in shifts in the phase of the traveling electron, and the electron's spin will rotate as well due to the scattering event. This rotation swaps sign if the trajectory of the electron is reversed. This results in an sign-flip from the WL picture with clockwise and counterclockwise trajectories around the loops interfering destructively at zero field. This inverse behavior of WL is referred to as weak anti-localization (WAL) and appears in materials with strong spin-orbit coupling, or materials with particularly heavy atoms such as gold.

Strongly Correlated Materials

Fermi Liquid (FL) theory is valid when the e-e interaction energies are relatively weak, compared to the single-particle bandwidth, so that quasiparticles can be used as in the simple Fermi gas model. However, when the e-e interaction becomes very strong, the FL theory begins to breakdown, leading to the observation of more exotic, strongly correlated phases. Some of the more interesting strongly correlated materials often consist of heavy atoms with partially filled *d* and *f*-electron shells, resulting in unique and exotic phases. Of particular relevance to this thesis are materials displaying heavy fermion phases and strange metallicity.

3.1 Heavy Fermions

Heavy fermion systems were first discovered in $\mathrm{CeAl_3}$[10] in 1975. These systems can be generalized via FL theory to a large increase in effective mass (m_e^*). It is best to begin with the simple Fermi gas model where e-e interactions can be ignored.

$$H\psi = E\psi \tag{3.1}$$

$$-\frac{\hbar^2}{2m_e}\nabla^2\psi = E\psi \tag{3.2}$$

From the Fermi gas model, a potential can be introduced to account for the e-e interactions accounted for.

$$-\frac{\hbar^2}{2m_e}\nabla^2\psi + V(\mathbf{r}) = E\psi \tag{3.3}$$

These potentials can be complicated many-body systems that cannot be easily modeled. FL theory[11] introduces the novel concept of quasiparticles to simplify this complicated many-body system. Quasi-particles are formed via an adiabatic transformation of a non-interacting fermion into an interacting system, and the mass (m_e) and magnetic moment are renormalized (m_e^*)[12]. This can result in a non-interacting quasiparticle with a mass and magnetic moment that differs from that of an electron.

$$-\frac{\hbar^2}{2m_e^*}\nabla^2\psi = E\psi \tag{3.4}$$

These heavy fermions can have effective masses a hundredfold times the mass of an electron due to the strong interactions[13]. These electron large electron masses are resultant of the hybridization of energy bands of the conduction electrons and the f and d-electrons flattening the bands as shown in Fig. 3.1. FL theory's use of quasiparticles helps to maintain its expected T^2 low-temperature resistance behavior, offering a simple and concise way to model these complex many-body systems.

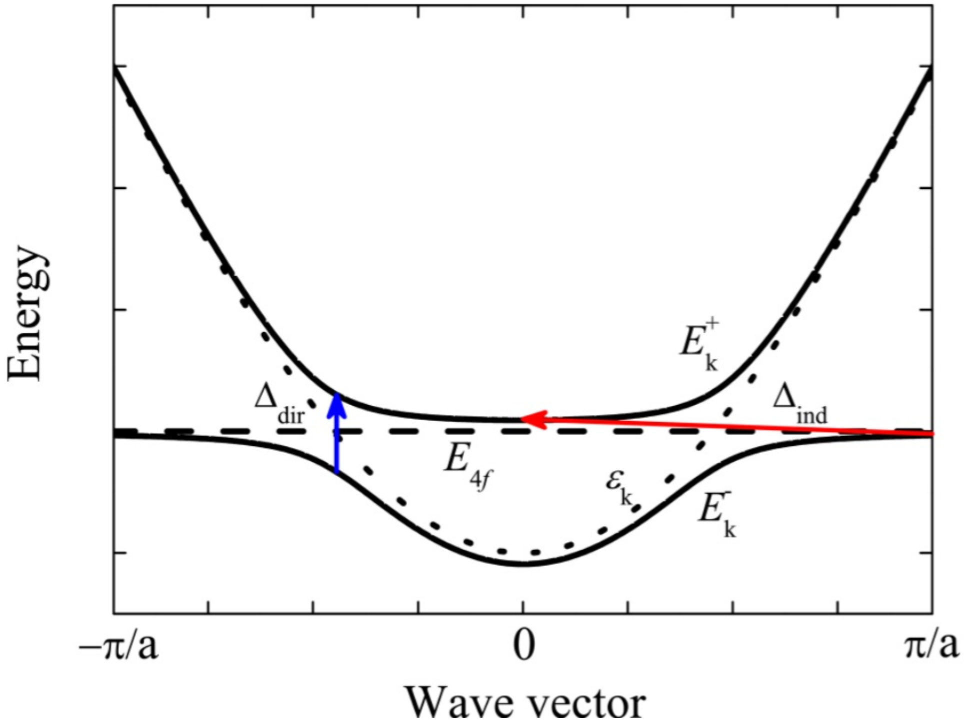

Figure 3.1 : schematic diagram showcasing the hybridization of the conduction electrons wihtt $4f$-electrons in a Kondo lattice.
[14, Reproduced]

In rare-earth element materials, the f-electrons at energies below the top of the valence band scatter conduction electrons in what is known as the Kondo effect[15]. The Kondo effect describes how below a certain characteristic temperature, the Kondo temperature T_K, the localized f-electron spin interacts strongly with the spin of the itinerant conduction electrons. Well above T_K the interaction energy scale between the spin of the f-electrons and the conduction electrons is small when compared to the thermal energ scale k_BT, resulting in a the f-electrons having little effect on the conduction electrons. Below T_K Kondo screening of the f-electron moments comes into play in their interaction with the conduction electrons resulting in hybridization between the two and the the f-electrons becoming a small part of the conduction in the heavy fermion. This strong interaction can increase the effective mass of the electrons traveling via the FL theory. The f-electrons can be thought of as becoming itinerant and joining the conduction electrons in the Fermi sea, thus providing a well-defined model of heavy fermions in heavy f-electron element materials.

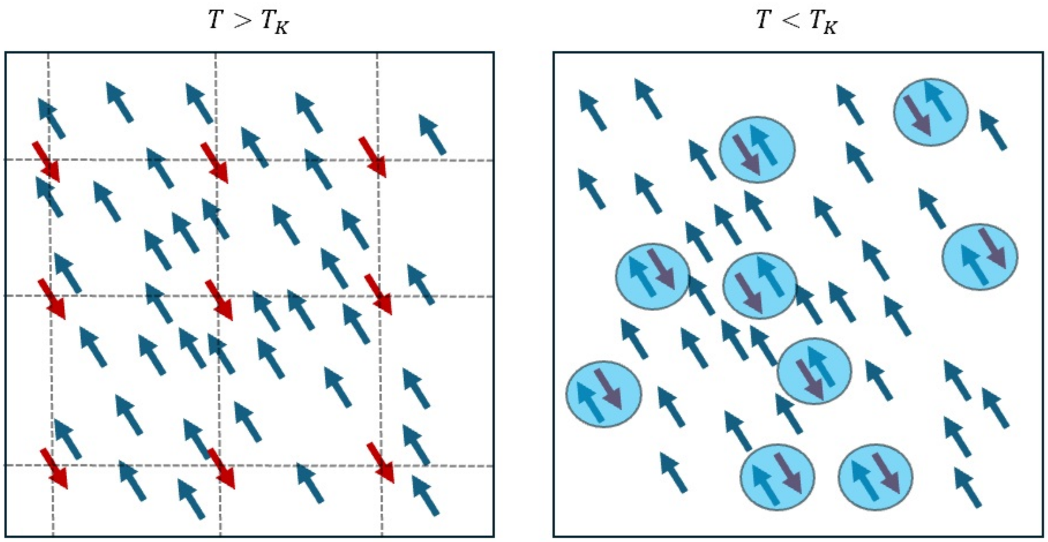

Figure 3.2 : Diagram showcasing how f-electrons (red) interact with conduction electrons (blue) in the Kondo effect with arrows indicating spin. a) Conduction electrons screen the localized f-electrons magnetic moment above T_K. b) Conduction electrons interact with f-electrons and f-electrons hybridize and become itinerant below T_K.

[16, Adapted]

In the rare-earth element heavy fermions, quantum criticality is often observed in proximity, resulting in exotic states at low temperatures. Quantum criticality refers to the low-energy excitation at a quantum critical point (QCP), which is a critical point in the phase transition occurring at absolute zero temperature[17]. Although this transition occurs at zero temperature, its presence is felt at higher temperatures, resulting in states that can disobey the FL theory. These states are cleverly referred to as *Non*-Fermi Liquid (NFL) states and are the subject of much discussion and research to understand their properties.

3.2 Strange Metal

The strange metal state is one such NFL state that is seen in proximity to a QCP. Strange metallicity can be identified by its unusual T-linear low-temperature resistance behavior and its unusual T-dependence on specific heat. What is happening in this "strange" state is still not well understood, but several theories suggest a lack of long-lived quasiparticles[18–20] common in the FL theory explanation of complex states.

Under the strange metal umbrella of linear resistivity, there are several seemingly different variants. Most commonly is the appearance of linear resistivity in superconducting cuprates[21,22].The strange metal state in these materials extends quite broadly from millikelvin temperatures[23] to temperatures as high as 1100 K[24]. In addition, it can occur in perovskite materials at various temperatures[25,26] and heavy fermion materials at low temperatures[27,28]. This broad range of effects and lack of saturation of the resistivity at higher temperatures is confusing and raises the question of whether such effects are indeed one and the same. However, the materials of interest in this thesis are those that specifically show strange metallicity at lower temperatures in proximity to a QCP.

Alongside the experimental variety of strange metals, a variety of theories have also been proposed to explain this phenomenon. For brevity, the discussion will be

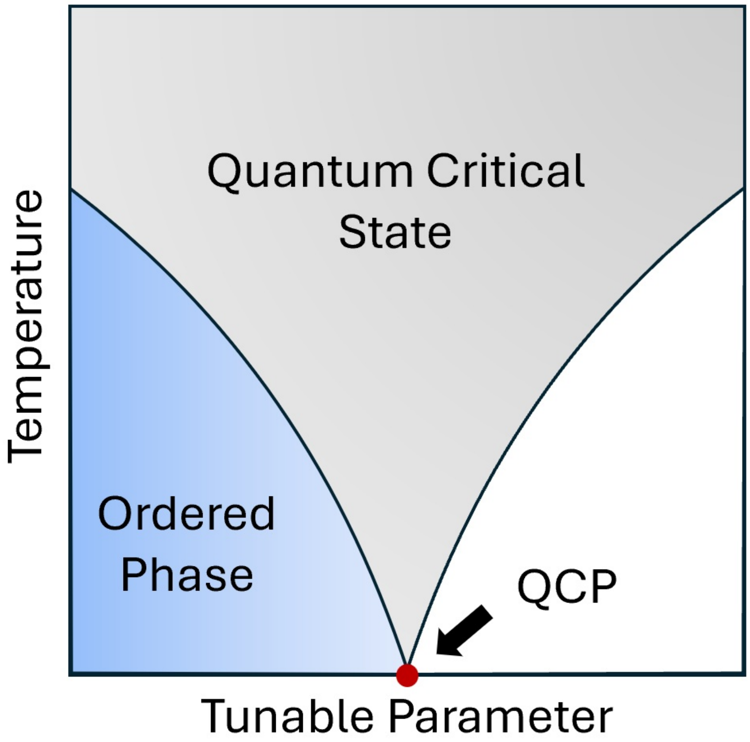

Figure 3.3 : Schematic diagram showcasing the emergence of a quantum critical state from a QCP.

limited to the case of theory of a lack of quasiparticles. As these theories are quite complicated, only brief qualitative explanations of token theoretical models will be given; anything else is beyond the scope of this thesis.

The first theory offers good modeling of strange metallicity effects via a surprising method. Holographic duality uses the parallelism between some quantum field theories and higher-dimensional curved classical gravitational theories[19] referring to these parallels as duals. The quantum state with which duality is claimed is one in which electrons moving through the material can no longer be thought of as discrete quasiparticles scattering around, resulting in resistances and heat exchange with the lattice. Instead, they should be considered as a hydrodynamical situation where scattering is events that are not related to the viscosity of the electronic fluid. The theory then converts between the duals to simplify mathematical calculation to explain the characteristic properties of a strange metal.

The second theory is the marginal Fermi liquid[29]. Here it is stated that these "strange" properties are a result of the material existing on a boundary between the FL and NFL regimes. The key component is that excitations arise and alter the charge and spin polarizability of the electrons. These polarizabilities have particular temperature and frequency dependencies that, when carried throughout, result in the T-linear resistivity seen in cuprate superconductors in the normal state.

The final theory covered in this section is based on numerical calculations of the Hubbard Model description of a strange metal[30]. The Hubbard model describes electrons moving in a lattice via a kinetic hopping parameter and the Coulomb repulsion experienced by electrons. In the case of doped cuprate, the addition of electrons via doping experience strong interaction with normally half-filled lattice sites, resulting in incoherent transport. This modeling can explain the transition from T-linear to a T-quadratic behavior as the temperature decreases.

Experimental approaches that might be able to examine signatures of these models of strange metallicity can now be considered and will be covered in the next two chapters.

Electronic Noise

Standard electronic measurements rely on the average values of the I and V, as well as their first (dI/dV) and second (d^2I/dV^2) derivatives. This offers numerous information that provides insight into the electronic environment in which they are observed. These observations provide a macroscopic view of the desired environment or material as seen in Section 2.1. To investigate the microscopic properties of a material, the fluctuations in the values of current and voltage.

Electronic noise refers to the mean squared fluctuations of the current $\langle(\delta I)^2\rangle$ and the voltage $\langle(\delta V)^2\rangle$. These values are often measured in terms of their spectral density across a given frequency range, yielding units of A^2/Hz for current and V^2/Hz for voltage. The origins and spectral response of electronic noise vary with the type of noise. Among the many types of noise, those that are particularly relevant to this thesis are Johnson-Nyquist "thermal" noise, $1/f$ "flicker" noise, and shot noise.

4.1 Thermal Noise

Thermal noise was predicted by Einstein's study of Brownian motion[31] in 1905 and is formally known as Johnson-Nyquist (JN) noise after John B Johnson and Harry Nyquist. In 1928, Johnson experimentally measured thermal noise[32] and Nyquist theoretically modeled it[33] based off of Johnson's findings. It can be described simply as fluctuations due to thermal agitation of the electrons and is present in every system with a resistance in equilibrium. At low frequencies, the mean-squared voltage fluctuations are linearly related to the resistance and temperature, as Johnson and Nyquist discovered and described, respectively, as seen in Fig. 4.1.

To conceptually understand the origins and derive the equation for the noise in a resistor at equilibrium, I paraphrase Nyquist's derivation[33]. To begin, consider two

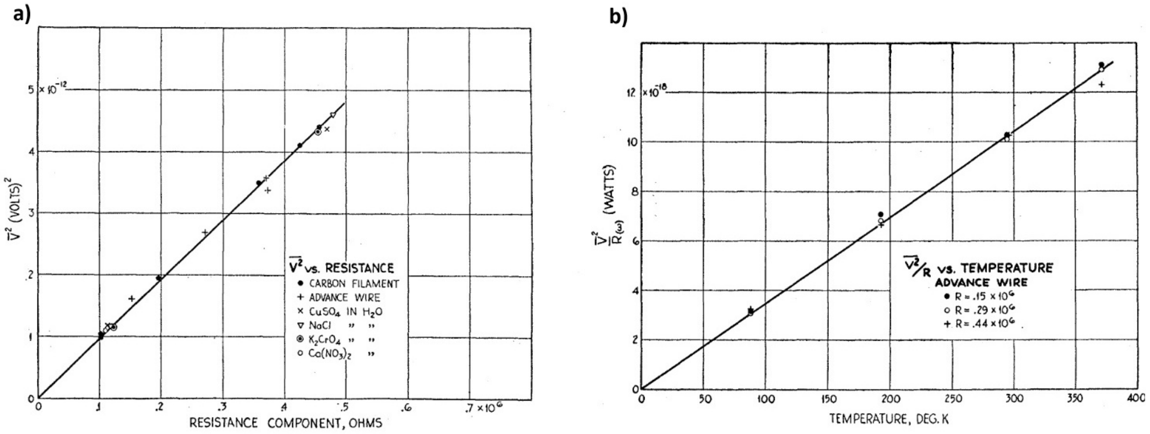

Figure 4.1 : a) Voltage-squared vs. resistance component for various types of conductors. b) Apparent power vs. temperature, for various wire resistances.
[32, Adapted]

resistors (R_1 and R_2) of resistance R connected together via a transmission line length ℓ (Fig. 4.2) and at thermal equilibrium at temperature T. The transmission line is non-dissipative and has impedance $R = \sqrt{\frac{L}{C}}$. Any power dissipated from R_1 to R_2 must be equal to and opposite to the power dissipated from R_2 to R_1 by the second law of thermodynamics. No system can spontaneously produce work from thermal energy.

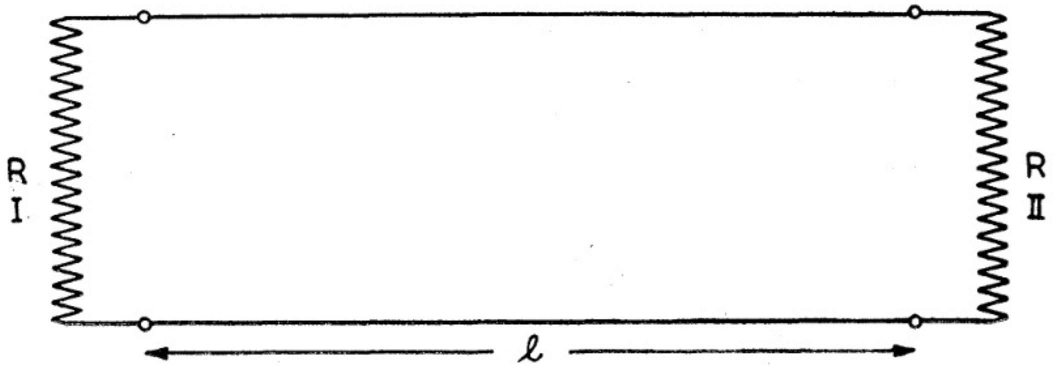

Figure 4.2 : Diagram of two resistors connected by a transmission line of length ℓ.
[33, Adapted]

After equilibrium is achieved, if the two ends of the transmission line are shorted, the resistors are cut off at the two ends. There is now complete energy reflection at the two ends, and the energy is trapped. The transmission line contains standing waves oscillating at natural frequencies $\frac{nv}{2\ell}$, with n being an integer, $n \geq 1$, and v being the propagation velocity. Focusing on a frequency range df, the number of standing modes to be $\frac{2ldf}{v}$. The average energy per mode can then be defined as k_BT by the equipartition theorem, such that k_BT is large compared to the mode spacing, as in the Planck blackbody spectrum. Thus, the total energy contained within the line is $E = \frac{2lk_BTdf}{v}$.

Since no reflection exists, E is the total energy transferred by both resistors during the transit time $t = \frac{\ell}{v}$. The average power transferred at this time is $P = \frac{1}{2}\frac{E}{t} = k_BTdf$. If the total current is given by $I = \frac{V}{2R}$, due to the current generated from resistors R_1 and R_2, then the power is $P = I^2R = \frac{V^2}{4R}$. Equating this to the power determined earlier and solving and substituting for $\frac{V^2}{df} = S_V$ results in

$$S_V = 4k_bTR \tag{4.1}$$

This gives $S_V(f)$, which is the voltage noise power density (V^2/Hz), and can be easily converted to S_I, which is the current noise power density (A^2/Hz), by dividing by R^2 to give

$$S_I = 4k_bT/R \tag{4.2}$$

This derivation is solely performed using a classical approach to the thermal noise. If the proper quantum canonical distribution is considered, the average energy of each mode would be $E = \frac{hf}{e^{\frac{hf}{k_BT}}-1}$ and this gives noise power

$$S_V(f) = \frac{4hfR}{e^{\frac{hf}{k_BT}} - 1} \tag{4.3}$$

If $hf \ll k_BT$ then one arrives back at the classical definition of S_V seen in Eq. 4.1. This gives a cutoff frequency for which the classical version is accurate to. or reference at $T = 1$ K, this gives a cutoff frequency of $\sim 10^{11}$ Hz or $\sim$ 10GHz.

An important feature of thermal noise is that it is frequency independent, i.e., white noise, and can therefore use a large frequency range to average over to determine either R or T. Additionally, thermal noise is only contingent on the real component of the impedance because the transmission line impedance R, due to inductance and capacitance, played zero role in the derivation beyond this illustration.

4.1.1 Thermal Noise vs. Bias in a Nanowire

Thermal noise has many uses in noise spectroscopy. It can be used to accurately measure the resistance if the temperature is known and vice versa. It can also be used to determine the noise floor quality of a noise measurement system and correct for background and determine gain to ensure measurement accuracy. Less commonly, however, it can be used to examine the e-ph coupling in materials, provided that they are shaped into sufficiently narrow nanowires.

When measuring noise in nanowires, the length scales are essential to determine what kind of noise will be measured, as will be expanded upon in Section 4.3. Determining the strength of the e-ph coupling and, in turn, determining the e-ph scattering length l_{e-ph} is very helpful, especially when it can be done in complementary devices. The 1D electron temperature profile $T_e(x)$ can be modeled[34–36] assuming that the contact pads act as reservoirs and are always at the lattice temperature T_{ph}.

$$\frac{\pi^2}{6}\frac{d^2T_e^2}{dx^2} = -\frac{eV}{Lk_B} + \Gamma(T_e^5 - T_{ph}^5) \tag{4.4}$$

With L being the length of the nanowire and Γ being the e-ph energy loss parameter. Eq. 4.4 has the form of a heat-diffusion equation with the terms being, from left to right, the heat diffusion due to a temperature gradient in T_e, energy input due to joule heating, and the last term describing heat loss from the electron to the lattice. The process of determining Γ entails taking an initial guess of Γ and solving for $T_e(x)$

then integrating for the thermal noise across the entire wire for various voltages V.

$$S_V = 4k_B \int_0^L T_e(x) R(T_e) dx \tag{4.5}$$

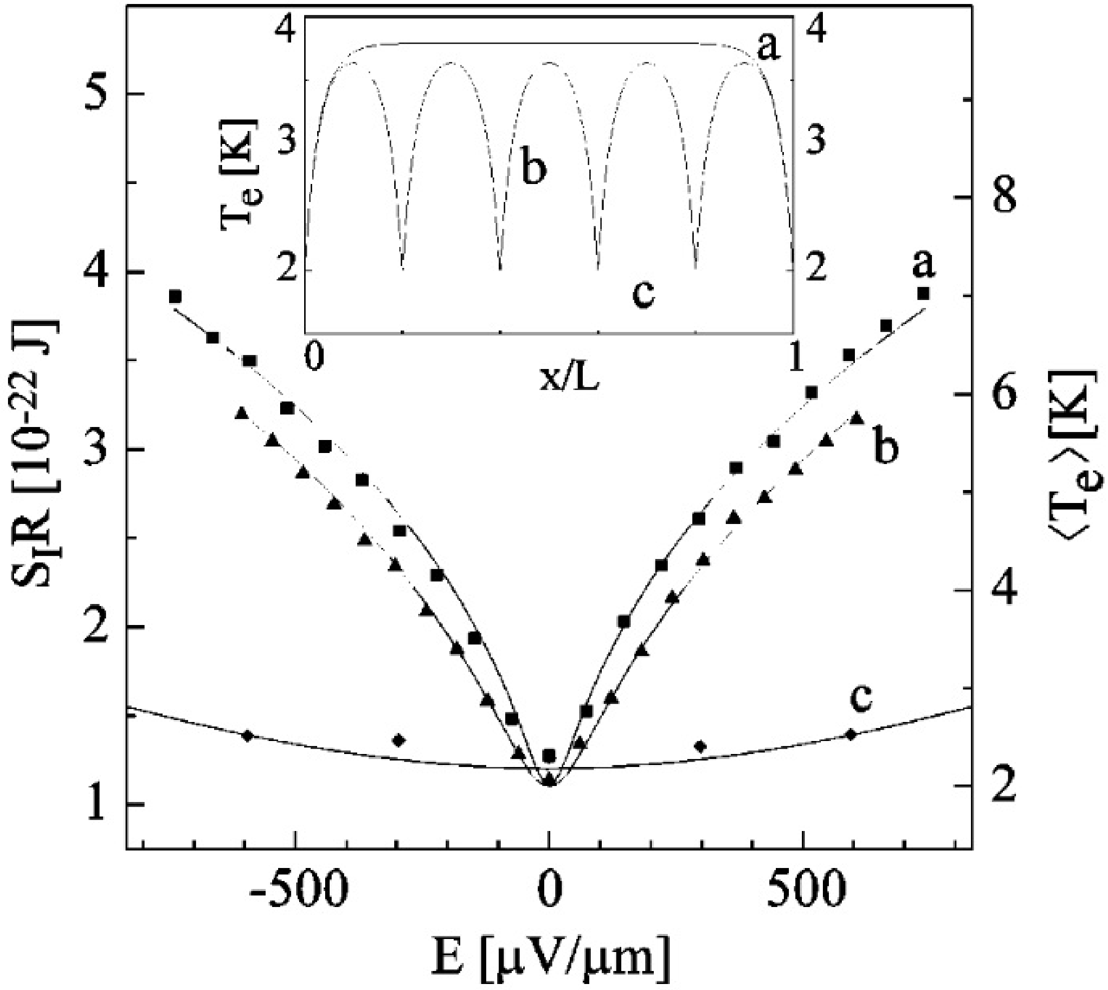

Figure 4.3 : Noise data showing fits on a) 50μm wire b) $5 \times 10\mu$m wires in series and c) $30\times \sim 1\mu$m wires in series. The inset shows the temperature profile for each wire configuration.

[35, Adapted]

If the fittings match the experimental values of S_V vs. V, then Γ has been acquired and can be related to l_{e-ph} via a simple relationship[34,35]

$$l_{e-ph} = 1.31/\sqrt{\langle T_e \rangle^3 \Gamma} \tag{4.6}$$

The calculation can be simplified if $L \gg l_{e-ph}$. Since l_{e-ph} has a values in Au nanowire of several nanometers at low temperatures, $T < 20$ K, a good general guess of wire length is $\sim 30\mu$m. In this regime, one can assume that the T_e is only changing near the pads at can assume that T_e is approximately constant across the wire, thus setting the left-hand side of Eq. 4.4 to zero. This makes the solution trivial and no longer requires numerical solving to obtain S_V at a given V.

$$S_V = 4k_BR\left(T_{ph}^5 + \frac{1}{\Gamma}\left(\frac{eV}{Lk_B}\right)^2\right)^{1/5} \tag{4.7}$$

With this Γ can be simply found via noise measurements making sure to have $L \gg l_{e-ph}$ which simplifies the calculation and removes other sources of noise, such as shot noise (Section 4.3).

4.2 $1/f$ “Flicker” Noise

1/f noise was first observed by John B. Johnson in 1925 while studying the current fluctuations of in a thermionic emission vacuum tube[37]. He noticed a deviation from the theoretical noise (shot noise) expected to be in these devices at low frequency and that the frequency dependence of this noise seemed to increase with decreasing f. Additionally, this noise appeared to exist only under bias and increased with increasing bias. Schottky later suggested that this noise arose from random foreign atoms changing the electron emission of the surface and dubbed it the “flicker effect”[38]. In 1927, Johnson would eventually confirm the $1/f$ dependence on the spectra in 1927[39]. Over the years, this noise phenomenon has been observed in several devices over the years: carbon microphones[40], semiconductors, semimetals, superconductors, and strongly disordered conductors[41].

Due to the appearance of $1/f$ noise in virtually unrelated systems, many attempts have been made to explain it. This has resulted in several explanations and models that work very well on different subsets of materials with $1/f$ but lack the fully comprehensiveness of a universal model. For example $1/f$ does not necessarily mean that the exponent on f is -1; in fact, it has been to found to range from $0.8 - 1.45$[41] across a wide range of materials. To understand $1/f$ noise at its potential sources, I will briefly explain some more popular models.

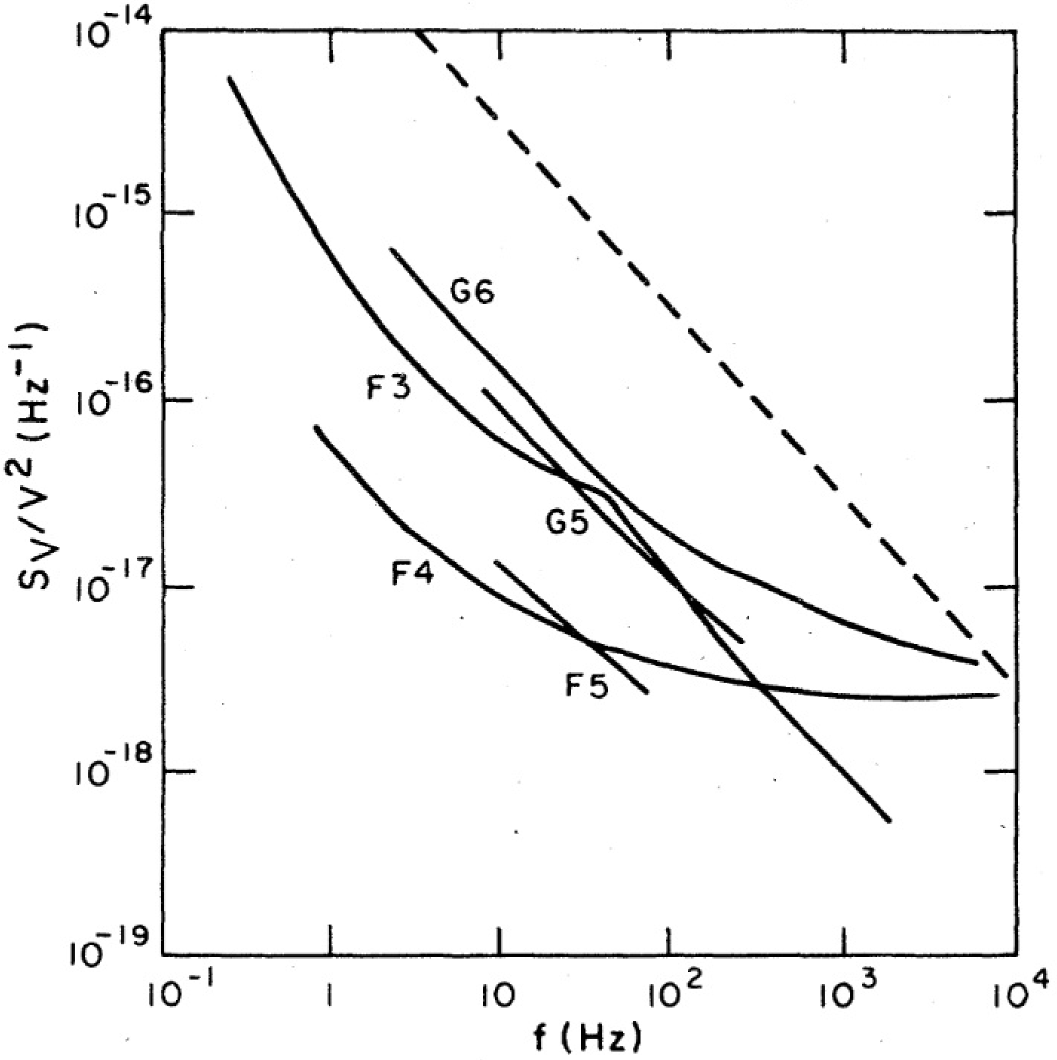

Figure 4.4 : Representative data on InSb samples showcasing the $1/f$ noise dependence on frequency and bias.
[42, Reproduced]

In 1969 F. N. Hooge correlated several experimental data on semiconductor and metal films[43]. He used the generic observations of many that the noise was inversely proportional to f and quadratic related to voltage/current to obtain a universal constant by accounting for the number of charge carriers N_c.

$$S_V = \frac{\alpha}{N_c}\frac{V^2}{f^\gamma} \tag{4.8}$$

Where γ represents slight variation of the exponent around 1 and α represents the Hooge parameter $\alpha = 2 \times 10^{-3}$. The relation to N_c was born of the observation that $1/f$ noise in semiconductors is frequently much larger than that observed in metal films.

Unfortunately, this explanation, while seemingly universal, is easily shown to be inaccurate in many cases. For example, in the Bi samples, there is a strong temperature variation in the spectra where N_c is relatively constant[41]. Additionally, Hooge claimed that the $1/f$ noise is only affected by the bulk of conductors and is independent of the effects of the surface. This contradicts observations that different surface preparations seems to alter the spectra[41,44,45]. Nevertheless, having a crude model for estimation is greatly beneficial and was the beginning of more profound models.

Interestingly, models showcasing defects as a source of $1/f$ noise in semiconductors[46] and metals[47] have had excellent success in describing spectral effects. These models consist of two-level tunneling systems with Lorentzian like behavior[48].

$$S(f) \propto \frac{f_c}{f_C^2 + f^2} \tag{4.9}$$

with f_c indicating a frequency related to the relaxation time of defects acting as charge traps. McWhorter[46] described charge traps deep in an oxide on a semiconductor and Dutta[47] more generally described smaller surface-level charge traps that all lead to conduction fluctuating as electrons are caught and released from traps at characteristic rates. Noticeably, this behaviorfor a single defect leads $1/f^2$. Both found that with an uncorrelated distribution of traps $D(f_c) \propto f_c$ then the noise becomes more

1/f-like.

$$S(f) \propto \int \frac{D(f_c)f_c}{f_c^2 + f^2} df_c \tag{4.10}$$

These traps are set at specific energies and can therefore be thermally activated and "frozen" out as temperature is swept causing the spectra to evolve in temperature[48]. However, even with all the features of these models, there still lacks a universal explanation and instead there are certain easily described situations that these models accurately describe.

Although 1/f noise may not be understood completely, the models have provided a better picture of the causes of this frequently encountered background noise. With the connection to defects, one can imagine passivating these defects such that no charge traps or dangling bonds of any sort. This can be achieved by either engineering perfect defect-free devices, which is incredibly challenging, or filling in surface gaps and dangling bonds possibly via hydrogen passivation[49] though theses processes are not always possible or necessarily helpful in reducing 1/f noise in all systems. Such work is necessary, especially in the world of qubits where 1/f noise leads to the decoherence of quantum states[50].

1/f has been described because it can be a confounding effect when observing shot noise, a useful phenomenon described in the next section.

4.3 Shot Noise

In 1918, Schottky measured the electronic noise in vacuum tubes[51] and discovered a noise source that is independent of frequency and dubbed it the "shot effect" or shot noise. Shot noise originates from the quantized nature of charge carriers and therefore exists only in the presence of an applied current. Schottky was also able to properly define this noise in the classical limit:

$$S_I = 2q\langle I \rangle \tag{4.11}$$

where q is the charge of the charge carrier, and $\langle I\rangle$ being the time-averaged current. This definition only holds in systems with uncorrelated, non-interacting tunneling processes, or in other words, when the charge carriers arrive at the drain at some average rate in a given time window. This is the exact situation described by Poissonian statistics!

For a given time interval, an event can occur any number of times or never. The probability of k events in the interval is described by Poisson probability distribution[52].

$$P(k) = e^{-\lambda \frac{\lambda^k}{k!}} \tag{4.12}$$

Here λ is the mean event occurring in the interval. this can be converted to an average rate r simply by the substitution of $\lambda = rt$, giving

$$P(k) = e^{-rt \frac{rt^k}{k!}} \tag{4.13}$$

This gives the probability of k events in interval t with the events occurring at a mean rate of r. One additional necessary information of the Piossonian distribution is that the variance is equal to the mean.

Substitutions can be made to describe the discharge of a vacuum tube. The events are electrons being discharged across the device; therefore, the rate is $r = \langle I\rangle/e$ and n now defines the number of electrons discharged. I and n are related to each other by $I = ne/t$; therefore, the variance in current $\overline{\Delta I^2}$ is defined as:

$$\begin{align}
\overline{\Delta I^2} &= \overline{\Delta n^2}\left(\frac{e}{t}\right)^2 \tag{4.14}\\
&= \frac{\langle I\rangle}{e} t \left(\frac{e}{t}\right)^2 \tag{4.15}\\
&= \langle I\rangle \frac{e}{t} \tag{4.16}
\end{align}$$

The power spectral densities can be roughly defined as:

$$S_I(f) = 2\frac{\overline{\Delta I^2}}{\Delta f} \tag{4.17}$$

Thus plugging in 4.16 and using the fact that $\Delta f = 1/t$ brings back Schottky's definition.

$$S_I = 2e\langle I\rangle \tag{4.18}$$

For a more formal frequency domain derivation of shot noise, it is recommended to look and follow along this derivation[53], but it is not necessary to comprehend the works in this thesis.

4.3.1 Single Barrier Tunneling Shot Noise

To properly understand shot noise in the simplest terms, it is best to discuss the non-interacting single barrier case. Although it is an ideal case, it still has relevance in several systems and offers an elegant solution. Consider a potential barrier separating metallic contacts, Au-hBN-Au for example. Using the ideas presented in Section 2.3 one can frame this via transmission probabilities.

For simplicity, consider the 1D case at zero temperature. Here, the FD distribution is not smeared at all, and the only noise source is the incident electrons on the barrier, which creates shot noise. Using Landauer-Büttiker formalism shot noise can be represented in this situation as

$$S_I = 2eI\langle \Delta n_{\mathcal{T}}^2\rangle \tag{4.19}$$

If $\langle n\rangle = \langle n_{\mathcal{T}}\rangle + \langle n_{\mathcal{R}}\rangle = 1$ then the averaged fraction of electrons transmitted is $\mathcal{T} = \langle n_{\mathcal{T}}\rangle$ and the fraction of electrons reflected is $\mathcal{R} = \langle n_{\mathcal{R}}\rangle$, where $\mathcal{T}$ and $\mathcal{R}$ are the probability of transmission and reflection, respectively. Additionally, transmission and reflection are inversely related,$\langle \Delta n_{\mathcal{T}} \rangle = -\langle \Delta n_{\mathcal{R}} \rangle$,thus variance of transmitted electrons can then be defined as

$$\langle \Delta n_{\mathcal{T}}^2 \rangle = \langle (n_{\mathcal{T}} - \langle n_{\mathcal{T}} \rangle)^2 \rangle \tag{4.20}$$

$$= -\langle (n_{\mathcal{T}} - \langle n_{\mathcal{T}} \rangle)(n_{\mathcal{R}} - \langle n_{\mathcal{R}} \rangle) \rangle \tag{4.21}$$

$$= -\langle n_{\mathcal{T}} n_{\mathcal{R}} - n_{\mathcal{T}} \langle n_{\mathcal{R}} \rangle - n_{\mathcal{R}} \langle n_{\mathcal{T}} \rangle + \langle n_{\mathcal{T}} \rangle \langle n_{\mathcal{R}} \rangle \rangle \tag{4.22}$$

$$= -\langle n_{\mathcal{T}} n_{\mathcal{R}} \rangle + \langle n_{\mathcal{T}} \rangle \langle N_{\mathcal{R}} \rangle + \langle n_{\mathcal{R}} \rangle \langle n_{\mathcal{T}} \rangle - \langle n_{\mathcal{T}} \rangle \langle n_{\mathcal{R}} \rangle \tag{4.23}$$

$$= -\langle n_{\mathcal{T}} n_{\mathcal{R}} \rangle + \langle n_{\mathcal{T}} \rangle \langle n_{\mathcal{R}} \rangle \tag{4.24}$$

$n_{\mathcal{T}}$ and $n_{\mathcal{R}}$ are orthogonal to one another, since and electron can only either be reflected or transmitted not both. Therefore, $n_{\mathcal{T}} n_{\mathcal{R}} = 0$ giving:

$$\langle \Delta n_{\mathcal{T}}^2 \rangle = \langle n_{\mathcal{T}} \rangle \langle n_{\mathcal{R}} \rangle = \mathcal{T}\mathcal{R} \tag{4.25}$$

Plugging this definition into Eq. 4.19 gives:

$$S_I = 2eI\mathcal{T}\mathcal{R} \tag{4.26}$$

interestingly this is not the same as the Poissonian definition of Eq. 4.18 in fact it differs by a factor of $\mathcal{T}\mathcal{R}$. If generalized to multiple conduction channels, the two equations become:

$$S_I = 2eVG_0 \sum \tau_i(1 - \tau_i) \tag{4.27}$$

$$S_I = 2eVG_0 \sum \tau_i \tag{4.28}$$

The ratio of S_I to the Poissonian becomes

$$F = \frac{\sum \tau_i(1-\tau_i)}{\sum \tau_i} \tag{4.29}$$

The Fano factor F defines the deviation from the pure Poissonian case. The actual noise measured can then be modeled in the low bias using F.

$$S_I = F \cdot 2q\langle I\rangle \coth\left(\frac{eV}{2k_BT}\right) + (1-F)4k_BT\left(\frac{dV}{dI}\right)^{-1} \tag{4.30}$$

Here the at high bias the Equation reduces down to shot noise $S_I = 2Fq\langle I\rangle$ and at zero bias to JN noise. F is an important determinant of features observed in shot noise analysis.

4.3.2 The Fano Factor

The Fano factor is named after Ugo Fano for his statistical work in defining the factor with regard to variance in ionization[54]. It can be used to describe the suppression or enhancement of shot noise in various systems beyond the $2q\langle I\rangle$. The Fano factor can vary in value based on the geometric, and electronic interaction properties of the system. For the context of this thesis, the discussion will be limited to the diffusive nanowire cases.

In the diffusive nanowire regime, it's assumed that the thickness and width are small compared to the length of the nanowire but large compared to the mean free path. Only the length of the nanowire is the relevant parameter to consider. Additionally, it is assumed that a strong electron reservoir is at either end of the nanowire to ensure proper heat dissipation; thus, the transition from the pad to the nanowire must be sharp and not tapered. The dependence of nanowire noise on length is broken into four possible cases, based on Fig. 4.5.

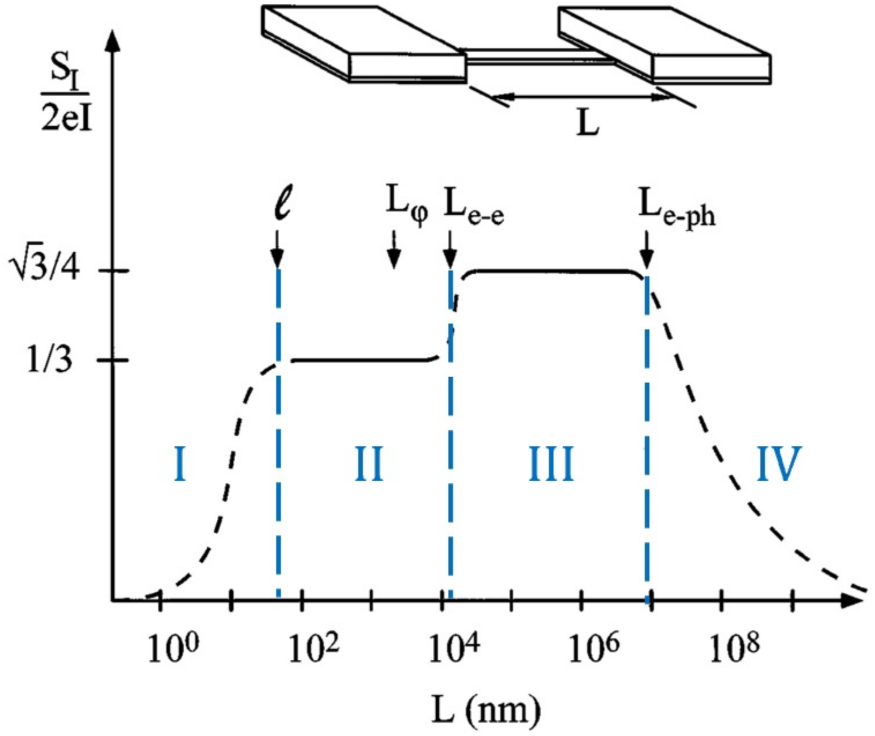

Figure 4.5 : Evolution of the Fano factor as a function of nanowire length. [55, Adapted]

Case I: Beginning with the shortest regime, $L > \ell$, with L being the length of the wire and ℓ being the mean free path of the electrons. The Fano factor decays to zero because the transport is ballistic below ℓ the transport is ballistic which gives an effective transmission coefficient $\tau \sim 1$ due to a lack of scattering causing tunneling events. The Fano factor then quickly approaches zero, as shown by plugging in $\tau \sim 1$ into Eq. 4.29.

Case II: The next regime is $L_\phi < L < L_{e-e}$, with L_ϕ being the phase coherence length and L_{e-e} being the e-e scattering lengths, respectively. In this regime, electrons are hot and unable to thermalize with one another. This lack of thermalization results in the electrons not being thermally distributed in the nanowire interior. Now only the ends are contributing to the resistance thus resulting in a reduction of noise[56]. This noise reduction results in a Fano factor of $F = 1/3$ in this regime. Interestingly the regime $\ell < L < L_\phi$ also gives the same result via mesoscopic theory[57]. This gives a Fano factor of $F = 1/3$ across the regime $\ell < L < L_{e-e}$.

Case III: The third regime is $L_{e-e} < L < L_{e-ph}$, with L_{e-ph} being the e-ph scattering length. Here, e-e scattering establishes a well-defined electron temperature profile $T_e(x)$, as in the last regime, but now can interact . This scattering of the electrons off of one another result in an increase from the independent regime. This increase is attributed to the scattering of electrons, resulting in an increase in the contributing electronic states[58]. As opposed to the non-interacting case, the electrons have a Fermi distribution to describe as opposed to a more step-like distribution as seen in Fig. 4.6. All these contributions result in an increase in the Fano factor from $F = 1/3$ to $F = \sqrt{3}/4$.

Case IV: The final regime is $L > L_{e-ph}$. In this regime, the noise is suppressed toward zero, similar to Case I. The suppression is a result of the electron now being

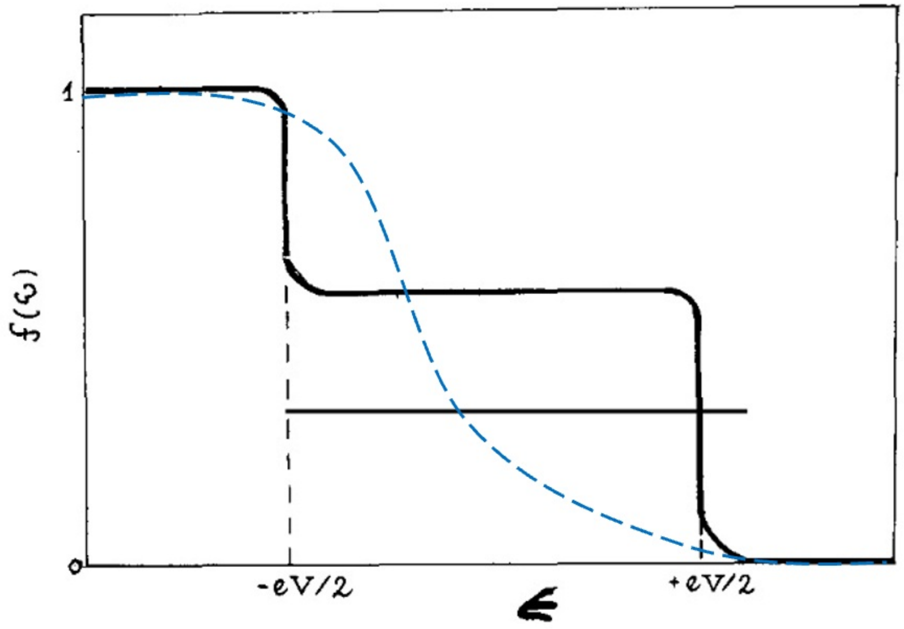

Figure 4.6 : Electron distribution in a nanowire system in the regime $L_\phi < L < L_{e-e}$(solid black line) and $L_{e-e} < L < L_{e-ph}$(dashed blue line). Distribution from contact pad 1 to nanowire to contact pad 2.
[56, Adapted]

able to interact with the lattice via phonon interaction. This reduces the number of electronic states that contribute to shot noise[58]. As L is further increased passed L_{e-ph} the states drop more and more causing the Fano factor to decay from $F = \sqrt{3}/4$ to $F \to 0$. In the limit that electrons are strongly coupled to the lattice vibrations, $T_e(x) \approx T_{ph}$, the noise should always look like JN noise at T_{ph}.

Experimental Methodology

To acquire the data for the topics discussed in this thesis, a combination of experimental techniques is required. The process begins with device fabrication, which is often the most time-consuming part of the process, followed by standard resistance measurements, and concludes with noise spectroscopy measurements. Each aspect is integral to the final result, so this chapter will go into detail about the processes and setup needed to achieve good results with the available tools.

5.1 Device Fabrication

There are three core processes for fabricating the structures used in this thesis: lithography, deposition, and etching. This section will cover each of them in detail and provide explanations of the process flow, equipment used, and tips on commonly encountered issues. These explanations are targeted more toward those who have little to no knowledge of these topics and techniques and will mainly focus on methodology rather than the proper physical mechanisms by which these techniques are implemented.

5.1.1 Photo/ Electron-beam Lithography

Lithography is the process through which micron and sub-micron features can be patterned onto a device. This is done using a special polymer resist that is tuned to have its chains broken by either UV light or electron-beam (e-beam) irradiation. The resist is spun onto a chip at a desired thickness and then exposed and developed into the desired features. Resists come in two forms: positive resist and negative resist, and they are characterized by what happens when the resist is exposed. In the case of positive resist, exposure makes it more soluble in the respective developers. The negative resist works in the opposite way; when exposed, it becomes less soluble in its developer.

Before lithography can properly begin, it is important to know how to clean and prepare chips beforehand. Acetone will clean off any organics left on the chip, possibly resist from previous lithographic processes, and is often accompanied by sonication to ensure cleanliness. Afterwards, chips are often lightly cleaned with plasma in a O_2/Ar plasma cleaner.

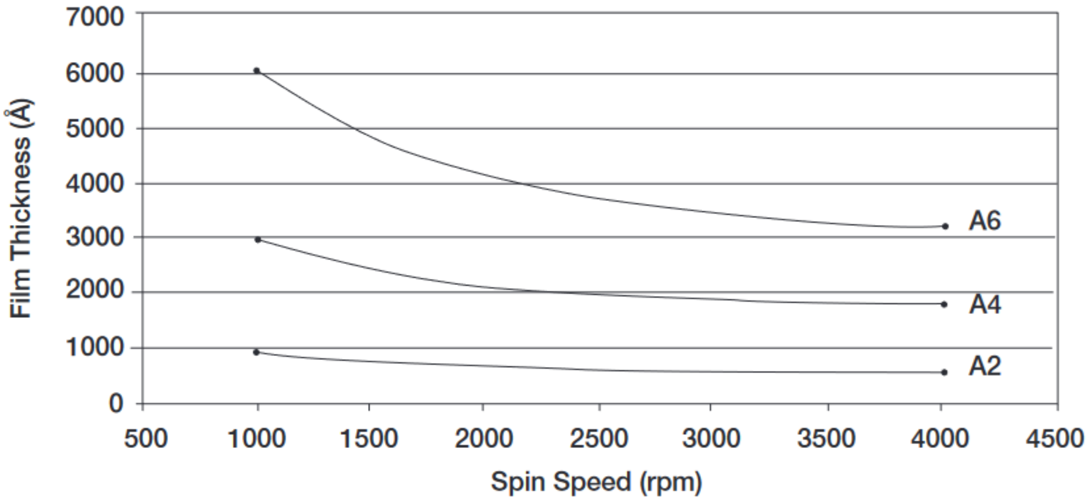

Figure 5.1 : PMMA 495 film thickness v spin speed plot for different resist solutions. [59, Reproduced]

The general process flow of lithography consists of spin coating the resist according to a specified recipe, exposing the resist with a designated pattern, and finally developing the resist. Spin coating parameters are provided in diagrams such as Fig. 5.1 and vary depending on the goal; however, they should generally be maintained within the relatively flat region of the curve for improved uniformity. The exposure of the resist requires a specified dose, which is usually determined through a dose test, which involves an array of doses ranging from underexposed to overexposed, with the ideal exposure falling somewhere in the middle.

One of the most important features to consider, as shown in Fig. 5.3, is the cor-

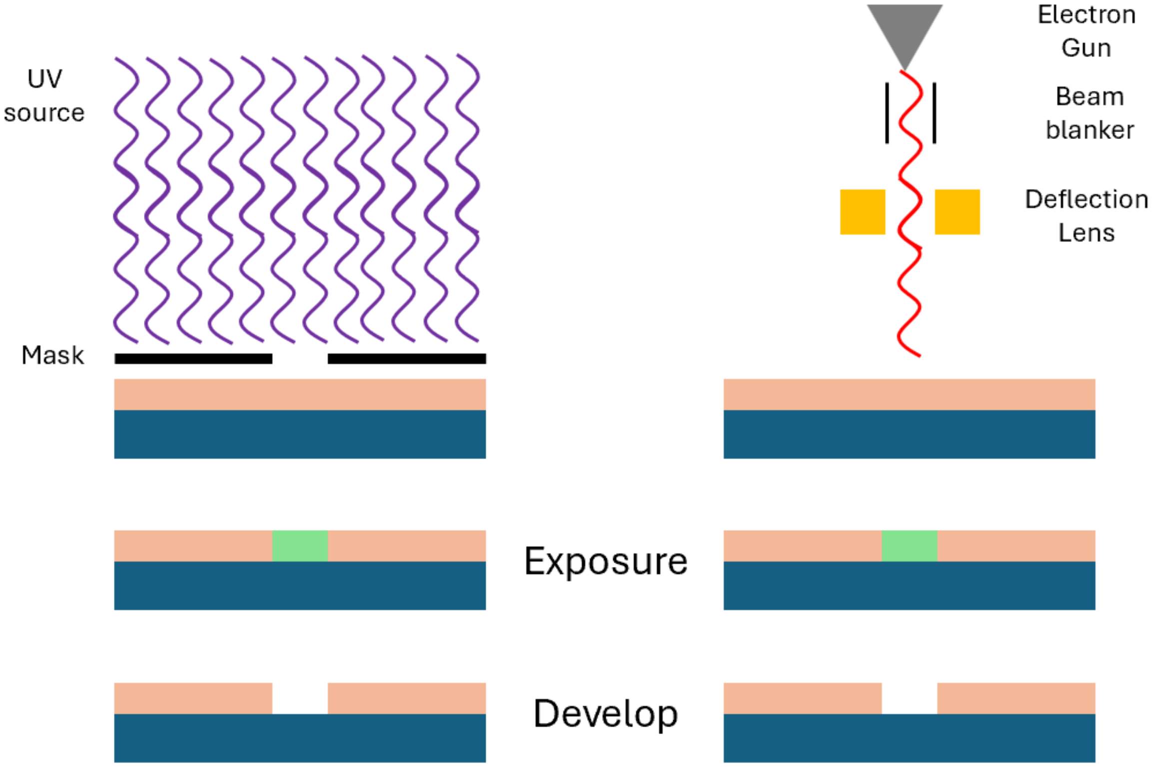

Figure 5.2 : PL and EBL exposure and development process.

ners. If the exposed area is clear, the sharpness of the corners will indicate whether the pattern has been properly exposed. Finally, the development process removes the desired resist. Development time typically does not need to be adjusted during testing processes beyond the manufacturer's recommendations, unless extreme patterns are attempted. Overdevelopment and overexposure can appear very similar, so it is important to vary only one parameter at a time if testing is necessary.

To provide a more detailed explanation of each process, I will begin with an overview of the photolithography (PL) process and its recipe, followed by a discussion of electron beam lithography (EBL).

Photolithography

The PL process generally works by using a photoreactive resist. This photoreactive resist is sensitive to a specific wavelength range, often in the ultraviolet (UV) range.

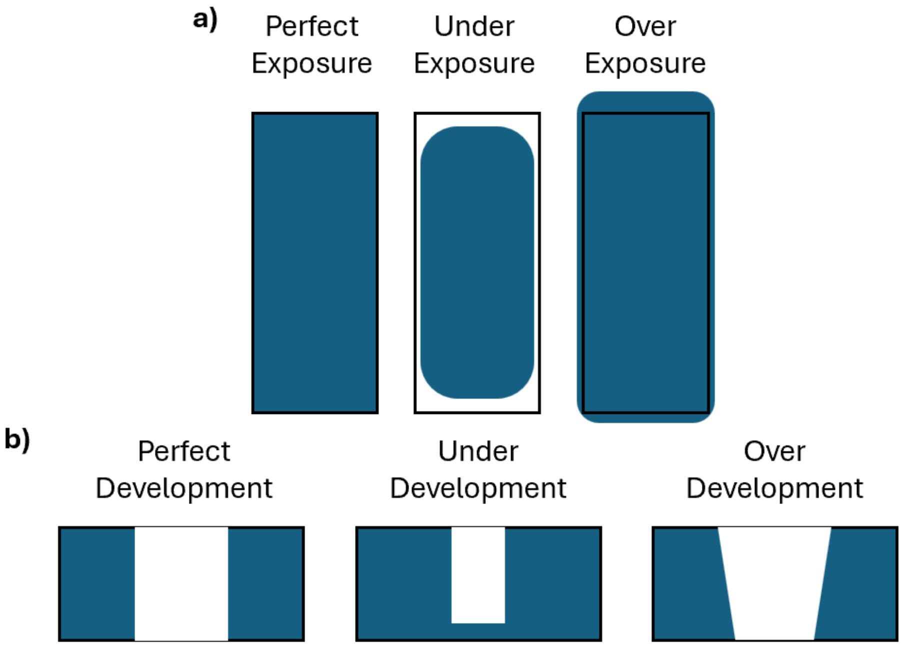

Figure 5.3 : Examples of a) over and under exposure (top view) and b) over and under development (side view).

Therefore, the entire PL process is typically conducted in areas with UV-filtered lights to prevent accidental exposure. The sole control parameter for a given wavelength is the exposure time. The duration of exposure to light controls the "dose" the resist receives, as PL exposure is done via flood exposure, meaning that the entire region is simultaneously exposed.

All PL processes were conducted using the Bruker SF-100 Lightning, a maskless PL system. The term "maskless" in this context refers to the absence of a physical pre-patterned mask laid on top of the resist for flood exposure. The maskless system uses digital micromirrors that reflect the pattern onto the sample. The maskless system can achieve is 2μm. The resist used for device fabrication is Microposit S1818, a positive resist spun at 4000 rpm for 60 seconds. Typical exposure for this recipe in the maskless system is performed at 365 nm for 1 second. Then, the resist is developed in Microposit MF-319/321 for 1 min. This resist and developer combination is very selective; therefore, there is not much concern of overdevelopment.

E-beam Lithography

EBL works by using a resist that is tuned to be sensitive to interactions with a beam of electrons, as opposed to UV light (though at high enough UV energies, it can be used for both). Unlike PL flood exposure, EBL employs single-point beam exposure along a grid of points (preferably equidistant). Therefore, EBL has more parameters to consider beyond just exposure time. EBL has three key parameters: dose per area, often referred to simply as dose (μC/cm^2), beam current (nA), and dose time (μsec/dot). These three parameters are interrelated; defining two of them determines the third. The dose and beam current are the two parameters that are typically controlled, so those will be the focus of the explanation for the EBL process

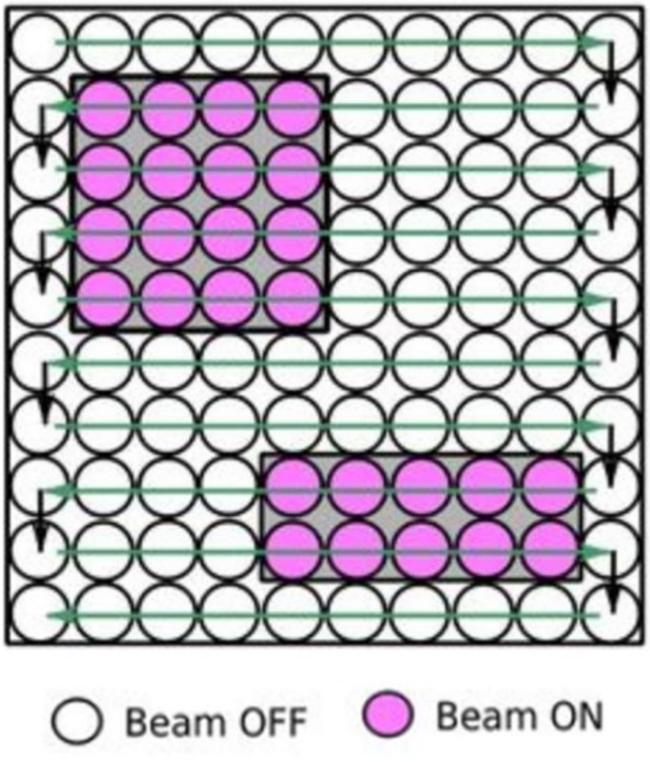

Figure 5.4 : Example of EBL point grid and exposure.
[60, Adapted]

Beam current is a simple concept to understand in terms of how it affects EBL processes. In most cases, a smaller beam current is better. This can be understood by imagining the diameter of the beam when it makes contact with the resist. To fill a square with circles, better resolution can be achieved if the circles are small. Although this is not physically how the process works, it is sufficient to think of it this way for setting up parameters in an EBL design.

This analogy also helps explain cases in which a smaller beam current is not always better, which relates to time management. A proper design is efficient in terms of both time and resolution when needed. For instance, when making large structures like pads, it is much more time-efficient to use a larger beam current, even if it comes at the cost of some resolution.

The general rule of thumb for beam current is: if high resolution is required, a lower beam current is better; however, if resolution is not critical, a larger beam current will save time and improve efficiency.

Dose is a slightly more complicated factor to consider; however, as seen in the previous paragraphs, it is the main parameter that requires attention to finer details. Dose refers to the total amount of electrons hitting an area and varies significantly with the resist and substrate; therefore, what works for one combination may not necessarily work for another. The best way to determine the proper dose for a given combination is to test a range of doses and observe the optimal exposure.

This can be done strategically by creating an array of dose levels for the same pattern, ranging from a value expected to be underdosed to one expected to be overdosed. This array is known as a dose test and should be a standard practice when changing resists or substrates or when creating a pattern with a higher resolution than previously needed.

All EBL processes were performed on an Elionix ELS-G100 with a 100kV e-beam. In most cases, a higher beam voltage results in improved resolution. The Elionix system can achieve resolutions on the scale of tens of nanometers. The resist used for the EBL process is a double-layer positive resist consisting of polymethyl methacrylate

(PMMA) 495 as the first layer and PMMA 950 as the second layer. A double-layer resist offers improved deposition liftoff, as shown in Fig. 5.5, and is always applied in the order where the first layer requires a lower dose than the second layer.

PMMA 495 is spun at 3000 rpm for 40 s, and PMMA 950 is spun at 4000 rpm for 60 seconds. Each layer is baked for 1 min and allowed to cool between layers. After exposure, the resist developed in a 1:3 ratio of methyl isobutyl ketone (MIBK) to isopropyl alcohol (IPA) for 40 seconds. This developer slightly etches unexposed PMMA, so care must be taken when adjusting the development time.

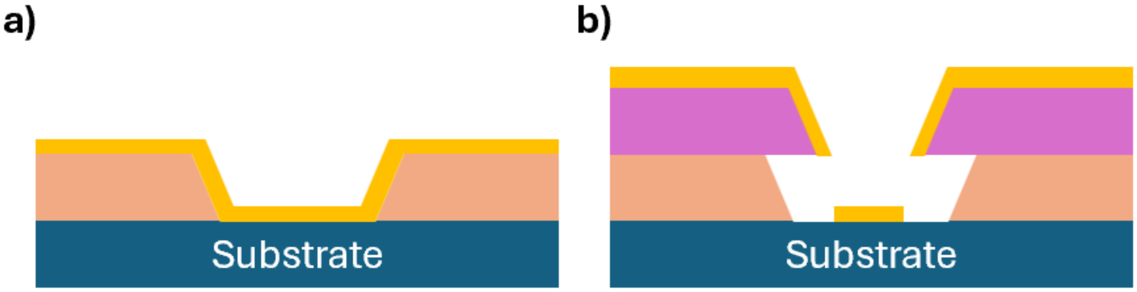

Figure 5.5 : a) Single layer b) double layer resist after development and deposition.

5.1.2 Deposition

A frequent follow-up to the lithographic process is the deposition of materials onto the lithographically defined sections. These depositions often serve as contacts, hard masks, or protective layers and typically consist of various materials chosen for specific purposes. Deposition is commonly performed using one of two methods: e-beam evaporation or plasma sputtering.

In both cases, proper sample preparation is essential. After development, it is recommended to lightly clean the surface with O_2/Ar plasma to improve the adhesion of deposited materials to the substrate. Regarding adhesion, Au is particularly notable due to its widespread use as conductive pads and pathways, while also having poor adhesion to most substrates. Poor adhesion is frequently mitigated with an adhesion layer, often a few nanometers of Ti or Cr. However, even with this adhesion layer, a clean deposition surface is crucial for optimal results.

The deposition process generally involves developing a pattern, depositing the material, and performing a liftoff. Liftoff refers to the removal of the resist that protects the substrate, leaving behind only the material deposited in the shape of the pattern. For effective liftoff, it is important to consider the thickness of the deposited material relative to the thickness of the protective resist. The edges of a resist pattern are typically slanted rather than perfectly vertical; thus, the material can accumulate along the edges and connect the material on top of the resist to that on the substrate surface, as shown in Fig. 5.5a. This issue is the main reason for using a double-layer resist, as it greatly improves the liftoff success rate by preventing the slanted sides from connecting the resist material to that on the substrate.

E-beam Evaporation

E-beam evaporation is one of the most commonly used techniques for depositing simple metals and oxides onto substrates. It uses an e-beam to evaporate crucibles filled with deposition material. This beam is focused and directed via magnetic fields, as shown in Fig. 5.6. An additional oscillating field sweeps the beam across the deposition material surface to promote a more stable evaporation rate by heating a larger area. All these processes occur in a high-vacuum environment to minimize the scattering of evaporated particles and maintain material purity.

The evaporation mechanism can be changed as in the case of thermal evaporation. For thermal evaporation, a crucible is placed between two high-voltage leads and the entire sample is heated through the crucible. It is important to note that some materials cannot be thermally evaporated at a reasonable rate due to the amount of energy required for evaporation. Higher energies can be achieved with comparable input voltages by using e-beam instead of heating. Furthermore, there are materi-

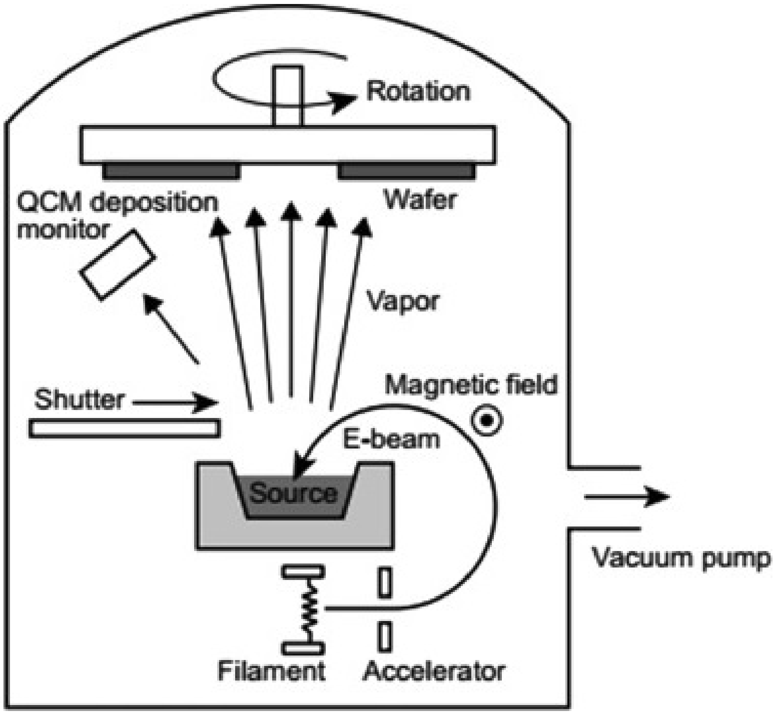

Figure 5.6 : Example of E-beam evaporation mechanism.
[61, Reproduced]

als that are very difficult to e-beam evaporate at which point a different deposition process is needed (possibly sputtering).

While evaporation is essential, it must be performed in a controlled manner, and it is best to measure deposition rates in situ. This is commonly achieved with a quartz crystal monitor (QCM) placed as close to the target substrate as possible. QCMs operate by utilizing the resonant frequency of quartz, which is highly sensitive to changes in mass. As mass accumulates on the QCM, its resonant frequency shifts. If the density and Z-ratio of the deposited material are known, the deposition rate for a specific material can be accurately determined. QCMs are standard tools in deposition systems due to their ease of implementation.

Plasma Sputtering

Sputtering is a technique in which a source material is bombarded with ions, often Ar ions, causing atoms to be ejected or sputtered onto a substrate. Similar to e-beam evaporation, the process is conducted under vacuum with nanometer-sized deposition rates. However, a key difference between material films deposited by e-beam evaporation and those deposited by plasma sputtering lies in the film quality of the source and coating. Because plasma sputtering is a non-thermodynamic process, it can deposit a broader range of materials, more reliably preserving their original composition and stoichiometry. In addition, the coating on the substrate in sputtering is more isotropic, which covers the edges of the resist and makes liftoff more challenging — a problem that can be alleviated with double-layer resist. Sputtered films also tend to have improved adhesion to substrates, likely due to the possibility of in situ plasma cleaning and the more isotropic nature of the film coating.

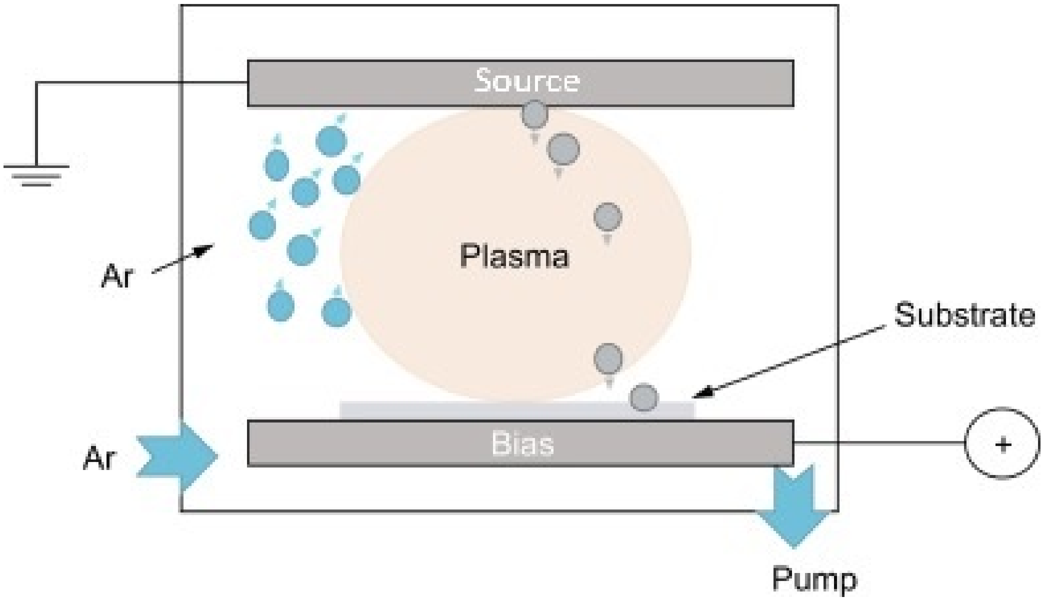

Figure 5.7 : Example of Plasma sputtering mechanism.
[62, Adapted]

5.1.3 Etching

While depositing material onto a patterned substrate is essential, removing material from a patterned substrate is equally important. This removal process, commonly referred to as etching, can take several forms. First, chemical etching occurs when an etchant specific to the substrate chemically reacts with and removes the material. Second, the material can be sputtered away, similar to the sputtering process described above for deposition. Finally, these two methods can be combined to create a process called reactive ion etching (RIE), in which ion bombardment and chemical reactions occur simultaneously.

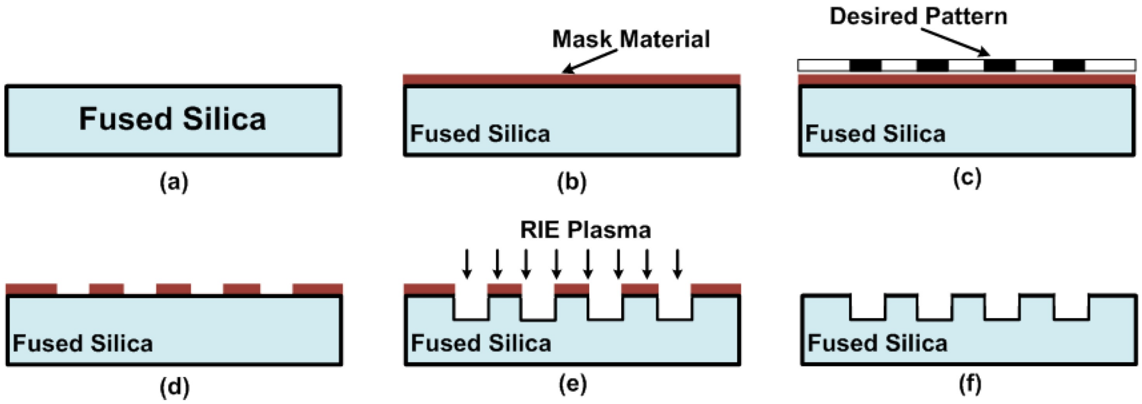

Figure 5.8 : RIE process flow.
[63, Reproduced]

RIE processes in this thesis were performed using the Oxford Plasmalab System 100/ICP 180. Recipes for the etching process in this system will vary depending on the substrate and masks used, but include the same parameters that are important to understand when creating a new etch recipe. Of most importance are the parameters regarding plasma composition and generation. This includes the radio-frequency (RF) power, inductively coupled plasma (ICP) power, and the amount and composition of the gases used for plasma generation. The RF power can be understood as the mechanism that provides direction and accelerates the plasma ions into the target substrate. On the other hand, ICP power provides the energy for the creation of reactive ion species[64]. RF power controls the physical mechanism, and ICP controls the chemical mechanism of the etching process. Finally, the gas composition and quantity, which are controlled by the flow rate, can be varied to give almost selectivity or to improve anisotropy. The general composition is a primary etching gas that targets the substrate, followed by a secondary gas that is versatile in its use. The secondary gas can be used to react with the removed material to improve the etch rate or to dampen the etch rate to a more controllable quantity. With all these core parameters in mind, recipes can be made and understood for fabrication.

The etching process for the devices fabricated in this thesis is often the final step of fabrication. The rest of the substrate and device features must be protected by a mask before etching to prevent unintentional etching. This can be achieved using one of two methods: a hard mask or a soft mask. A hard mask is a material deposited on the surface that is resistant to the etching process or, at minimum, etches more slowly than the target substrate. On the other hand, a soft mask is a photoresist patterned to expose only the areas to be etched. Both types have their uses, but as a general rule, the most important aspect of a mask is its removability following the etch process, unless it is intended to remain on the device. A mask that is resistant to etching but is difficult to remove without damaging the substrate is considered unsuitable.

5.2 Resistance Measurements

Characterization of both the film and the nanowires fabricated from them is important to confirm that fabrication has not altered the properties of the film and to understand the interesting physics of the material at the nanoscale. This section covers some of the various techniques and possible information that they can convey.

5.2.1 Resistance

The resistance measurements are the standard measurement when a multitude of other characterization techniques can be boiled down to. The resistance measurement can be boiled down to applying a known I or V and measuring the others as it passes through a sample. Using the equations defined in Section 2.1 the resistance can be determined from these two quantities.

$$R = \frac{\Delta V}{I} \tag{5.1}$$

$$R = \rho \frac{L}{A} \tag{5.2}$$

From Eq. 5.1 the basis for performing resistance measurements is presented. With this resistance measurement, the resistivity can be backed out. If the length L and cross-sectional area A are known Eq. 5.2 can be used to obtain the resistivity ρ, otherwise a more creative method will need to be used, as discussed in Section 5.2.2.

There are a couple of ways to go about this measurement. A direct current (DC) or an alternating current (AC) approach can be used to measure resistance.

DC measurement

The DC measurement approach is straightforward and can be implemented using a source, a voltage amplifier, a current amplifier, and an analog-to-digital converter (ADC) to record the data. The source is typically a DC voltage source with a series resistance much greater than the expected resistance of the device, which helps prevent damage. This setup effectively converts the voltage source into a current source by introducing a resistor. The current passes through the sample and is fed into a current amplifier, which converts it back into a voltage that the ADC can read.

Because voltage measurements are inherently differential, the voltage amplifier has two inputs connected on either side of the sample and outputs the measured voltage to the ADC. By sweeping the current across a range, a series of points is generated, and the slope of the resulting curve provides the resistance.

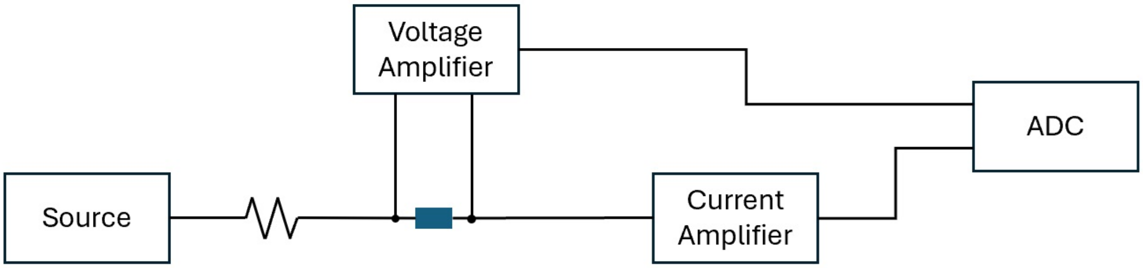

Figure 5.9 : DC resistance measurement setup with a voltage source and the sample as the blue block. The source,voltage amplifier, and current amplifier used are Stanford Research DS345,SR560,SR570 respectively.

This method works well for ohmic samples, meaning that the IV-curve is linear with no curvature. However, in non-ohmic regimes — common in exotic phases — the DC approach is no longer an effective direct measurement technique. In such cases, the AC approach is more suitable for directly measuring the resistance.

AC Measurement

An AC resistance measurement is more accurately described as a measurement of the differential resistance, dR. This method is similar to the DC approach but with a key difference: a sinusoidal AC bias is applied instead of applying a DC bias. This requires the addition of lock-in amplifiers to lock onto the specific frequency of the AC source signal. By measuring V_{AC} and I_{AC}, the differential voltage dV and differential current dI can be obtained.

$$dR = \frac{dV}{dI} \tag{5.3}$$

This can be demonstrated through a Taylor expansion of the sinusoidal output signal V_{out} as a function of the input signal I_{in}. The Taylor expansions are defined as

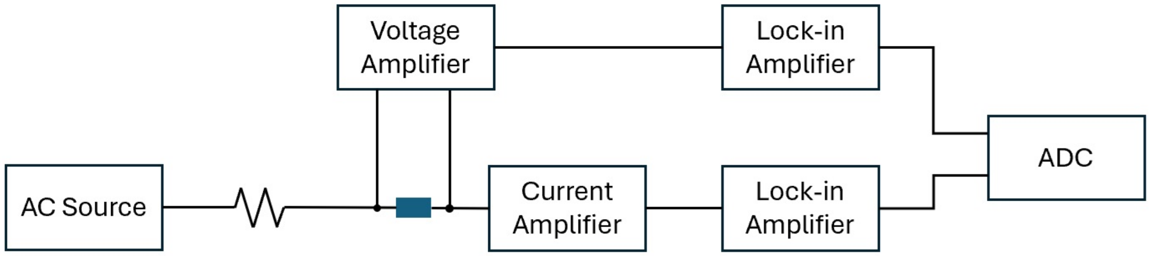

Figure 5.10 : AC resistance measurement setup with an AC voltage source with the sample as the blue block. Lock-ins used are Signal Recovery Model 7270 and 7265

follows:

$$\sum_{n=0}^{\infty} \frac{f^{(n)}(a)}{n!}(x-a)^n \tag{5.4}$$

Let I_{AC} represent the amplitude of the input signal, I_{DC} the dc offset, ω the angular frequency ($\omega = 2\pi/f$), and t be the time.

$$I_{in} = I_{AC} sin(\omega t) + I_{DC} \tag{5.5}$$

The output voltage V_{out} is then:

$$V_{out} = f(I_{in}) \tag{5.6}$$

Expanding V_{out} as a Taylor series yields:

$$V_{out} = f(I_{DC}) + \frac{df}{dI}\Big|_{I_{DC}} I_{in} + \frac{1}{2}\frac{d^2 f}{dI^2}\Big|_{I_{DC}} I_{in}^2 + \frac{1}{6}\frac{d^3 f}{dI^3}\Big|_{I_{DC}} I_{in}^3 + O(4) \tag{5.7}$$

Substituting Eq. 5.5 and applying some trig relations, the higher-order terms can be grouped into the following harmonics:

$$\begin{aligned} V_{out} = &(f(I_{DC}) + \frac{I_{AC}^2}{4}\frac{d^2 f}{dI^2}\Big|_{I_{DC}}) + (I_{AC}\frac{df}{dI}\Big|_{I_{DC}} + \frac{3I_{AC}^3}{8}\frac{d^3 f}{dI^3}\Big|_{I_{SC}}) sin(\omega t) \\ &- \frac{I_{AC}^2}{4}\frac{d^2 f}{dI^2}\Big|_{I_{DC}} cos(2\omega t) - \frac{I_{AC}^3}{24} sin(3\omega t) + O(4) \end{aligned} \tag{5.8}$$

From the first harmonic term, the relationship between V_{AC} and I_{AC} and assuming $f'''(I_{in}) << f'(I_{in})$ can be expressed as:

$$V_{AC} = I_{AC}\frac{dV}{dI}\Big|_{I_{DC}} \tag{5.9}$$

Using the definition of f, combining Eqs. 5.3 & 5.9 gives:

$$dR = \frac{V_{AC}}{I_{AC}} \tag{5.10}$$

This demonstrates that differential resistance and derivatives can be directly measured using an AC source and lock-in amplifiers added to the DC measurement setup.

5.2.2 Van der Pauw Method

The Van der Pauw (VdP) method[65,66] is an incredibly useful method for conducting resistivity measurements on thin films. A conformal mapping technique any closed polygon can be used to perform the VdP method. The measurement scheme only requires the contacts to be placed along four points along the perimeter, preferably at corners or roughly equidistant from one another, as shown in Fig. 5.11.

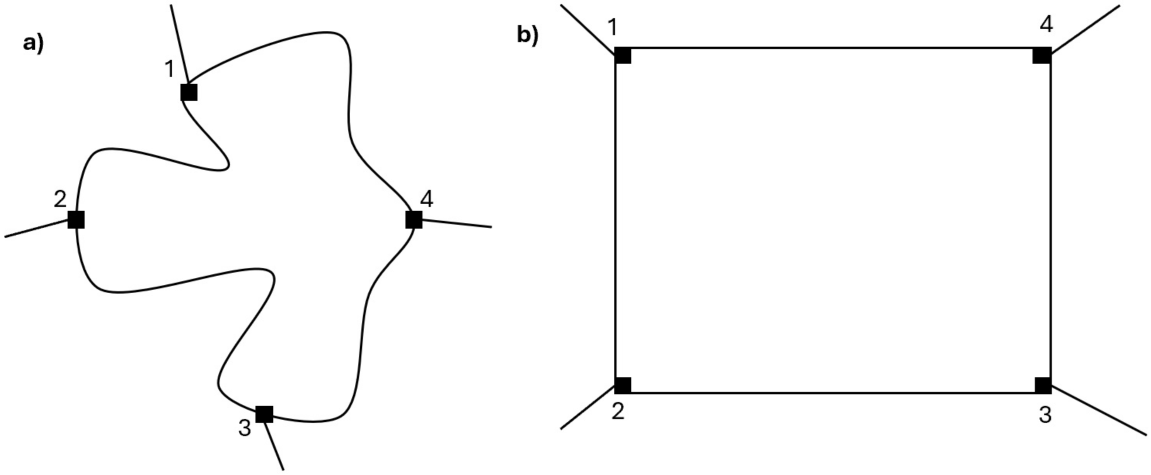

Figure 5.11 : Example of valid connection setups for a VdP measurement with a) arbitrary polygonal and b) rectangular sample.

The measurement consists of two separate resistance measurements along the perimeter. In the first configuration, the current is passed between pads 1 and 4 I_{14} and voltage is measured along the opposite edge between 2 and 3 V_{23} to obtain a resistance $R_{14,23}$ (referenced in Fig. 5.11b). The second configuration is then measured using current I_{12} and voltage V_{43} for a resistance $R_{12,43}$. With the resistances measured here, the resistivity can be determined by solving for ρ with t being the film thickness.

$$e^{-\pi R_{14,23}t/\rho} + e^{-\pi R_{12,43}t/\rho} = 1 \tag{5.11}$$

In general Eq. 5.11 is not analytically solvable for ρ, except in the special case of $R_{14,23} = R_{12,43}$[67], and an iterative approach is needed to properly solve the equation. The Newton-Raphson method can be used to solve the VdP formula for ρ.

The Newton-Raphson method begins with the iterative equation.

$$\rho^{+} = \rho - \frac{f(\rho)}{f'(\rho)} \tag{5.12}$$

$f(\rho)$ and its derivative are defined from Eq. 5.11 as

$$f(\rho) = 1 - e^{-\pi R_{14,23}t/\rho} - e^{-\pi R_{12,43}t/\rho} \tag{5.13}$$

$$f'(\rho) = -\frac{\pi t}{\rho^2}(R_{14,23}e^{-\pi R_{14,23}t/\rho} + R_{12,43}e^{-\pi R_{12,43}t/\rho}) \tag{5.14}$$

Using some substitutions for simplification.

$$s = e^{-\pi t/\rho} \tag{5.15}$$

$$R_1 = R_{14,23} \tag{5.16}$$

$$R_2 = R_{12,43} \tag{5.17}$$

Eq. 5.12 becomes

$$\rho^{+} = \rho + \frac{\rho^{2}}{t\pi} \frac{1 - s^{R_1} - s^{R_2}}{(R_1 s^{R_1} + R_2 s^{R_2})} \tag{5.18}$$

This offers a nice formulaic solution that converges quickly into the true value of the film resistivity.

5.2.3 Cryogenic Systems

Liquid He is commonly used to perform low-temperature experiments. Liquid He was first achieved in 1908 by Heike Kamerlingh Onnes[68]. He comes in two main isotopes ^{4}He and ^{3}He. ^{4}He is the most abundant of the two and liquefies at 4.2K and becomes a superfluid at 2.17K. ^{3}He is substantially rarer than ^{4}He and liquefies at 3.2K and becomes a superfluid at 1mK. Since ^{4}He is the more common of the two, it is most commonly used in helium pumps to go down to 4.2K or below if it is pumped on to remove the boiled off He.

All noise measurements and most resistance measurements were performed using the Quantum Design Physical Properties Measurement System (PPMS). The PPMS system consists of a He detector with several vacuum jackets and a liquid nitrogen jacket, a maximum 9T superconducting magnet, and a reliquefies for recycling boiled-off helium. Samples are placed in a central sample space in the middle of the magnet. The temperature within the system can be varied from 1.9K-400K.

In cases where temperatures below 1.9K are required, a ^{3}He/^{4}He dilution refrigerator can be used. A dilution refrigerator provides cooling power via mixing of the superfluid ^{4}He and liquid ^{3}He. This works via a phase separation of a dilute and concentrated ^{3}He phase and the exchange of ^{3}He across the phase boundary being endothermic.

5.3 Noise Spectroscopy

Noise spectroscopy measurements can elucidate many properties of materials as seen in Chapter 4. These noise measurements can often be difficult to isolate the desired noise. Proper noise setup implementation and measurement techniques are necessary to acquire accurate data. This section will cover how to take noise measurements and calibrate the setup to ensure accurate data collection used in previous publications[69, 70].

5.3.1 Setup

The noise setup used in this thesis is a low-frequency (low-f) noise measurement setup with the upper bound of frequency being 5MHz, set by the oscilloscope. In this setup, the voltage noise is measured and amplified to ∼ x10000 across each chain. Bias often needs to be applied and is sourced from an NI-Daq split across channels and heavily filtered by low-pass filters. The two channels shown in Fig. 5.12 is used for cross-correlation of the signals to help reduce the noise resulting from the amplifiers.

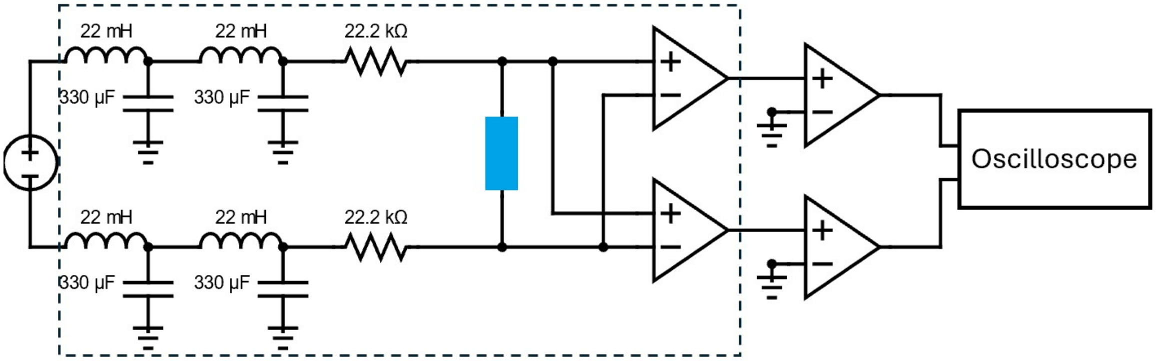

Figure 5.12 : Circuit diagram of the low-frequency noise measurement setup. The dashed line indicates the components within a Faraday cage. Sample is indicated by the blue device. Amplifier chains consist of an LI-75A followed by an SR560 in differential and single modes. The oscilloscope used is the Picoscope 4262.

Cross-correlation is a technique that helps reduce the overall noise of a system by comparing and amplifying the correlated noise of two channels and reducing the unrelated noise of an individual channel. To demonstrate how this works[71] let the voltage in channels 1 and 2 be expressed as follows:

$$v_j(t) = s(t) + w_j(t) \tag{5.19}$$

where $s(t)$ being the shared correlated signal between the two channels and $w_j(t)$ be the uncorrelated noise in channel j. The power spectral function $S_v(f)$ is defined as the Fourier transform of the autocorrelation function (r):

$$S_v(f) = \mathcal{F}\{r(\tau)\} = \sum_{\tau=-\infty}^{+\infty} r(\tau)e^{-i2\pi f\tau} \tag{5.20}$$

The cross-correlation function is the autocorrelation function except with 2 different channels instead of a single channel. Thus, r can be defined as:

$$r(\tau) = r_{12}(\tau) = E[v_2(t) \cdot v_1(t+\tau)] \tag{5.21}$$

Because $w_1(t)$, $w_2(t)$, and $s(t)$ are uncorrelated from one another it can be estimated in the case of N samples:

$$\tilde{r}_{12}(\tau) = \frac{1}{N}\sum_{t=0}^{N-1} v_2(t) \cdot v_1(t+\tau) \tag{5.22}$$

Then, an estimate of $S_v(f)$ is

$$\tilde{S}_v(f) = \frac{1}{N}\sum_{\tau=-(N-1)}^{N-1}\sum_{t=0}^{N-1} v_2(t) \cdot v_1(t+\tau)e^{-i2\pi f\tau} \tag{5.23}$$

$$\tilde{S}_v(f) = \frac{1}{N}\sum_{t=0}^{N-1} v_2(t) \cdot V_1(f)e^{i2\pi ft} \tag{5.24}$$

$$\tilde{S}_v(f) = \frac{1}{N}V_1(f) \cdot V_2^*(f) \tag{5.25}$$

Taking only the real component of $\tilde{S}_v(f)$ removes half of the uncorrelated noise power, improving the signal to noise (SNR) ratio further. Because $s(t)$ is present equally in both channels, it has no imaginary component, and the linear combination of $w_1(t)$ and $w_2(t)$ results in a complex value.

Cross-correlation helps to lower the noise floor of the system by introducing two identical channels, but it is still important to get each individual channel as quiet as possible to further lower the noise floor. Therefore, proper shielding, grounding, and a high-quality low-noise first-stage amplifier are essential. The first-stage amplifier, sample, and low-pass filters are all within Faraday cages to help reduce the interference of the external electromagnetic signals of the lab environment with the noise signal. The first-stage amplifier and the probe to which the sample is connected are isolated from the cryostat system and are on their own grounds to offer a cleaner ground. Finally, the first-stage amplifier is a good quality LI-75A low-noise amplifier that comes with a silent power source from NF corporation and is the biggest limiter in the quality of the noise signal. An improvement in the first-stage amplifier (made quieter, or cooled to reduce thermal noise) will result in a significant reduction in the noise floor of the system.

The probe used in the noise measurements was a custom probe designed and made by Liyang Chen, a lab alumnus. It consists of a hollow stainless steel body to reduce thermal conductivity while maintaining electrical conductivity to act as a Faraday cage to the wires inside. The rod is connected to the top vacuum seal/ LEMO connection via a spring to reduce rod flexion and stress on the bottom slot of the PPMS system. On the other end of the rod is the copper sample housing, which is wrapped in aluminum foil during measurements to shield the sample from potential noise inside the PPMS system. The rod is connected to a thermal sink in the PPMS bottom slot via a pinless connector. The connector is attached to the sample housing via a screw and nut with insulating buffers to prevent the electrical

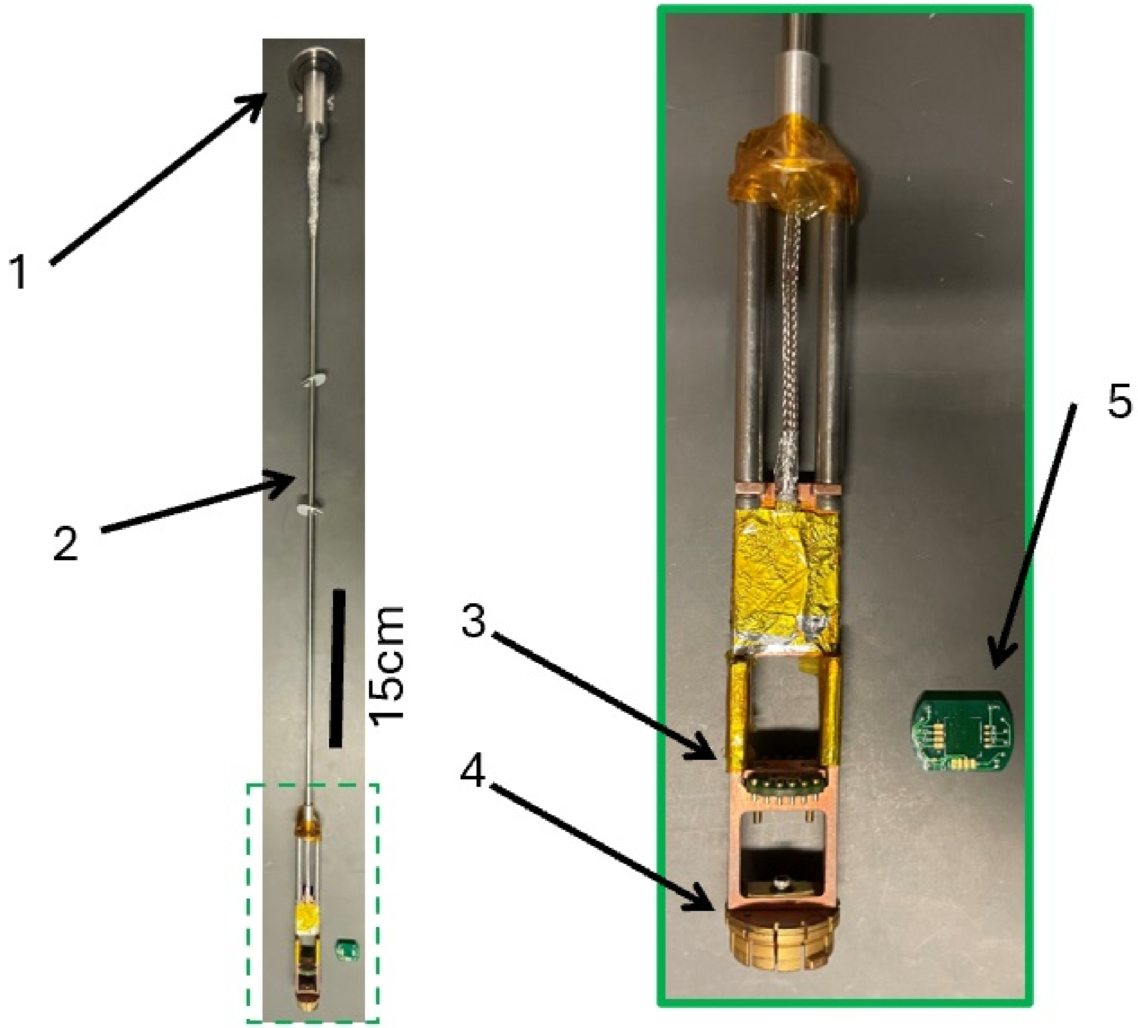

Figure 5.13 : Noise probe **1)** Vacuum cap with LEMO connection. **2)** Stainless steel rod with low-temperature wires inside connected to the vacuum cap via spring. **3)** Sample holder insertion. **4)** Thermal connection to the PPMS bottom (electrically isolated). **5)** Sample holder.

connection between the bottom PPMS slot and the sample housing.

5.3.2 Measurement & Calibration

Measurements are controlled via a Labview program that reads and cross correlates two channels. This is averaged over several times (often 300 times) into the final signal. Data are often taken over several runs of increasing voltage, with voltage reset between runs, and further averaged to improve the SNR. The raw data are outputted into frequency and arbitrary unit noise data, which are converted into V^2/Hz via a prior calibration to determine the appropriate conversion.

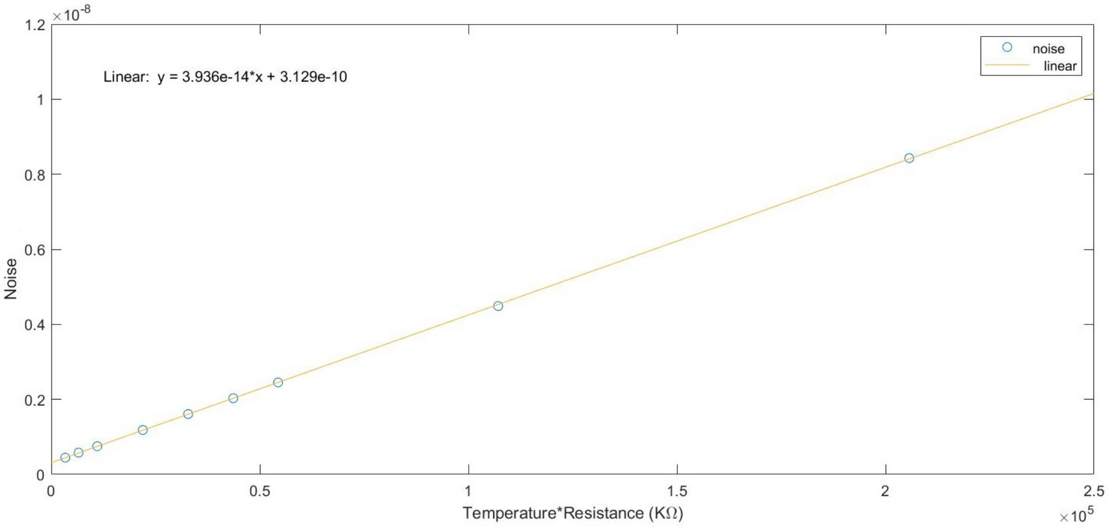

Figure 5.14 : Example of calibration data using a test 1 kΩ resistor with noise taken at temperature values of 3, 5, 7, 10, 20, 30, 50, 100, and 200 K.

Calibration consists of a series of thermal noise measurements of various resistors at various temperatures shown in Fig. 5.14 . Using the definition of thermal noise (Eq. 4.1) the calibration fit equation is:

$$S_v = A4k_B \cdot TR + S_o \tag{5.26}$$

A corresponds to the actual gain of the system, which should be of order of all amplifier gains multiplied together. S_o is the background noise inherent in the system resulting from the amplifiers and the imperfect nature of the cross correlation technique. This gives the correction to the arb. units of the raw data to convert into the real values of V^2/Hz. It is recommended to perform calibration using multiple resistors at different temperatures or, in the event that a specific device calibration is needed, a single resistance value at several temperatures up to at least 200 K. Notably, this calibration is necessary to repeat if the system is changed. Common examples are: change in cable length, new amplifiers, changing of series resistors, and any changes in the probe.

All noise measured in this thesis is white noise and should therefore be flat. It is not necessary for the entire spectra to be flat as there is often $1/f$ noise present below $\sim$ 3kHz and RC decay is often present at high frequencies due to parasitic capacitance in the system. A sufficiently large region of flat spectra is the only thing necessary for proper data analysis. To that end it's important to diagnose stray peaks in the spectra, particularly at low resistances and low temperatures, to measure the noise floor of the system. Diagnostic approaches can be as simple as swapping amplifiers if an amplifier is failing or as complicated as scouring the lab for a new noise source with a special probe made from many loops of wire on the end of a rod connected to the noise setup to pick up signals in the target frequency range.

In addition to the minimization of issues in the noise setup, it is recommended to have dedicated cables and amplifiers to ensure that the signals being measured are consistent with the calibration performed before and to reduce concerns of minor errors causing effects. It is also recommenced to connect to devices via a 4-terminal measurement setup if possible, or a pseudo-4-terminal setup if not. The pseudo-4-terminal setup refers to the use of two wires on each pad in a 2-terminal measurement setup to remove any resistance sources before the contact pads. Ensuring proper accuracy of noise measurements and minimization of issues is an art form and essential for achieving proper and repeatable noise spectroscopy measurements.

Subcoherence Quasiparticle Properties in $YbAl_3$ Nanostructures

$YbAl_3$ is a prototypical heavy fermion material that has been measured and discussed since the 1970s[72,73]. $YbAl_3$ is mixed valence system which means that the Yb ions are present in two oxidation states within the compound, Yb^{3+} and Yb^{2+}[72]. This mixed valence state exist due to the $4f$-electron energy levels existing in proximity to the Fermi energy, the highest allowed energy at in a system at zero T. This results in fluctuations in the valence behavior resulting in complex electronic interactions.

As mentioned $YbAl_3$ is a heavy fermion with f-level valence electrons resulting in it being well described by the Kondo physics discussed in Section 3.1. The single-ion Kondo temperature for $YbAl_3$ is $T_K \approx 670$ K[74], meaning that the measurements done in this chapter, $T \leq 20$ K, are firmly in the Kondo regime. The heavy fermion coherence — that is the T^2 R-dependence — occurs at $T^* \sim 37$ K[75]. This coherence point implies fully well-defined quasiparticles and offers an effective mass $m^* \approx 25$ - 30 m_e[76]. This coherence has yet to be properly quantified in any heavy fermionic materials most likely owing to a lack of thin filmed materials required for mesoscopic measurements.

In addition to the heavy fermionic behavior, $YbAl_3$ also has unusual interaction between the electrons and the lattice. Calculations of the thermoelectric effect in $YbAl_3$[77], suggest that the phonon drag contribution to the Seebeck response is strong, implying a strong coupling between the conduction electrons and the phonons. Inelastic neutron scattering measurements[78] also show that there is strong resonance f-electrons and the optical phonons of the aluminum atoms near 32 - 35 meV. At the same time below T^*, $YbAl_3$ experiences a negative thermal expansion, one that isn't seen in it's nonmagnetic cousin $LuAl_3$[79]. Theory[80] suggests the negative thermal expansion is resultant of of the continued evolution of the f-electron hybridization below the T^* and the renormalization of the the phonon frequencies that coincides as the temperature continues to drop below T^*. This negative temperature thermal expansion has strong temperature variation coinciding with the unusual e-ph coupling.

Previous measurements of bulk $\mathrm{YbAl_3}$ have found the low temperature coefficient of electronic specific heat[72] to be $\gamma = 45\ \mathrm{mJ/K^2 \cdot mol}$. From the lattice constant od 4.20Å,the volume coefficient of electronic specific heat is $\gamma_V = 1.01 \times 10^3\ \mathrm{J/K^2m^3} = (\pi^2/3)k_B^2 g(E_F)$, in the sommerfield picture where $g(E_F) \approx 1.6 \times 10^{48}\ \mathrm{J^{-1}m^{-3}}$ is the density of states at the Fermi level. From the Einstein relation $1/\rho_{0,f} = e^2 D g(E_F)$, the diffusion constant for carriers in the film is $D \approx 5.0 \times 10^{-5}\ \mathrm{m^2/s}$. Measurements of the deHaas-van Alphen oscillations in single crystals[81] have found an effective mass for the low temperature $\mathrm{YbAl_3}$ heavy carriers $m_e^* \approx 23 m_e$; within a Sommerfeld model, combining this with $g(E_F)$ gives a Fermi velocity $v_F \approx .2 \times 10^4$ m/s, consistent with other reports[82]. Assuming 3D diffusion in the thin film, the elastic mean free path inferred from D,v_F, and the residual resistivity is $\ell_f \approx 3.5$ nm.

With the increased interest in thin filmed strongly correlated materials, mesoscopic measurements are now available to elucidate the complex behavior in the heavy fermion $\mathrm{YbAl_3}$[83]. Magnetotransport measurements of mesocopic wires fabricated from epitaxial $\mathrm{YbAl_3}$ films reveal both WAL and UCF effects at temperatures well below the coherence onset. Observations of these phenomena allow detailed analysis of L_ϕ for quasiparticles[7,84] of which hasn't been done prior. Mesoscopic wires also allow noise measurements of JN noise in $\mathrm{YbAl_3}$ revealing anomalous e-ph energy loss (Γ) from 3-20 K via bias dependence in the noise.

6.1 Device Fabrication

The $\mathrm{YbAl_3}$ films were grown via molecular beam epitaxy (MBE) by Kyle Shen's group at Cornell University[75]. Fig. 6.1a shows the film stack which was grown on a MgO substrate with a buffer layer 5 nm of $\mathrm{LuAl_3}$, to reduce stress via lattice matching, and 15 m, of $YbAl_3$. The Lu ions have a full 4f shell making it magnetically inactive and therefore has little effect on the properties seen at lower temperatures that are dominated by the partially filled Yb ions as shown in Fig. 6.1b.

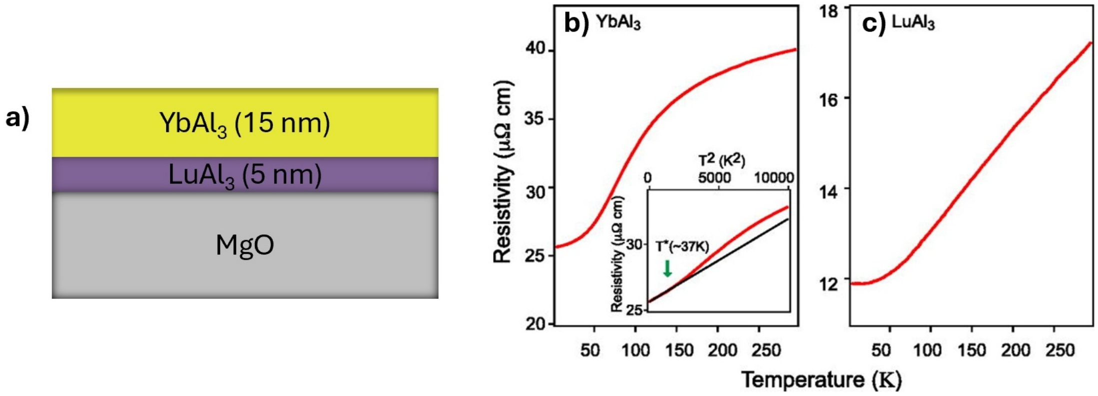

Figure 6.1 : Film stacking information. a) Stacking diagram of the $YbAl_3$ films. Resistivity data of b) a mixed $YbAl_3$ (YA 20 nm/LA 1.6 nm/Al 1.2 nm) stack showing difference from c) a pure $LuAl_3$ resistivity showcasing how the $YbAl_3$ features dominate the electronic properties at low-T.
[75, Adapted]

The epitaxial $YbAl_3$ films were fabricated into nanowires via EBL, Fig. 6.2. First the contacts are defined using EBL, then a layered deposition — consisting of 5 nm Ti + 80 nm Au + 32nm Cr — is put down via e-beam evaporation and subsequently lifted off to define the contact pads. A second lithographic step then defines the wire and a mask — 60 nm Ge +40 nm Cr — is deposited to protect from etching at a later step and subsequently lifted off to create a wire of Ge/Cr on the surface of the $YbAl_3$ film. Ge is used here due to all chemical etchings of Cr attempted, Cr etchant and HCl, damage the $YbAl_3$ film. A window is then opened up around the entire device using photolithography to protect the rest of the film from the etching process that will define the wire and electrically isolate the device from the rest of the film. Etching is of the film is done using a Ar in an Oxford Plasmalab System 100/ICP 180 RIE. The parameter specifics of the $YbAl_3$ etch are: 14 mTorr pressure with 35 sccm flow rate of Ar at 13°C. RF and ICP powers are 120 W and 200 W respectively. The etch is done with an etch rate of ~ 5.9 nm/min to etch away approximately 35 nm of the 20 nm film. The Cr hard mask on the pads are calibrated to be completely eaten through by the etch leaving behind the pure Au of the pads. For the wires, a little bit of Cr is left behind but is not a conductive path between the pads due to the residual Ge/GeO$_x$ buffer layer that is left on the wire after etching that at low temperatures is several orders of magnitude more resistive than the YbAl$_3$ wires.

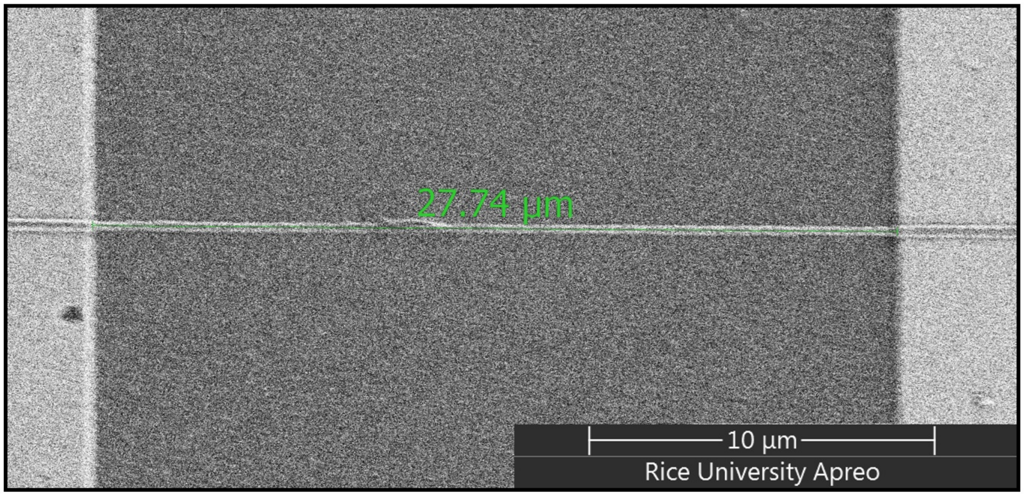

Figure 6.2 : Image of a representative $\sim 30\mu$m YbAl$_3$ via scanning electron microscopy (SEM)

6.2 Device Quality Measurements

Following device fabrication, both $R(T)$ and the magnetoresistance (MR) at various T are measured to ensure that the device maintains the heavy fermionic properties seen in the bulk single crystals. The $R(T)$ of a representative 29 μm × 160 nm wire is shown in Fig. 6.3a. Below T^* the resistance of the wire is expected to behave quadratically of the form

$$R(T) = \left(\frac{L}{wt}\right)\left(\rho_{0,w} + A_w T^2\right) \tag{6.1}$$

with L being the length of the wire, w being the width, and t being the thickness of the film stack. The residual resistivity is $\rho_{0,w} \approx 103.6\ \mu\Omega \cdot \mathrm{cm}$ which compares to the film resistivity, before fabrication, $\rho_{0,f} \approx 48.5\ \mu\Omega \cdot \mathrm{cm}$. This is quite a bit higher but is not too surprising given the increased disorder of fabricating a nanowire. This argument is further confirmed when comparing the $\rho_{0,f}$ is compared to the bulk[85] $\rho_{0,b} \approx 1.3\ \mu\Omega \cdot \mathrm{cm}$ and to thicker films of residual resistivity of 26 $\mu\Omega \cdot \mathrm{cm}$[75], indicating that increased disorder of scaling down dimensions and fabrication results in an increased ρ_0. The coefficient A_w should remain largely unchanged as the Fermi liquid behavior needs to be maintained through fabrication. Indeed this is the case as $A_w \approx 1.9 \times 10^{-3} \pm 0.1 \times 10^{-3}\ \mu\Omega \cdot \mathrm{cm/K}^2$ is very similar to $A_f \approx 1.7 \times 10^{-3}\ \mu\Omega \cdot \mathrm{cm/K}^2$, both taken from fitting below 30 K data from Fig. 6.3 These resistivity measurements ensure that the heavy fermion state is maintained in the wires fabricated. Additionally calculation of mean free path with the new $\rho_{0,w}$, assuming no changes in the actual electronic structure of the material — $g(E_F)$, v_F, etc. — gives $\ell_w \approx 1.7$ nm with a inferred diffusion constant of $D_w \approx 2.3 \times 10^{-5}\ \mathrm{m}^2/\mathrm{s}$.

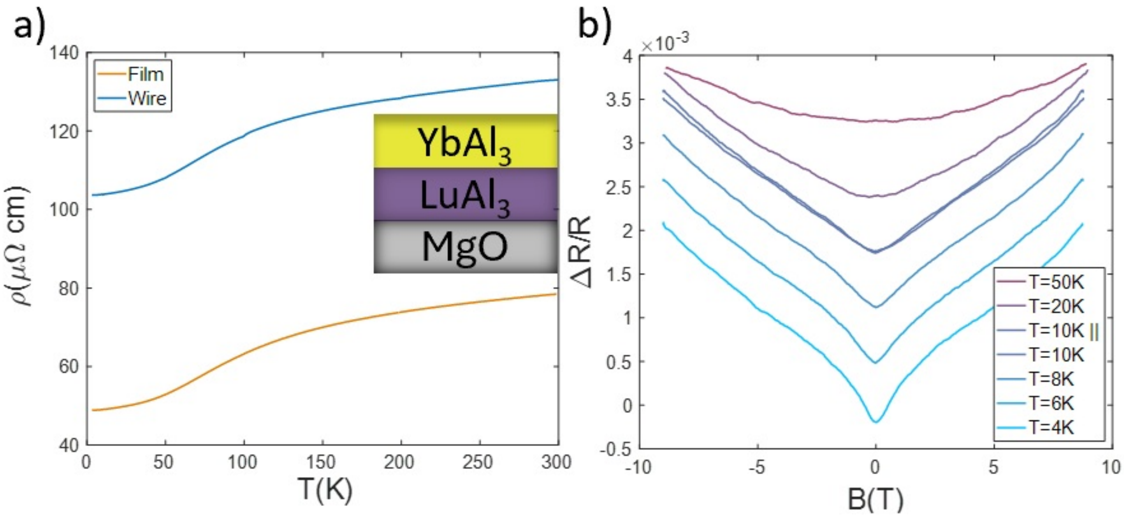

Figure 6.3 : a) Resistivity of unpatterned film and a representative wire of $\mathrm{YbAl_3}$. b) Magnetoresistance data with field going into the plane of the film in all except at 10 K. Curves shifted for clarity
[83, Reproduced]

Initial MR measurements, shown in Fig. 6.3b, showcase a linear-in-B dependence at higher values of $B \perp$ c-axis. This is consistent with measurements done in bulk crystals[74,86] at low magnetic fields. A peak in the conduction can be observed and will be discussed more so in the next section. Interestingly the linearity in B begins to become quadratic as temperature is increased above T^* — observed in bulk samples[74,86] — indicating that it might be related to the mechanism of heavy fermion coherence.

6.3 Magnetoresistance Measurements and Analysis

Fitting the linear background in the MR measurements and removing the background, highlights the peak in conductance and fluctuations where the MR was linear as seen in Fig. 6.4a,b. As temperature is lowered, the peak in conductance grows and the fluctuations retrace themselves and grow and sharpen. These features are consistent with WAL and UCF respectively, given the strong spin-orbit observed in $YbAl_3$ due to Yb. Data shown in Fig. 6.4 were taken in a dilution refrigerator insert of a Quantum Design Dynacool cryostat.

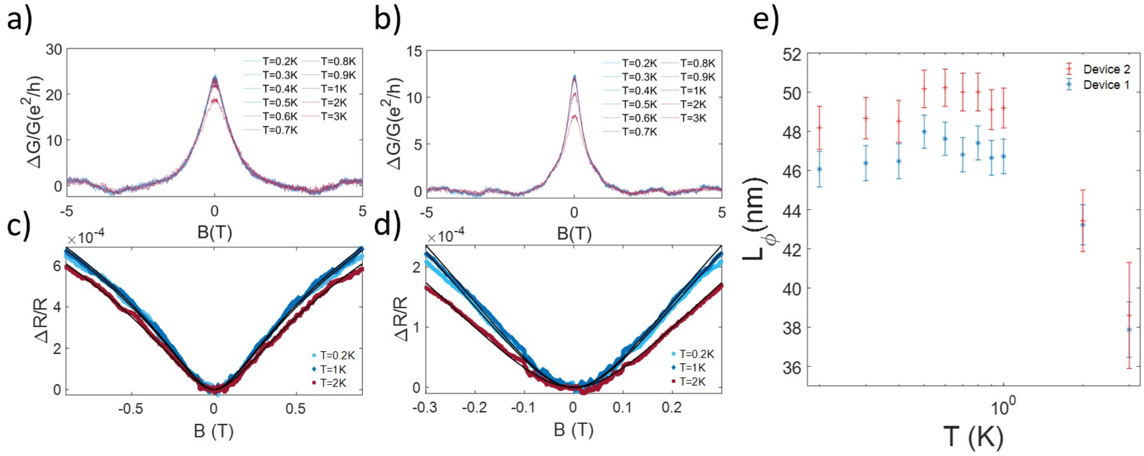

Figure 6.4 : a, b) MG data with the linear-in-B background subtracted for 154 nm and 168 nm wide devices respectively at various temperatures below 3 K. WAL is observed at low fields and UCF is observed at higher fields at representative temperatures, $T = 0.2, 1, 2$ K. c, d) MR data with fits from Eq. 6.2 superimposed. e) Coherence length as a function of temperature from fits from Eq. 6.2.

[83, Reproduced]

WAL Analysis

WAL can be analyzed in terms of theoretical expectations[87,88] using an expression appropriate to the dimensions of the nanowire, the 2D limit.

$$\left.\frac{R(B)-R(0)}{R(0)}\right|_{2D} = \frac{e^2}{2\pi^2\hbar}\frac{R(0)w}{L}\left[\psi\left(\frac{1}{2}+\frac{1}{2}\frac{\hbar}{2e|B|L_\phi^2}\right)-\ln\left(\frac{1}{2}\frac{\hbar}{2e|B|L_\phi^2}\right)\right] \tag{6.2}$$

This is Hikami, Larkin, Nagaoka prediction in the limit that the spin-orbit scattering time is the most rapid timescale in the process and hence drops out of the MR expression. The positive sign on the MR correction over the whole field range is consistent with the sign expected from the data in Fig. 6.4a,b, making it a reasonable ansatz for the system. It's not unrealistical to assume that the spin-orbit scattering time is rapid considering the strong spin-orbit coupling expected from the Yb $4f$ electrons role interaction with the conduction electrons in YbAl$_3$. A comparison between the inferred coherence length and the wire width and thickness allows a check for self-consistency of the assumption of quasi-2D quantum corrections to the conduction.

Fitting Eq. 6.2 to the data, shown in Fig. 6.4c,d, for the two wires of length 29μm and widths 154 nm and 168 nm in the field ranges of $+/-0.9$ T and $+/-0.3$ T respectively, to minimize the effects of UCf on the WAL signal. Fig. 6.4e shows the extracted $L_\phi(T)$ are less than w and greater than the film thickness t, so that analysis in terms of quasi-2D WAL is internally consistent. The saturation of $L_\phi(T)$ seen at low temperatures is not uncommon to observe and can be a result of spin-flip scattering from paramagnetic impurities[89,90]. While pure stoichiometric YbAl$_3$ should not contain such possible scattering centers, impurities or chemically distinct Yb containing species at surfaces and etched-boundaries could function as scattering sites. The coherence lengths exceed the inferred elastic mean free path, a requirement for the consistency of the usual derivation of the WAL correction.

UCF Analysis

In addition to quantifying L_ϕ via WAL, UCF can be seen at lower temperatures and can be used as another means of assessing coherence. The lowest temperature data, $T = 0.2$ K, is used as it represents the strongest signal of UCF. The WAL component between ±2 T is cut from the data the linear background from 14 T$>$ $|B|$ $>$2 T are removed to give a flat MR for UCF analysis. The auto correlation $F(\Delta B) = \delta G(B)\delta G(B + \Delta B)$ is taken to determine a critical field B_c such that $F(B_c) = 1/2F(0)$[91]. L_ϕ can then be found from B_c[91] using Eq. 6.3 and Eq. 6.4, with D_w being determined in Section 6.2. The appropriate equation is dependent on how L_ϕ compares to the thermal length scale, $L_T = \sqrt{\hbar D_w/k_B T} \sim 29$ nm. When L_T and L_ϕ are comparable, then L_ϕ exists in the crossover and Eq. 6.3 and Eq. 6.4 now serve as bounds for L_ϕ via UCF. This is indeed the case as Eq. 6.3 gives $L_\phi \sim 37$ nm and Eq. 6.4 gives $L_\phi \sim 103$ nm compared to the coherence length calculated from the WAL, $L_\phi \approx 47$ nm.

$$L_\phi = \sqrt{0.49\frac{h}{e}\frac{1}{B_c}} \qquad L_T \ll L_\phi \tag{6.3}$$

$$L_\phi = 1.14\frac{h}{e}\sqrt{\frac{k_B T}{\hbar D_w}\frac{1}{B_c}} \qquad L_T \gg L_\phi \tag{6.4}$$

The WAL and UCF data are consistent with well-defined Fermi liquid quasiparticles in this mixed valence heavy fermion system at temperatures well below the nominal onset of coherence, $T^* \sim 37$ K. As expected for a Fermi liquid in the comparatively weakly disordered regime ($k_F\ell \gg 1$), it is reasonable to consider the semiclassical picture of heavy charge carriers as diffusing through the material, but with quantum interference corrections as the complex phase of such a wavepacket remains well defined over distances of tens of nm. The dominant decoherence mechanism (e.g., e-e scattering; e-ph scattering at higher temperatures; extrinsic like spin-flip interactions with paramagnetic defects) in such a heavy fermion system can in principle be inferred from careful study of these mesoscopic corrections as a function of temperature and sample geometry.

6.4 Johnson Noise Measurements & Analysis

In addition to quantum coherence corrections to conduction, the fabrication of $YbAl_3$ nanowires enables further measurements to quantify the inelastic scattering of the emergent heavy charge carriers. Noise measurements in nanowires as a function of bias current make it possible within a simple 1D thermal model to infer the energy loss rate from the conduction electrons to the phonons[34–36], as described in Section 4.1.1. This approach has been employed previously in examining e-ph energy loss in mesoscopic $YbRh_2Si_2$, $\Gamma \approx 9{\times}10^9$ K^{-3}m^{-2} wires[69] and gold nanowires[35,36], $\Gamma \approx 5{\times}10^9$ K^{-3}m^{-2}, at low temperatures.

The voltage noise as a function of bias, shown in Fig. 6.5, was examined in a $YbAl_3$ wire of width 265 nm using a low frequency cross-correlation technique setup described in Section 5.3. It is important to note that the Debeye temperature is measured to be 337 K[92] in bulk $YbAl_3$, thus the phonon population is largely frozen out in the low temperatures displayed in Fig. 6.5. The phonon, however, can still be excited via driven electrons making the, meaning the Γ calculations are in a valid regime. At each substrate temperature, the noise as a function of current can be modeled well using Eq. 4.4 — restated in Eq. 6.5—, with Γ as an the sole adjustable parameter. Surprisingly the Γ is observed to be very temperature-dependent, $\Gamma(T)$ as opposed to what is observed in Au and $YbRh_2Si_2$, where it is largely constant for the whole low temperature range.

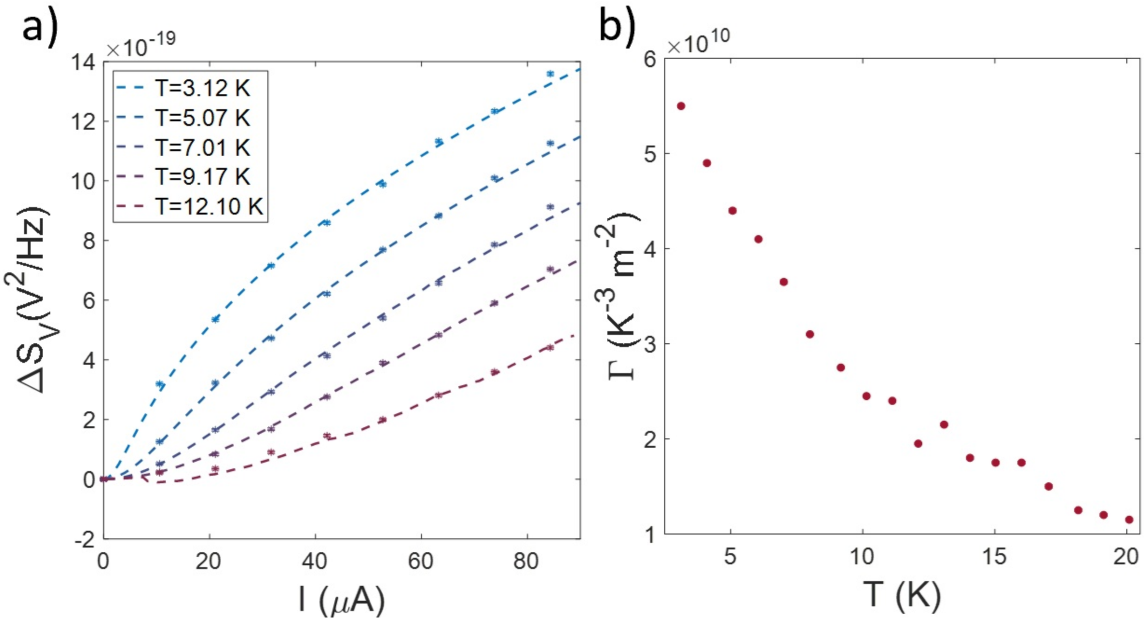

Figure 6.5 : a) Noise vs. bias current in a 265 nm wide wire with fits to Eq. 6.5. b) Calculated Γ vs substrate temperature T for same wire. Error is comparable to marker size.

[83, Reproduced]

$$\frac{\pi^2}{6}\frac{d^2T_e^2}{dx^2} = -\frac{eV}{Lk_B} + \Gamma(T_e^5 - T_{ph}^5) \tag{6.5}$$

The comparatively large Γ observed in $\mathrm{YbAl_3}$ is a signature of strong e-ph coupling. Studies of thermoelectric properties in $\mathrm{YbAl_3}$[73,77,93] have indicated that e-ph scattering with strong energy transfer is likely near room temperature, given that the phonon drag component of the Seebeck response exceeds the bare electronic contribution.At low temperatures, inelastic neutron scattering[78] indicates that an Al-based optical phonon mode can resonate with the Yb $4f$ level, causing dynamic changes in $4f$ hybridization. The strong temperature variation of $\Gamma(T)$ implies that significant e-ph interactions persist and evolve even at temperatures well below the coherence temperature for the heavy fermion quasiparticles. This temperature dependence of Γ occurs over the same range in which the thermal expansion coefficient of $\mathrm{YbAl_3}$ is observed to be negative and temperature dependent[79].

This coincidence suggests that a single underlying mechanism involving the evolving f-electron hybridization in the coherent heavy fermion Fermi liquid state drives changes to the lattice and the e-ph energy transfer processes. A strong connection between f-electron hybridization and lattice structure has long been known in Ce compounds in the context of the Kondo Volume Collapse[94, 95]. In that case, the free energy of the system depends strongly on the hybridization because of competition between the spin entropy of the local moments and the elastic energy cost of lattice deformation. In Yb mixed valence compounds, changes in $4f$ occupancy are strongly associated with corresponding changes in lattice volume, with the f^{13} limit having smaller volume and the f^{14} limit having larger volume[80]. Other mixed valence Kondo lattice systems similarly have negative thermal expansion coefficients associated with valency changes and affected by chemical disorder[96].

In an effort to explain these phenomena observed in $\mathrm{YbAl_3}$ collaborative effort is made with Ruiwen Xie of the Institute of Materials Science at the Technical University of Darmstadt. Theoretical models are used to explain both the electronic density of states — density functional theory combined with dynamical mean-field theory (DFT+DMFT)[97–99] — and the phonon bands — Quantum Espresso (QE)[100]. Using these tools and following the idea proposed by Abramovitch et al[101] to address e-ph coupling in correlated materials, two distortion phonon modes were used to carry out the DFT +DMFT calculations to model $\mathrm{YbAl_3}$ at $T = 17.5$, 20, 30, 50, 100, 200 K.

Temperature dependence of the DOS and the hybridization of the Yb $4f$ electrons with the conduction states can be seen in Fig. 6.6. Coherence features grow as temeprature is decreased, more so as T drop below 50 K, shown by the increasing peaks near E_F in Fig. 6.6a. Zooming into the region around E_F, Fig. 6.6b, it can be more the temperature dependence can be more clearly seen as well as a shift of the peak to larger than E_F at $T = 17.5$ K. In addition to the peak at E_F, there is a peak corresponding to the total angular momentum, due to strong spin-orbit coupling, of

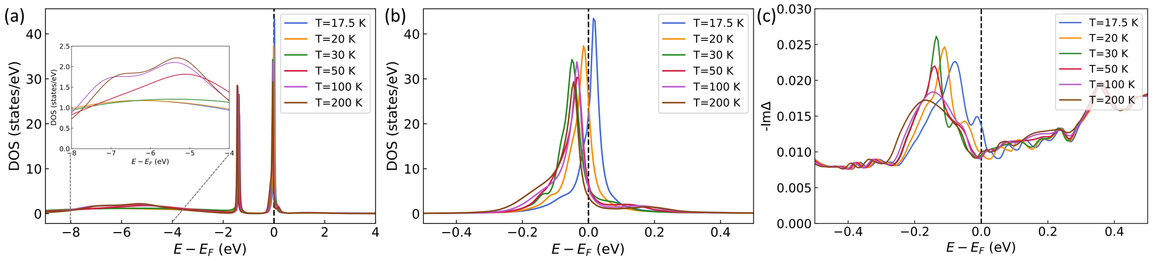

Figure 6.6 : a) Density of states (DOS) corresponding to Yb $4f$ states at different temperatures. The inset zooms in the DOS at the range of [-8, -4] eV. b) DOS of Yb $4f$ states close to the Fermi level E_F ([-0.5, 0.5] eV). c) Hybridization function of Yb $4f$ states at the energy range of [-0.5, 0.5] eV.
[83, Reproduced]

$J = 7/2$ that has been observed via angle-resolved photoemission spectroscopy[102]. Finally the hybridization function, Fig. 6.6c, is show to follow a similar trend as the DOS. This results in an increased hybridization between the $4f$ electrons and the become more strongly hybridized as temperatures drops below $T = 30$ K, indicative of continued evolution of the quasiparticles below the $T^* = 37$ K.

Following the establishment that the theoretical models properly displaying observed behavior of YbAl$_3$ the e-ph coupling strength can be investigated. To do so the self energy difference between the perturbed cell (Σ^{ph}) — atoms are displaced from equilibrium corresponding to phonon modes — and the unperturbed cell (Σ^{cn}) — atoms are at equilibrium, or the phonons are "frozen" — at $T = 20$ and 200 K for two phonon modes G and R. Fig. 6.7a show the representative modes taken from the full phonon band structure. The two modes were taken to be representative of contributions associated with the higher frequency regions, Al, and the contributions associated with low frequency regions, Yb. Figs. 6.7b and 6.7c showcase the temperature and energy dependencies of the G and R modes. The imaginary part of $\Sigma^{ph} - \sigma^{cn}$, the introduced change due to the lattice distortion is more substantial at low temperatures, especially for mode G. These changes and the growth in $g(E_F)$ are consistent with an increasing e-ph scattering parameter Γ with decreasing T.

These calculations also allow an investigation into the origin of the linear MR seen

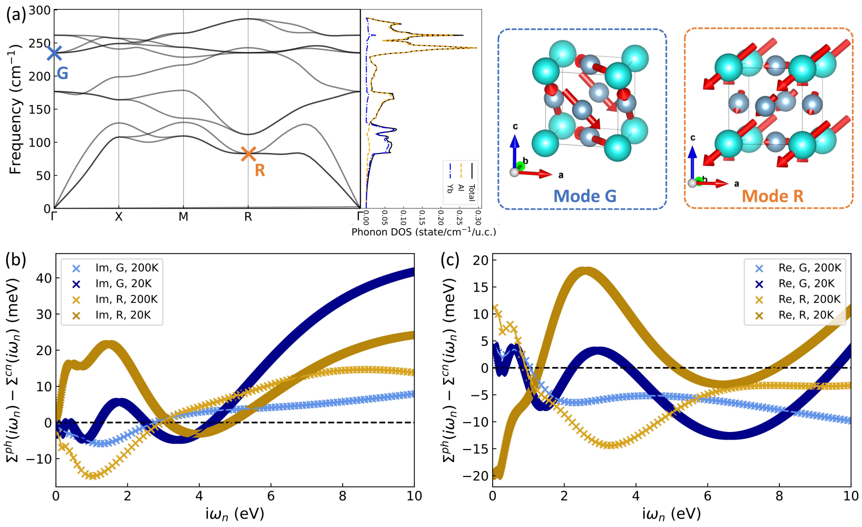

Figure 6.7 : a) Phonon band structure and phonon DOS of $YbAl_3$ with resolved contributions from Al and Yb. The frequencies corresponding to the distortion modes G and R are marked on the phonon band structure, with the atomic displacements illustrated on the right panel. The imaginary b) and real parts c) of self-energy difference ($\Sigma^{ph} - \Sigma^{cn}$) corresponding to $J = 7/2$ between the perturbed cell (Σ^{ph}) and the unperturbed cell (Σ^{cn}) at $T = 20$ and 200 K for modes G and R.
[83, Reproduced]

in both bulk and mesoscopic measurements mentioned at the end of Section 6.2. In the cubic enviroment of $YbAl_3$, $J = 7/2$ splits into three crystal field levels, Γ_6, Γ_7, Γ_8, due to the induced electric fields caused by the proximity of ions in a crystalline lattice. Based on DFT+DMFT model results, the energy difference between the the doublet ground state, Γ_6, and the first excited quartet state, Γ_8, is about 3 meV. 3 meV corresponds to a temperature, $T = E/k_b$, of $T = 34.8$ K which is close to T^*, suggesting that the onset of coherent heavy quasiparticles coincides with the reduction to an effective spin-1/2 manifold appropriate for the Kondo lattice picture of heavy fermions. This is also suggestive of a mechanism for the onset of the roughly linear-in-B MR background in Fig. 6.3. While very challenging to model directly, Zeeman splitting of the ground state doublet (linear in B-field) could then lead to a corresponding reduction in hybridization, suppression of $g(E_F)$, and a corresponding increase in residual resistivity at fixed disorder, an idea that could be tested with future calculations. Additionally, the energy difference between the second excited doublet Γ_7 and the ground state Γ_6 is approximately 25 meV, which is quite close to optical phonon frequency where Al has the prominent contribution to the phonon DOS. This proximity in energy scale could also lead to stronger interplay of the crystal electric field and the phonons, as proposed in the work of Čermák et al[103].

6.5 Conclusion

In summary, these mesoscopic transport and noise studies provide insights into the electronic excitations of this mixed valence compound. The observations of WAL and UCF at temperatures well below the coherence temperature $T^* \sim 37$ K are direct evidence for the existence of coherent heavy fermions. These mesoscopic phenomena give quantitative access to the phase coherence of the emergent quasiparticles. Both WAL and UCF analyses find L_ϕ of tens of nanometers. The very weak temperature dependence of L_ϕ implies that while the quasiparticles are coherent ($L_\phi \gg l$), inelastic processes strongly affect that coherence in these nanostructures, whether from extrinsic sources (e.g., paramagnetic impurities and defects) or from intrinsic sources (still evolving effective e-e scattering).

The Johnson-Nyquist noise measurements reveal an unusually strong and temperature-dependent e-ph energy loss in $YbAl_3$, with the energy loss parameter Γ increasing significantly as temperature decreases from 20 K to 3 K. This temperature dependence is coincident with the negative and T-dependent thermal expansion coefficient previously reported in bulk crystals, suggesting a common underlying mechanism likely related to the continued evolution of f-electron hybridization with conduction electrons below T^*. The magnitude of Γ in $YbAl_3$ considerably exceeds that of Au and even other heavy fermion compounds like $YbRh_2Si_2$ by an order of magnitude, consistent with the exceptionally strong e-ph interactions theoretically predicted and inferred in other measurements. Theoretical modeling points shows the increase hybridization expected basd on the measured $\Gamma(T)$ and offers a brief possible explanation of the origin of linear-in-B MR observed in $\mathrm{YbAl_3}$.

These results demonstrate that mesoscopic transport techniques, traditionally applied to weakly correlated materials, can serve as powerful probes of complex electronic systems. By extending these approaches to strongly correlated materials like $\mathrm{YbAl_3}$, we gain valuable insights into the nature of heavy fermion quasiparticles and their interactions with the lattice. Future work applying these techniques to other correlated electron systems may provide further understanding of the interplay between electronic correlations, coherence, and e-ph coupling in complex quantum materials.

Observations of Quasiparticle Loss in $YbRh_2Si_2$

$YbRh_2Si_2$ (YRS) is a tetragonal heavy fermion metal[104] that has emerged as one of the most important and well-studied quantum materials in condensed matter physics. YRS has been found to be an ideal model system for the study of the Kondo effect and quantum criticality[105]. YRS exhibits complex magnetic behavior, ordering antiferromagnetically at the Neel temperature $T_N = 70$ mK[106] and an unconventional QCP resulting in Kondo destruction[20,104] at $B_c \approx 60$ mT[106]($B \perp c$-axis).

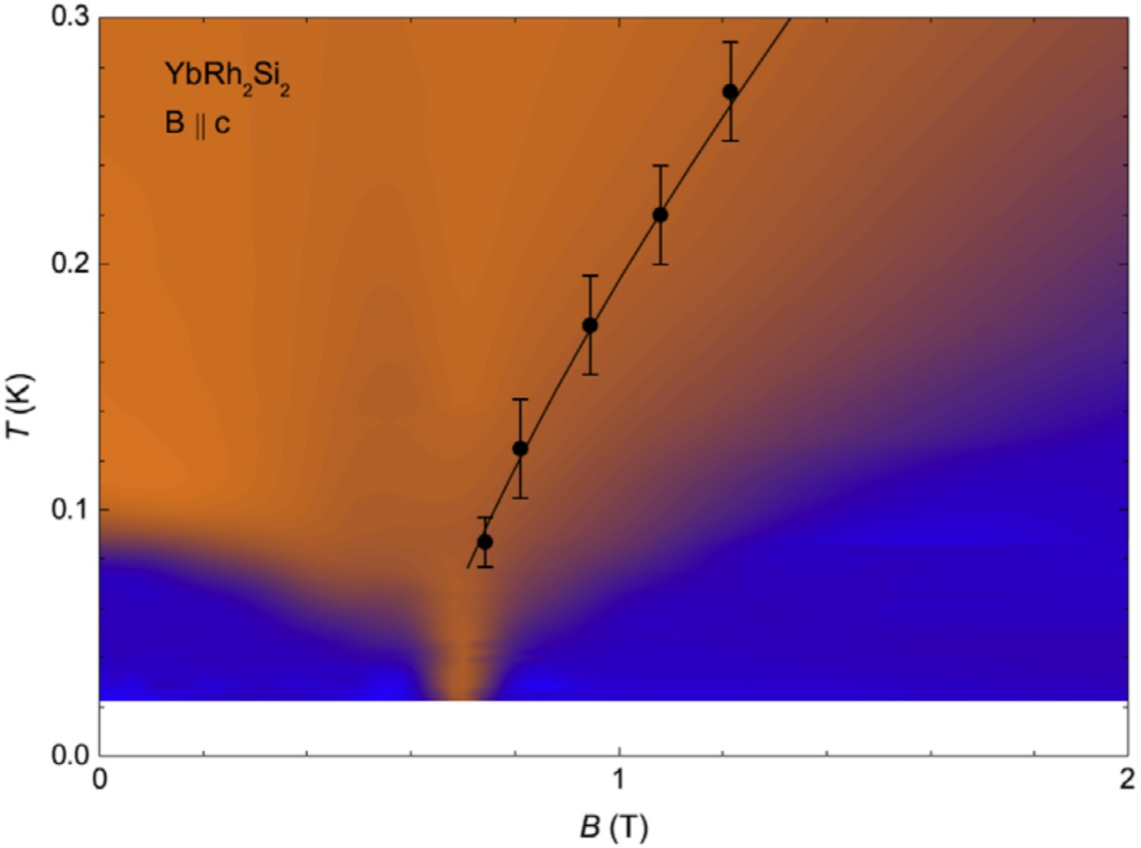

Figure 7.1 : Phase diagram showcasing emergence of strange metallicity from a QCP @ $B \approx 0.7$ T when $B \parallel c$-axis. The line in the line diagram indicates the transition temperature $T^*(B)$ at $B \perp c$-axis

[104, Adapted]

YRS easily accessible QCP[107] and it being a well-defined example of a strange metal make it the ideal material for the study of strange metallicity[108,109]. The QCP in YRS splits at zero T the low temperature states of the antiferromagnetic heavy Fermi Liquid metal to a paramagentic heavy Fermi Liquid. Hall effect measurements display an isothermal crossover at this transition that is rapid, indicative of a sudden reconstruction of the Fermi surface across the quantum phase transition at the QCP[110]. The strange metallicity fans out from the QCP as shown in Fig. 7.1 in temperature and magnetic field[109,111].

In the same vein as the $\mathrm{YbAl_3}$ case, the advent of thin films allows mesoscopic probing of the strange metal state and draw connections to theoretical models, summarized in Section 3.2. Previous measurements from the Natelson Lab have showcased this capability. Shot noise measurements in YRS have have suggested a lack of quasiparticles and made a connection to theory[69]. To further solidify this no or short-lived quasiparticle picture it's useful to replicate the MR measurements done in $\mathrm{YbAl_3}$ at low temperatures, like those shown in Fig. 7.1. These measurements show the quasiparticles in the adjacent heavy Fermi Liquid regimes and then the corresponding loss of them in the regions within the quantum critical fan, or the strange metal regime.

7.1 Previous Results: Shot Noise Measurements

It's useful to discuss the shot noise measurements[69] to offer a clear background and motivation for the current measurements. The fabrication and growth of the films is also mirrored in current measurements so will be covered in this section. To begin with, its helpful to discuss why shot noise measurements are helpful in researching strange metallicity.

Shot noise as mentioned in Section 4.3 looks at the transport of "granular" charge carriers of charge q with an average current $\langle I\rangle$. This can be done in complicated systems with quasiparticles to find the effective charge of the quasiparticle, such as fractional charge in a fractional quantum Hall liquid[112,113], fractional charge in quantum dot Kondo systems[114,115], and double charge due to electron pairing in superconductors[70,116].It can then follow that a lack of granular quasiparticles would naïvely result in suppression in the shot noise, due to the flow of a continuous fluid lacking fluctuations. Measuring shot noise in the strange metal YRS and comparing it to a known well-defined Fermi Liquid, Au, allows for an examination of how current flow differs between the the states and showcases suppression when compared to Fermi Liquid control case.

7.1.1 Device Fabrication

High-quality YRS films were grown on Ge substrates[117,118] via MBE. Nanowires were fabricated from the films into 660 nm long and 240 nm wide wires on a 60 nm film via EBL, shown in Fig. 7.2. Pads are defined first with thick Au pads (200 nm) with Cr protective mask put on top. Wires are then defined with pure Cr mask protective layer. The device is then etched via RIE and the leftover Cr is then removed via a 70° soak in 37% HCl solution leaving behind the Au pads and YRS wire. Devices were confirmed to maintain strange metallicity below ~ 10 K.

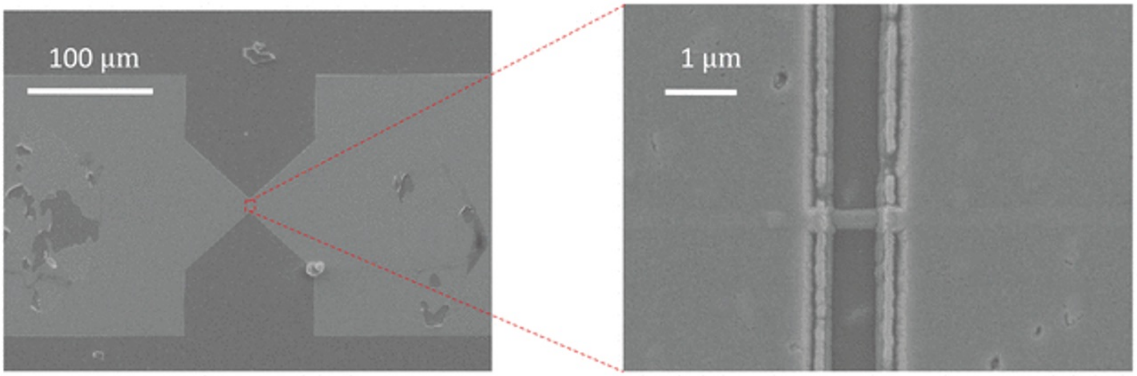

Figure 7.2 : $YbRh_2Si_2$ nanowire and pads defined for shot noise measurements with an additional image to view the wire quality at increased magnification.
[69, Adapted]

7.1.2 Shot Noise Results

The study of shot noise in YRS takes a comparative approach to analyzing the noise signals backed up by theoretical explanations of results seen in YRS. Study begins by setting up a control measurement of a well known and ideal Fermi liquid, Au. Shot noise measurements are performed in Au and are shown to conform well to the Fano factor $F = 1/3$ expected of the wire dimensions, Fig. 7.3b. In this Fermi liquid picture it's important to note that the only suppression allowed is that due to strong e-ph coupling.

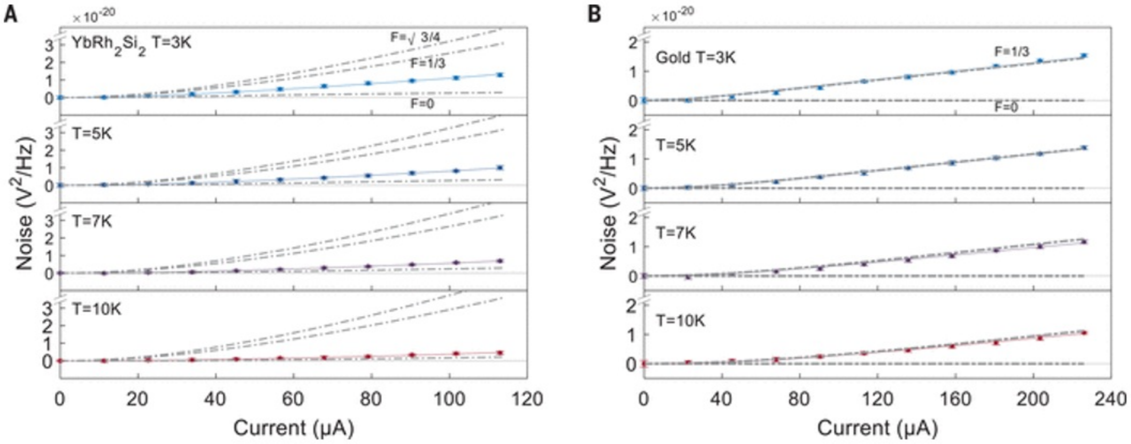

Figure 7.3 : Noise vs. bias current for a a) $YbRh_2Si_2$ and b) Au wire at 4 temperatures $T = 10, 7, 5, 3$ K. YRS data is shown to be suppressed below the expected F while Au conforms well to a $F = 1/3$
[69, Reproduced]

The noise measurements in YRS are done up to $\sim 110\ \mu$A with the flatband frequency signal taken from the range 300 - 600 kHz. Attempting to fit the noise data as a function of bias current to the shot noise model shows that F is suppressed well below the expected values. To rule out suppression via strong e-ph coupling, JN noise measurements are done to find an effective Γ for YRS in longer $\sim 30\ \mu$m wires. The Γ determined from this is $\Gamma \approx 9e9$ $\mathrm{K^{-3}m^{-2}}$ which is comparable to the Au value of $\Gamma \approx 5e9$ $\mathrm{K^{-3}m^{-2}}$, implying that the e-ph coupling is not causing the suppression.

The suppression seen in the YRS wires is therefore caused by a breakdown of the

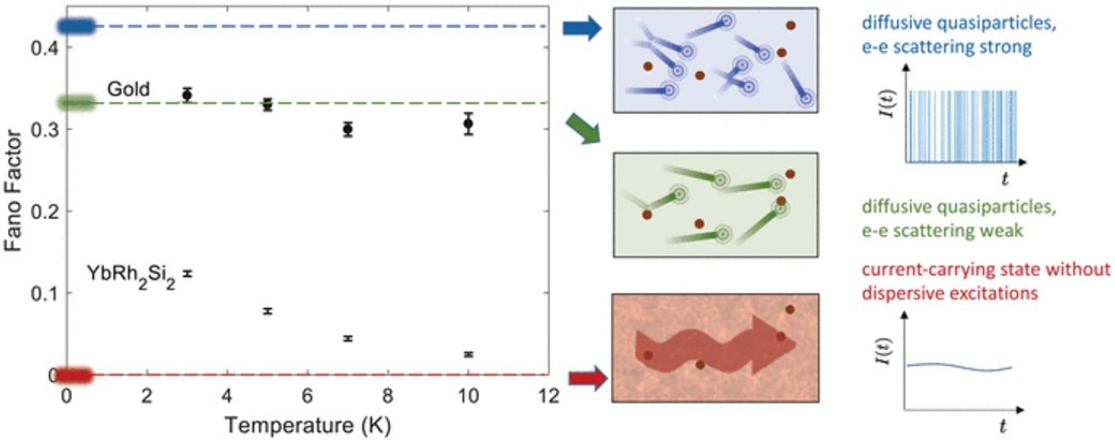

Figure 7.4 : Fano factors of YRS wire and Au wire as a function of temperature. Side panels offer a visual representation of quasiparticle interaction in relation to specific values of the $F = 0,\ 1/3,\ \sqrt{3}/4$.

[69, Reproduced]

Fermi liquid picture. That is that the idea of granular quasiparticles is no longer a valid picture hence the suppression of the Fano factor observed in YRS. This idea is supported by several theoretical papers as a result of these measurements that serve to theoretically replicate the data taken[119, 120]

7.2 Current Results

The MR measurements of YRS are an endeavor to probe the heavy Fermi liquid regimes that exist at low temperatures. Making use of a dilution refrigerator (DR) allows access to the low field antiferromagnetic heavy fermion state and the high field paramagnetic heavy fermion state separated by the strange metal fan permeating from the QCP shown in Fig. 7.1. With use of a DR it's possible to observe WAL in the low field antiferromagnetic state and then UCF oscillations in the paramagnetic state. Both effects should noticeably disappear given the results from shot noise experiments that there is a lack of quasiparticles, or extremely short-lived quasiparticles due to the sudden change in the coherence length that both WAL and UCF are dependent on.

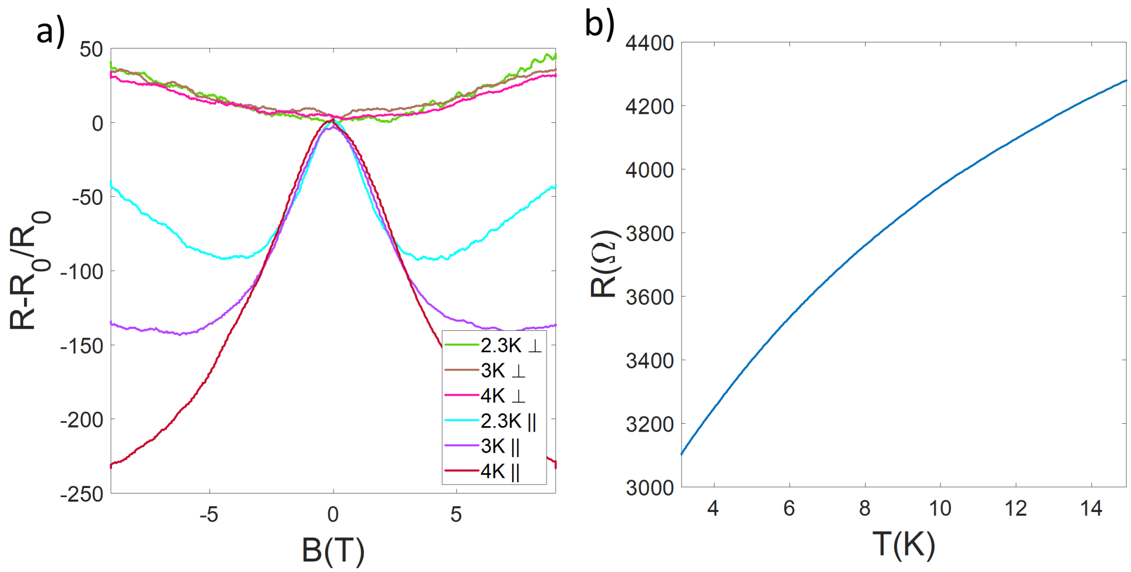

Figure 7.5 : a) MR measurements up to 4 K for $B \parallel c$ and $B \perp c$. b) $R(T)$ down to 3 K.

Initial tests have been done on films down to 2.4 K mainly to confirm similar quality of devices to that of the ones from the shot noise paper[69]. These measurements, shown in Fig. 7.5, show magnetoresistive effects and linear $R(T)$ behavior similar to those seen in previous devices. Notably the MR in parallel field has an interesting shape of which the origin is not known and the perpendicular field is quite simple in comparison. For detection of WAL and UCF further measurements at lower temperatures will be needed with a focus on perpendicular field due to strong anisotropy of these effects.

Recent measurements have been attempted at sub kelvin temperatures have been attempted using Prof. Yonglong Xie's DR. While the goal is to reach sub 100 mK temperatures, thermalization due to high frequency pickup only allows access to temperatures as low as $\approx$ 300 mK as can be seen in Fig. 7.6a. MR data with $B \parallel c$ was taken at the minimum temperature and at 1 K, shown in Fig. 7.6b. Interestingly a feature begins to appear at $T \approx$ 300 mK where one wouldn't expect considering its comparatively far away from the expected transition seen in Fig. 7.1. Theses measurements are still ongoing so there is little to be said aside from the noticeable deviation from the 1 K data. Which seems to imply that there might be some cuspy behavior developing at $\approx$ 300 mK. This is potentially indicative of WAL though it is still to early to make any strong claims of this.

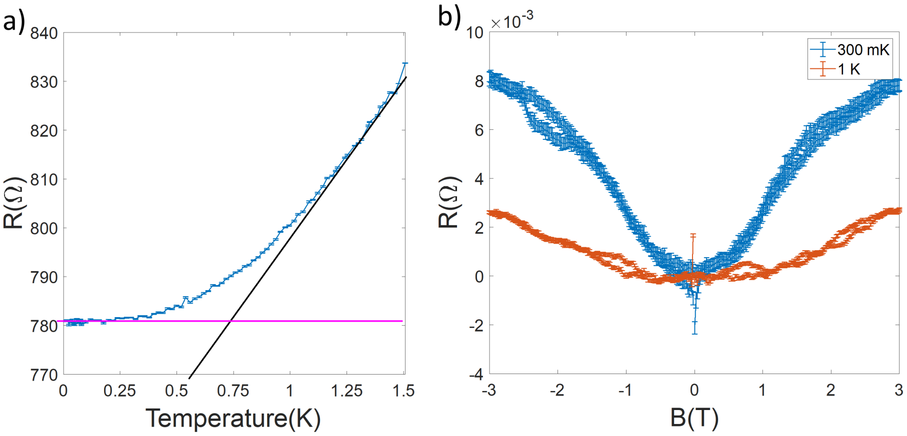

Figure 7.6 : a) $R(T)$ data showing flattening at $T \approx 300$ mK due to thermalization. Guiding lines help indicate linearity from strange metal (black) and flat region from thermalization (pink). b) MR data at the effective 300 mK and 1 K.

Following these initial measurements at Rice, devices will be sent to the Paschen lab — the providers of the films — for use of their DR that can access sub 100 mK temperatures. At these temperatures the low field phase should be accessible and the the $B = 0$ T $R(T)$ data should show a sudden change in behavior from T-linear to T-quadratic. At these temperatures it can be expected that WAL would appear in this regimes and that as soon as the field approaches $\sim$ 700 mT a jump should be observed and indicate the transition into the strange metal state[121].

In addition to the devices being sent to the Paschen Lab doing MR measurements shorter devices will be added into the batch of devices sent over. These shorter devices will be for shot noise measurements at sub 100 mK temperatures allowing the tuning of YRS in and out of the Fermi liquid regime for a more direct comparison than what was seen in the previous shot noise results.

7.3 Conclusion

Strange metallicity is still not well understood phenomena and is the subject of many studies with YRS being a leading candidate for study, particularly in the case of thin film studies. With recent access to thin films, thanks to growth by the Paschen lab at the Vienna University of Technology, mesoscopic scale devices are now able to be fabricated as new probes into the origins of strange metallicity. Shot noise measurements have already proved successful in gaining insight in the YRS films and an extension of those measurements via MR measurements seeks to further support those measurements and offer some new quantitative differences in the transition between Fermi Liquid and strange metal states.

Initial MR measurements have been done at Rice down to 0.3 K and further measurements are planned to be done to lower temperatures. These measurements will seek to probe the coherence length of the carriers in YRS and there evolution across the strange metal state. Plans have already been made to expand upon these and the previous shot noise measurements by sending films to the Paschen lab for sub 100 mK analysis.

Mesoscopic probes of the strange metal and heavy fermion states offer a unique look into the interesting states resultant of strong electron correlations. As more strongly correlated films become available these studies of the interplay of heavy fermion behavior and strange metallicity will help to shape the understanding of the quantum nature resultant of strong electron correlations.

Misfortunes of $Sr_3Ru_2O_7$ Nanowires

$Sr_3Ru_2O_7$ (SRO327) is perovskite of the Ruddlesden-Popper (RP) series of oxide phases ($A_{n+1}B_nO_{3n+1}$)[122]. SRO327 experiences a strange metal state emanating from a QCP at $B_c \approx 7.8$ T. This makes SRO327 one of the best candidates to study strange metallicity due to the ease of accessibility of both the Fermi liquid state at low fields and the strange metal state at high fields, with both being easily accessible at a large range of temperatures. Studying such a well-defined system offers the advantage of confirming the strange metal data seen in the YRS system of the previous chapter for universality of results.

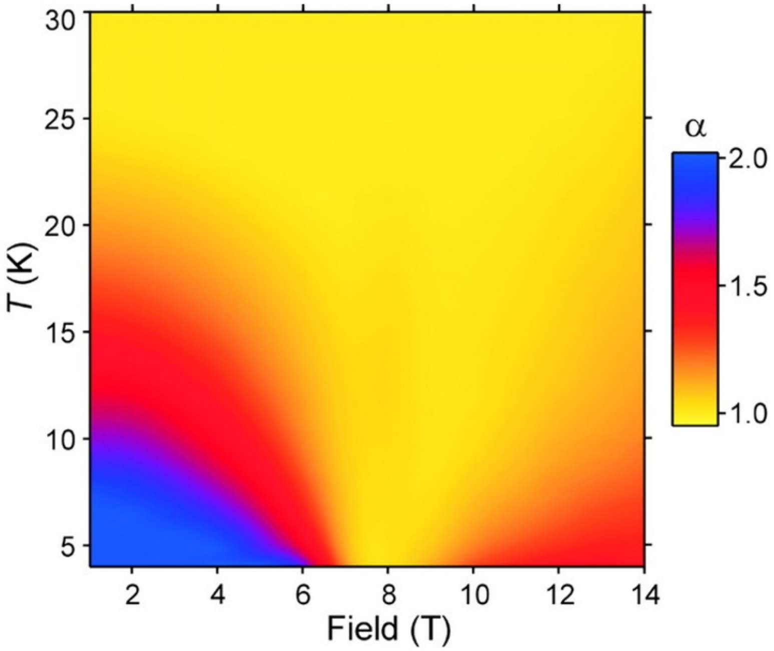

Figure 8.1 : Phase diagram of the exponent α in the equation $\rho = \rho_0 + AT^{\alpha}$ showcasing emergence of strange metallicity from a QCP @ $B \approx 7.8$ T when $B \parallel c$-axis [26, Reproduced]

Much work has been done to characterize strange metallicity bulk SRO327 crystals: defining the range of strange metallicity[26], study spin fluctuations across the strange metal boundary[123], ARPES measurements detailing the Fermi surface[124].

However, there have yet to be much work into thin films mainly due to the sheer difficulty of growing high quality SRO327 thin films. Various attempts have been made in growth in recent years[125–127], but as of the time of this research it has been difficult to grow pure SRO327 films.

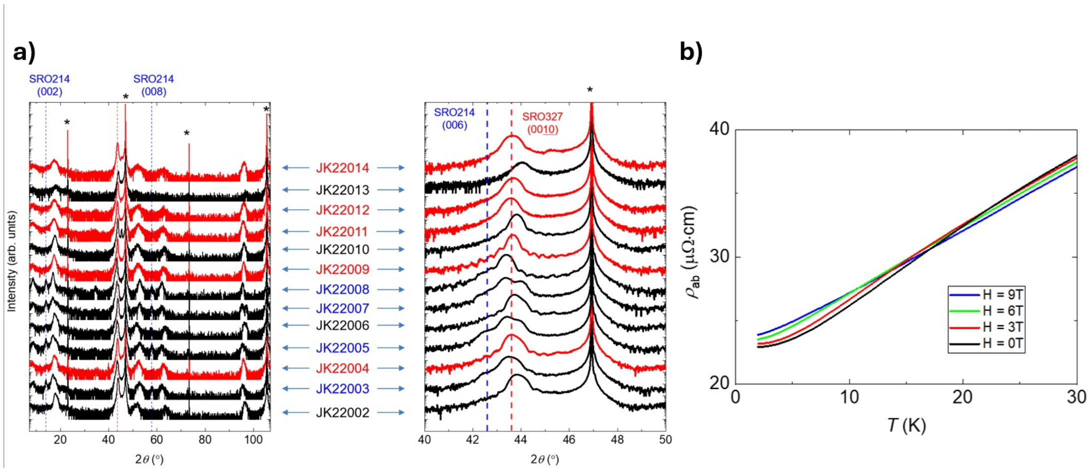

Figure 8.2 : a) X-ray diffraction data of SR)327 samples showcasing peaks corresponding to SRO327, red dashed lines, SRO214, blue dashed lines, and the substrate LSAT, black dashed lines. Data is of several samples offset from one another for clarity and colored such that red curves are the highest quality, blue is mixed with SRO214, and black curves which are of low quality mixed with SRO4310. b) Temperature dependent resistivity data at 4 different magnetic fields parallel to the *c*-axis, $B = 0, 3, 6, 9$ T, showcasing the evolution from Fermi liquid T^2-behavior to the strange metal T-behavior in the representative high quality film JK22012
[128, adapted]

Collaborative efforts with Tae Won Noh's group at Seoul National University[127] gave access to test films of the highest quality Noh's group could achieve at the time via pulsed laser deposition. The films show little SRO214 mixing, a more stable competing phase of the RP series, though due to narrow growth region of a $\sim$ 50 °C[128] makes this difficult to actually achieve. The films grown were seen to be very sensitive to chemical agitation resulting in destruction of the strange metal behavior, either a shift into the SRO214 phase or by some other mechanism. This introduces the challenge of how to fabricate such a sensitive material and if able to fabricate the process can serve as a base line for how to fabricate other potentially unstable materials for mesoscopic analysis.

8.1 Standard Fabrication: EBL

Initial tests of fabricating the SRO327 films consisted of using the standard procedure described in Section 5.1.1. Of important note is the use of the 100kV electron beam of the Elionix system. The 100kV beam ripped up the exposed surface of the SRO327 as seen in Fig. 8.3. This is obviously renders any pattering of SRO327 via 100kV e-beam useless. This observation sparks the need to develop a new process to fabricate the SRO327 films.

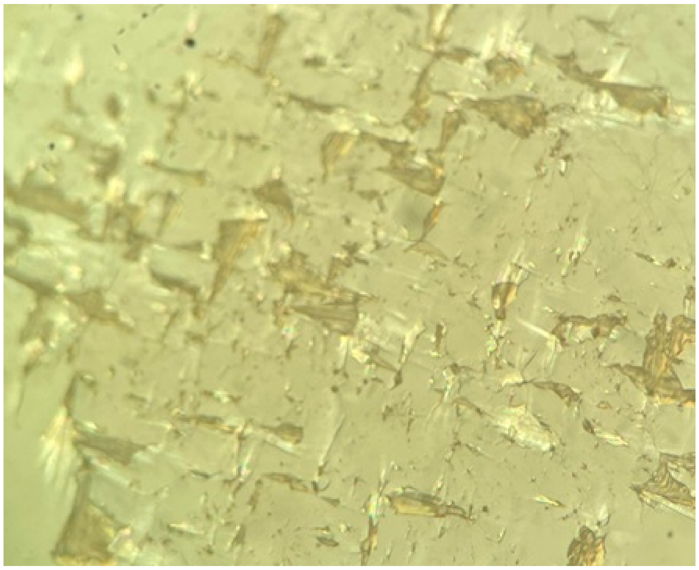

Figure 8.3 : Image of the SRO327 surface after exposure to a 100kV e-beam from the Elionix system.

The first, and in theory simplest, idea is to simply use a lower column voltage. Considering the damage 100kV caused to the surface of SRO327 it would be best to use the lowest column voltage possible to define the patterns. Going to lower voltages opens up the issue of reduced resolution due to scattering of the electron upon impact with the resist, Fig. 8.4. To that end the lowest beam voltage, through testing, that can be reasonably achieve the maximum device size of $\sim$ 300 nm x 30 μm is 10kV.

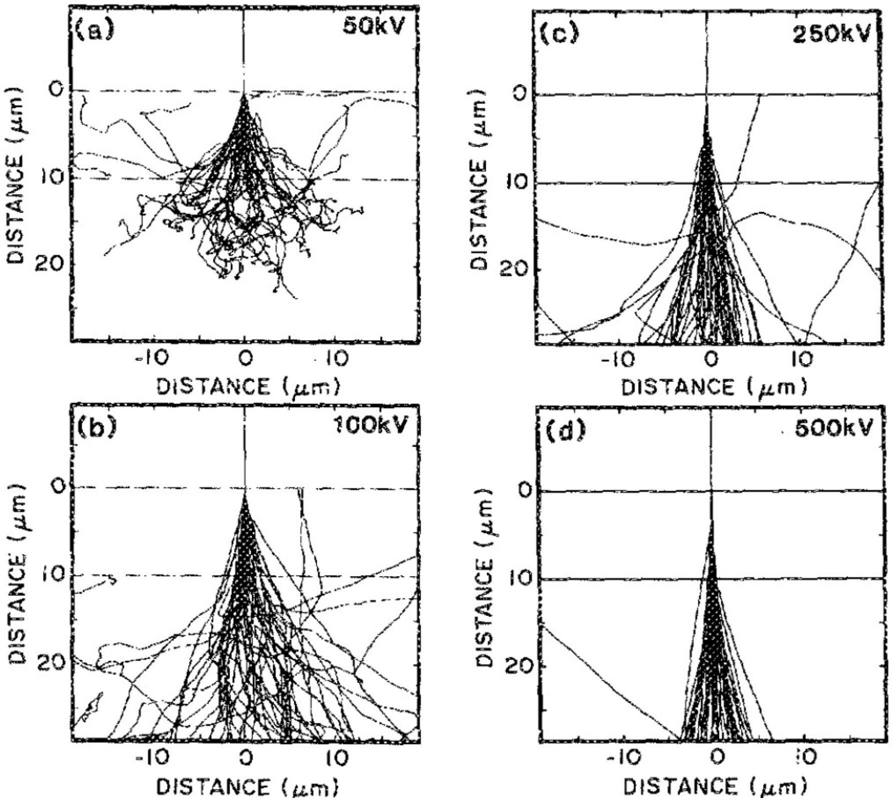

Figure 8.4 : Plots of scattering calculations at several column voltages for EBL. Of note is the decreased scattering as voltage is increased resulting in a increase in resolution.

[129, Reproduced]

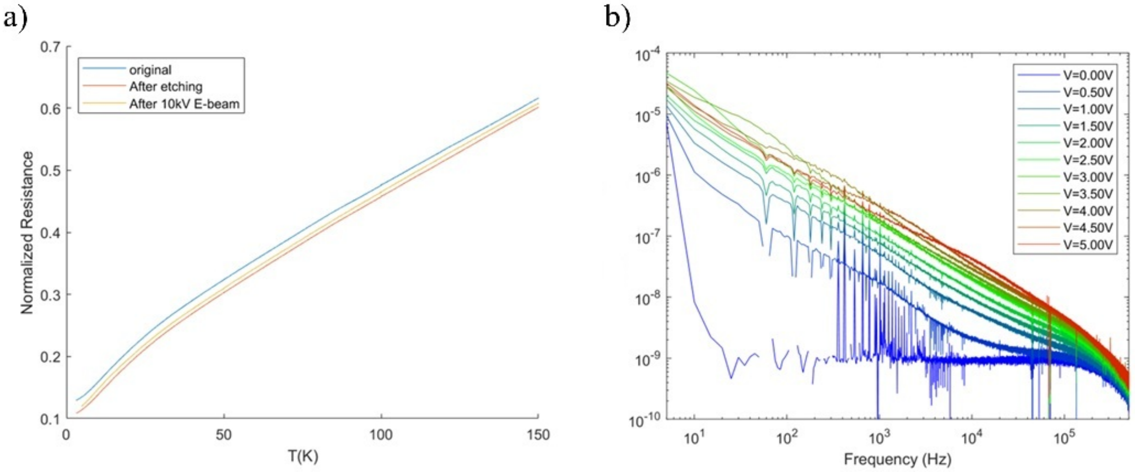

Figure 8.5 : a) Normalized R vs. T for the unpatterned film, film after 10kV exposure(and deposition of pads), and the nanowire fabricated via etching at 8 T, $B \parallel c$-axis . b) Raw noise data of the final fabricated nanowire showing a large $1/f$ presence across the whole noise spectra.

At 10kV the SRO327 looks visibly undisturbed. With the first step of not visibly damaging the surface achieved the next step is to make sure the strange metal phase present at $B \approx 7.8$ T is still present. For a more systematic study to ensure that both the exposure and the etching, Ar ions in the RIE with similar parameters to the previous materials' studies, aren't changing the properties measurement of $R(T)$ was done after exposure to the 10kV and after the etching the wire. Fig. 8.5a shows the results of these measurements compared to that of untouched film. Incredibly it shows that the 10kV beam seems to maintain the strange metal state given how the 100kV beam behaved. Unfortunately Fig. 8.5b shows a subsequent noise measurement wherein a large 1/f noise presence is seen, completely dwarfing all flat-band noise signals necessary for both shot noise and JN noise measurements. This $1/f$ noise could potentially be intrinsic, but is this is most likely not the case as will be seen later on.

8.2 Alternative Fabrication 1: Focused Ion Beam

Since the 10kV beam failed to produce viable wires a new approach needs ot be taken that offers similar resolutions and this can be found by use of a Focused Ion Beam (FIB). Focused Ion Beam is a process that bombards the service with a focused beam of ions. These ions break bonds and physically remove material in the spot size the beam encompasses. The particular FIB used for these tests is the FEI Helios NanoLab 660 DualBeam system which makes use of Ga^+ as the FIB source.

The FIB's precision etching can be used to combine the lithography and the etching into a single step. Notably the pads for the wire will still be lithographically defined using the 10kV e-beam with the hope that most of the $1/f$ signal resulted from the defined wire. The FIB will be used to outline the pads and then to define the wire between the pads as shown in Fig. 8.6a. An Atomic Force Microscopy (AFM) of a test pattern on SiO_2 is included in Fig. 8.6b to showcase how the pattern would

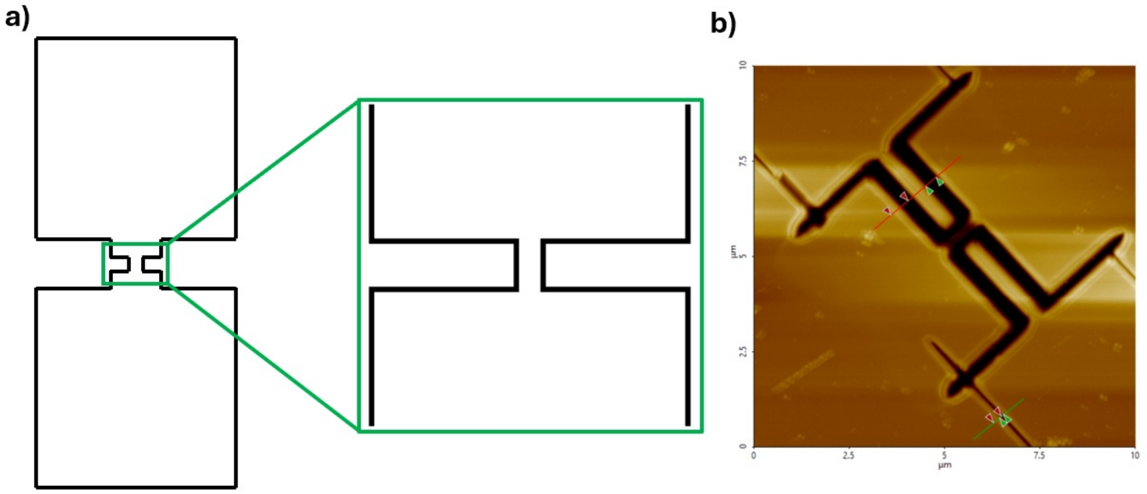

Figure 8.6 : a) Pattern design for a FIB outline of a SRO327 nanowire with a zoom in of the actual wire. Black lines indicate where material is removed via FIB. b) Atomic force microscopy (AFM) image of failed test example of FIB process on SiO_2.

ideally turn out.

To transfer the design to the SRO327 films some care needs to be taken due to needing to lightly expose the etch location to the FIB. To protect the film a ≈ 50 nm thick coating of SiO_x is deposited across the film. The protective SiO_x also hopefully serves to reduce the Ga^+ implantation issue commonly associated with FIB processes.

Unfortunately the actual process of FIB on the SRO327 films is plagued by the issue of a drifting beam. This beam drift resulted in the pattern seemingly being dragged across the surface creating shadows around where the actual pattern was taken. This results in ill-defined wires and potential contamination of the already sensitive SRO327 to the Ga contamination. This drift is due to charge being built up along the surface of the film deflecting the ions heading towards the target area. Many attempts were made to rectify this issue including adding in conductive tape, silver epoxy, and removal of the protective oxide layer to give the charge somewhere to dissipate to. Due to the mesoscopic scale these conduction spots can't be particulary near the wire itself and well fixing the issues around the pads the wire still deviated as it was done in a separate step for improved resolution meaning the at Ga^+-based

FIB failed to fabricate useful nanowires.

8.3 Alternative Fabrication 2: 3D Photolithography

With the failure of both FIB and EBL the next idea for lithographically defining wires is using PL. Early on in the testing of $1/f$ in the SRO327 nanowires seen in Fig. 8.5b some wider, ≈ 2 μm, wires were created as a sanity check to see if the etching method used to define the wires is the cause of the observed $1/f$ noise. Fig. 8.7a showcases the raw spectra in the PL defined wire and shows that these wires don't seem to show $1/f$ higher than ≈ 3 kHz, which is resultant from the amplifiers and therefore unavoidable. This result confirms the statement mentioned earlier that $1/f$ noise isn't intrinsic to the SRO327 films otherwise even at this scale there would be some bias dependent signature that showed itself. Now this doesn't rule out the etching as being the cause of the previously observed $1/f$ noise. To do that new wires will need to be defined by PL, a much gentler physical process compared to EBL, on similar widths as the EBL defined wires. As mentioned in Section 5.1.1 PL is usually ill-suited to defining nanowires due to the limitations of resolution that can be achieved on most research grade PL apparatuses.

There is a technique that does fit that criteria called 3D photolithography. 3D PL functions similarly to resin 3D printers wherein a resin is precisely targeted with photons to cause a chemical reaction to bind the polymers of the resin into a solid object. In the case of 3D PL a 2-photon method is used to only provide the necessary energy for the chemical reaction at the point where two laser pulses meet, giving improved resolution of that of regular PL. The specific device used for the 3D PL was a Nanoscribe Photonics Professional GT with resolutions of a few hundred nanometers.

Work flow followed the same idea as the FIB wherein the pads were defined via the 10kV e-beam method with the exception that the 3D pattern drawn by the 3D PL system will function as the mask for the wire and etching would follow the same

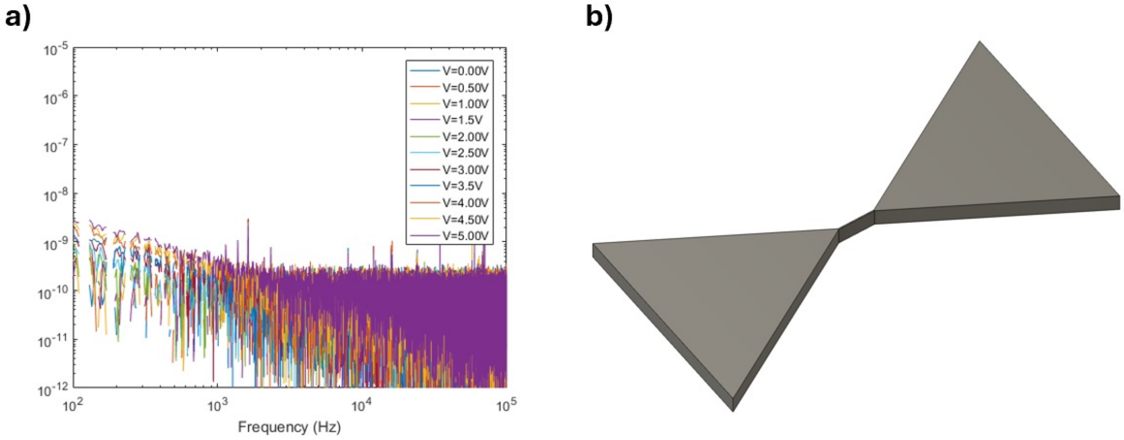

Figure 8.7 : a) Raw noise data of a 2 μm wide photolithographically defined wire. b) Image of the 3D design of the 100 nm x 10 μm nanowire with triangular anchors for stability all 1 μm.

procedure as in the 10kV case. Initial designs used were that solely of a 300 nm x 10 μm wire. This design encountered the issue that only the heavily overdosed wires, in a dose test, remained on the surface. This is most likely due to the cleaning procedure used to wash off the leftover resin after lithography and the fact that the surface area contact was potentially too narrow compared to the sway of the 1 μm, necessary to survive the etch. Adjustments were made to the design as a result and can be seen in Fig. 8.7b. This adjustments added triangular anchors to hopefully stabalize the ends and given more structure to the nanowire. This worked better, however, now resulted in the nanowires not washing off but stretching and becoming curved from the cleaning. Additional structures and shortening of the wire run the risk of changing the shape of the nanowire too much and misalignment do to the optical nature of the alignment respectively. This means that the third and final attempt at fabricating nanowires on SRO327 has resulted in a failure and the 3D PL method wasn't successful.

8.4 Conclusions and Insights

SRO327 is very chemically sensitive material and thin films of it are not very phase pure and easily damaged. This provides a great fabrication challenge in how to define a nanowire out of the film without altering any of the desired strange metal properties. To that end several methods were tried ranging from standard EBL, FIB, and 3D PL. All methods proved to be insufficient for different reasons at properly defining a stable wire.

The attempts documented here are limited by access to machines and techniques provided by Rice University by the Shared Equipment Authority. There are several possibilities to proceed forward on fabrication of SRO327 thin films. One such possibility is improved growth and stability of the SRO327 films might mean that the most successful method, the 10kV EBL, could potentially work assuming that the $1/f$ noise resultant from it would be mitigated if stability were improved. Another idea would be to test if instead of a Ga^+ FIB a He^+ FIB were used. This idea functions off of the idea that the He ions are smaller and therefore offer improved resolution and contamination and potentially less charge effects when trying to define the nanowire. The last idea, and most likely to succeed, would be the use of PL technique that offers finer resolution than the 3D PL but doesn't do negative lithography and instead does positive lithography. There are machines capable of this used in industry, such as Deep UV lithography (DUV)[130]. DUV is used in the semiconductor industry for wafer scale-sized fabrication with resolutions of tens of nanometers. The difficulty in this idea is that these machines are meant for wafer scale and therefore are not trivial to do on small $\sim$ 5 x 5 mm chips. Even if it were possible the cost of such machines for research use would be astronomical. Any of these ideas described have the potential to result in successful fabrication of SRO327 films, and by proxy sensitive films, for further universality research of an easily accessible strange metal state.

Conclusions

Mesoscopic transport measurements have proven to be powerful probes of strongly correlated electron systems, as demonstrated throughout this thesis by extending techniques traditionally applied to weakly correlated materials into the realm of quantum criticality and heavy fermion physics. Through systematic studies of fabricated nanostructures from epitaxial thin films, we have provided unique insights into quantum coherence, quasiparticle behavior, and electron-phonon interactions in exotic quantum states. The successful fabrication of functional devices from $\mathrm{YbAl_3}$ and $\mathrm{YbRh_2Si_2}$ establishes these approaches as essential tools for investigating electronic correlations at the nanoscale, while the challenges encountered with chemically sensitive $\mathrm{Sr_3Ru_2O_7}$ highlight the need for continued development of gentler fabrication techniques to access a wider range of strongly correlated materials.

The scientific contributions presented here address fundamental questions about the nature of electronic transport in strongly correlated systems. Magnetoresistance studies provided the first direct quantification of phase coherence lengths in heavy fermion quasiparticles, confirming coherent heavy fermions in $\mathrm{YbAl_3}$ with coherence lengths of tens of nanometers well below the coherence temperature. Johnson-Nyquist noise spectroscopy revealed anomalous temperature-dependent electron-phonon coupling that increases with decreasing temperature and connects with theory to explain further evolution at low temperatures. Measurements performed on $\mathrm{YbRh_2Si_2}$ serve to expand upon previous shot noise measurements by taking magnetoresistance and additional shot noise measurements to lower temperatures where both the heavy fermion and strange metal states can be accessed via field tuning. Attempts were made to perform similar measurements on $\mathrm{Sr_3Ru_2O_7}$, but due to fabrication complications, these efforts primarily provided information on the difficulties of fabricating devices from sensitive materials. Nevertheless, these results offer insight into possible avenues to pursue should further investigation be attempted.

These results contribute to our fundamental understanding of how electronic correlations manifest in transport properties and quantum coherence phenomena, validating theoretical frameworks for strongly correlated Fermi liquids while offering insight into the transport phenomena in strange metal regimes. The combination of magnetoresistance and noise measurements offers a comprehensive approach to characterizing electronic coherence and energy dissipation mechanisms that complements bulk measurements and theoretical predictions. The information that can be gleaned from these measurements aren't limited to just these materials, as further materials of interest are discussed in Appendix A. Ultimately, this work establishes mesoscopic transport as an indispensable tool for unraveling the microscopic origins of exotic electronic behavior, paving the way for future investigations into the rich physics of strongly correlated materials.

Bibliography

[1] Ohm G 1827 *T.H. Riemann*

[2] Drude P 1900 *Annalen der Physik* **306** 566–613 (*Preprint* `https://onlinelibrary.wiley.com/doi/pdf/10.1002/andp.19003060312`) URL `https://onlinelibrary.wiley.com/doi/abs/10.1002/andp.19003060312`

[3] Kittel C 2005 *Introduction to solid state physics / Charles Kittel.* eighth edition. ed (Hoboken, NJ: John Wiley) ISBN 047141526X

[4] Ashcroft N W and Mermin N D 1976 - 1976 *Solid state physics / Neil W. Ashcroft , N. David Mermin, Cornell University.* (New York: Holt, Rinehart and Winston) ISBN 0030839939

[5] Natelson D 2015 *Nanostructures and nanotechnology / Douglas Natelson, Rice University, Houston.* (Cambridge, United Kingdom: Cambridge University Press) ISBN 9780521877008

[6] Landauer R 1957 *IBM Journal of Research and Development* **1** 223–231

[7] Datta S 1995 *Electronic Transport in Mesoscopic Systems* Cambridge Studies in Semiconductor Physics and Microelectronic Engineering (Cambridge University Press)

[8] Ferry D and Goodnick S M 1997 *Transport in Nanostructures* Cambridge Studies in Semiconductor Physics and Microelectronic Engineering (Cambridge University Press)

[9] Andersen M P, Mikheev E, Rosen I T, Tai L, Zhang P, Wang K L, Kastner M A and Goldhaber-Gordon D 2023 *Nano Letters* **23** 10802–10810 pMID: 38029283 (*Preprint* `https://doi.org/10.1021/acs.nanolett.3c02932`) URL `https://doi.org/10.1021/acs.nanolett.3c02932`

[10] Andres K, Graebner J E and Ott H R 1975 *Phys. Rev. Lett.* **35**(26) 1779–1782 URL `https://link.aps.org/doi/10.1103/PhysRevLett.35.1779`

[11] Landau L 1956 *Sov. Phys. JETP* **3** 920–928

[12] Coleman P 2015 *Introduction to Many-Body Physics* (Cambridge University Press)

[13] Morosan E, Natelson D, Nevidomskyy A H and Si Q 2012 *Advanced Materials* **24** 4896–4923 URL `https://doi.org/10.1002/adma.201202018`

[14] Smidman M, Adroja D T, Goremychkin E A, Lees M R, Paul D M and Balakrishnan G 2015 *Phys. Rev. B* **91**(6) 064419 URL `https://link.aps.org/doi/10.1103/PhysRevB.91.064419`

[15] Kondo J 1964 *Progress of Theoretical Physics* **32** 37–49 ISSN 0033-068X (*Preprint* `https://academic.oup.com/ptp/article-pdf/32/1/37/5193092/32-1-37.pdf`) URL `https://doi.org/10.1143/PTP.32.37`

[16] Aynajian P, da Silva Neto E, Gyenis A, Baumbach R, Thompson J, Fisk Z, Bauer E and Yazdani A 2012 *Nature* **486** 201–206

[17] Sachdev S 1999 *Quantum Phase Transitions* (Cambridge University Press)

[18] Hartnoll S A, Lucas A and Sachdev S 2018 *Holographic Quantum Matter* (The MIT Press)

[19] Davison R A, Schalm K and Zaanen J 2014 *Phys. Rev. B* **89**(24) 245116 URL `https://link.aps.org/doi/10.1103/PhysRevB.89.245116`

[20] Coleman P, Pépin C, Si Q and Ramazashvili R 2001 *Journal of Physics: Condensed Matter* **13** R723 URL `https://dx.doi.org/10.1088/0953-8984/13/35/202`

[21] Tranquada J M, Lozano P M, Yao J, Gu G D and Li Q 2024 *Phys. Rev. B* **109**(18) 184510 URL `https://link.aps.org/doi/10.1103/PhysRevB.109.184510`

[22] Wahlberg E, Arpaia R, Seibold G, Rossi M, Fumagalli R, Trabaldo E, Brookes N B, Braicovich L, Caprara S, Gran U, Ghiringhelli G, Bauch T and Lombardi F 2021 *Science* **373** 1506–1510 (*Preprint* `https://www.science.org/doi/pdf/10.1126/science.abc8372`) URL `https://www.science.org/doi/abs/10.1126/science.abc8372`

[23] Mackenzie A P, Julian S R, Sinclair D C and Lin C T 1996 *Phys. Rev. B* **53**(9) 5848–5855 URL `https://link.aps.org/doi/10.1103/PhysRevB.53.5848`

[24] Gurvitch M and Fiory A T 1987 *Phys. Rev. Lett.* **59**(12) 1337–1340 URL `https://link.aps.org/doi/10.1103/PhysRevLett.59.1337`

[25] Allen P B, Berger H, Chauvet O, Forro L, Jarlborg T, Junod A, Revaz B and Santi G 1996 *Phys. Rev. B* **53**(8) 4393–4398 URL `https://link.aps.org/doi/10.1103/PhysRevB.53.4393`

[26] Grigera S A, Perry R S, Schofield A J, Chiao M, Julian S R, Lonzarich G G, Ikeda S I, Maeno Y, Millis A J and Mackenzie A P 2001 *Science* **294** 329–332 (*Preprint* `https://www.science.org/doi/pdf/10.1126/science.1063539`) URL `https://www.science.org/doi/abs/10.1126/science.1063539`

[27] Custers J, Gegenwart P, Geibel C, Steglich F, Coleman P and Paschen S 2010 *Phys. Rev. Lett.* **104**(18) 186402 URL `https://link.aps.org/doi/10.1103/PhysRevLett.104.186402`

[28] Steglich F, Aarts J, Bredl C D, Lieke W, Meschede D, Franz W and Schäfer H 1979 *Phys. Rev. Lett.* **43**(25) 1892–1896 URL https://link.aps.org/doi/10.1103/PhysRevLett.43.1892

[29] Varma C M, Littlewood P B, Schmitt-Rink S, Abrahams E and Ruckenstein A E 1989 *Phys. Rev. Lett.* **63**(18) 1996–1999 URL https://link.aps.org/doi/10.1103/PhysRevLett.63.1996

[30] Huang E W, Sheppard R, Moritz B and Devereaux T P 2019 *Science* **366** 987–990 (*Preprint* https://www.science.org/doi/pdf/10.1126/science.aau7063) URL https://www.science.org/doi/abs/10.1126/science.aau7063

[31] Einstein A 1905 Investigations on the theory of the brownian movement

[32] Johnson J B 1928 *Phys. Rev.* **32**(1) 97–109 URL https://link.aps.org/doi/10.1103/PhysRev.32.97

[33] Nyquist H 1928 *Phys. Rev.* **32**(1) 110–113 URL https://link.aps.org/doi/10.1103/PhysRev.32.110

[34] Wellstood F C, Urbina C and Clarke J 1994 *Phys. Rev. B* **49**(9) 5942–5955 URL https://link.aps.org/doi/10.1103/PhysRevB.49.5942

[35] Henny M, Birk H, Huber R, Strunk C, Bachtold A, Krüger M and Schönenberger C 1997 *Applied Physics Letters* **71** 773–775 ISSN 0003-6951 (*Preprint* https://pubs.aip.org/aip/apl/article-pdf/71/6/773/18528415/773_1_online.pdf) URL https://doi.org/10.1063/1.119641

[36] Henny M, Oberholzer S, Strunk C and Schönenberger C 1999 *Phys. Rev. B* **59**(4) 2871–2880 URL https://link.aps.org/doi/10.1103/PhysRevB.59.2871

[37] Johnson J B 1925 *Phys. Rev.* **26**(1) 71–85 URL https://link.aps.org/doi/10.1103/PhysRev.26.71

[38] Schottky W 1926 *Phys. Rev.* **28**(6) 1331–1331 URL https://link.aps.org/doi/10.1103/PhysRev.28.1331

[39] Johnson J B 1927 *Nature* **119**(2984) 50–51 URL https://doi.org/10.1038/119050c0

[40] Christensen C J and Pearson G L 1936 *Bell System Technical Journal* **15** 197–223 (*Preprint* https://onlinelibrary.wiley.com/doi/pdf/10.1002/j.1538-7305.1936.tb00730.x) URL https://onlinelibrary.wiley.com/doi/abs/10.1002/j.1538-7305.1936.tb00730.x

[41] Kogan S 1996 *Electronic Noise and Fluctuations in Solids* (Cambridge University Press)

[42] Vande Voorde P and Love W F 1981 *Phys. Rev. B* **24**(8) 4781–4786 URL https://link.aps.org/doi/10.1103/PhysRevB.24.4781

[43] Hooge F 1969 *Physics Letters A* **29** 139–140 ISSN 0375-9601 URL https://www.sciencedirect.com/science/article/pii/0375960169900760

[44] Maple T G, Bess L and Gebbie H A 1955 *Journal of Applied Physics* **26** 490–491 ISSN 0021-8979 (*Preprint* https://pubs.aip.org/aip/jap/article-pdf/26/4/490/18314454/490_1_online.pdf) URL https://doi.org/10.1063/1.1722025

[45] Noble V E and Thomas Jr J E 1961 *Journal of Applied Physics* **32** 1709–1714

[46] McWhorter A 1957 *Semiconductor surface physics* 207–228

[47] Dutta P, Dimon P and Horn P M 1979 *Phys. Rev. Lett.* **43**(9) 646–649 URL https://link.aps.org/doi/10.1103/PhysRevLett.43.646

[48] Weissman M B 1988 *Rev. Mod. Phys.* **60**(2) 537–571 URL https://link.aps.org/doi/10.1103/RevModPhys.60.537

[49] Sandén M, Malm B, Grahn J V and Östling M 2000 *Microelectronics Reliability* **40** 1863–1867 ISSN 0026-2714 URL https://www.sciencedirect.com/science/article/pii/S0026271400000524

[50] Paladino E, Galperin Y M, Falci G and Altshuler B L 2014 *Rev. Mod. Phys.* **86**(2) 361–418 URL https://link.aps.org/doi/10.1103/RevModPhys.86.361

[51] Schottky W 1918 *Annalen der Physik* **362** 541–567 (*Preprint* https://onlinelibrary.wiley.com/doi/pdf/10.1002/andp.19183622304) URL https://onlinelibrary.wiley.com/doi/abs/10.1002/andp.19183622304

[52] Poisson S D 1837 *Recherches sur la probabilité des jugements en matière criminelle et en matière civile* (Bachelier)

[53] Rice F 2016 *American Journal of Physics* **84** 44–51 ISSN 0002-9505 (*Preprint* https://pubs.aip.org/aapt/ajp/article-pdf/84/1/44/13067649/44_1_online.pdf) URL https://doi.org/10.1119/1.4934706

[54] Fano U 1947 *Phys. Rev.* **72**(1) 26–29 URL https://link.aps.org/doi/10.1103/PhysRev.72.26

[55] Steinbach A H, Martinis J M and Devoret M H 1996 *Phys. Rev. Lett.* **76**(20) 3806–3809 URL https://link.aps.org/doi/10.1103/PhysRevLett.76.3806

[56] Nagaev K 1992 *Physics Letters A* **169** 103–107 ISSN 0375-9601 URL https://www.sciencedirect.com/science/article/pii/0375960192908143

[57] Beenakker C W J and Büttiker M 1992 *Phys. Rev. B* **46**(3) 1889–1892 URL https://link.aps.org/doi/10.1103/PhysRevB.46.1889

[58] Nagaev K E 1995 *Phys. Rev. B* **52**(7) 4740–4743 URL https://link.aps.org/doi/10.1103/PhysRevB.52.4740

[59] MicroChem 2019 *PMMA data sheet* URL https://kayakuam.com/wp-content/uploads/2019/09/PMMA_Data_Sheet.pdf

[60] Roberts S 2024 Using wecas for elionix ebl cad file conversion and considerations for choosing write parameters Tech. rep. Nanofabrication Facility Advanced Science Research Center URL https://asrc.gc.cuny.edu/wp-content/uploads/media/global-assets/2024_03_29_Wecas_Elionix_CAD_Conversion_Training.pdf

[61] Bashir A, Awan T I, Tehseen A, Tahir M B and Ijaz M 2020 Chapter 3 - interfaces and surfaces *Chemistry of Nanomaterials* ed Awan T I, Bashir A and Tehseen A (Elsevier) pp 51–87 ISBN 978-0-12-818908-5 URL https://doi.org/10.1016/B978-0-12-818908-5.00003-2

[62] Zafar M S, Farooq I, Awais M, Najeeb S, Khurshid Z and Zohaib S 2019 Chapter 11 - bioactive surface coatings for enhancing osseointegration of dental implants *Biomedical, Therapeutic and Clinical Applications of Bioactive Glasses* Woodhead Publishing Series in Biomaterials ed Kaur G (Woodhead Publishing) pp 313–329 ISBN 978-0-08-102196-5 URL https://doi.org/10.1016/B978-0-08-102196-5.00011-2

[63] Li X, Chan K Y and Ramer R 2018 *Micromachines* **9** ISSN 2072-666X URL https://www.mdpi.com/2072-666X/9/3/138

[64] Plasma-Therm 2020 Understanding dc bias accessed: 8 November 2024 URL https://corial.plasmatherm.com/en/blog/understanding-dc-bias

[65] der Pauw L J V 1958 *Philips Res. Rep.* **13** 1–9

[66] der Pauw L J V 1958 *Philips Tech. Rev.* **20** 220–224

[67] Cieśliński J L 2012 *Thin Solid Films* **522** 314–317 ISSN 0040-6090 eMRS 2011 symp Q URL https://www.sciencedirect.com/science/article/pii/S0040609012011327

[68] van Delft D and Kes P 2010 *Physics Today* **63** 38–43 ISSN 0031-9228 (*Preprint* https://pubs.aip.org/physicstoday/article-pdf/63/9/38/9879861/38_1_online.pdf) URL https://doi.org/10.1063/1.3490499

[69] Chen L, Lowder D T, Bakali E, Andrews A M, Schrenk W, Waas M, Svagera R, Eguchi G, Prochaska L, Wang Y, Setty C, Sur S, Si Q, Paschen S and Natelson D 2023 *Science* **382** 907–911 (*Preprint* https://www.science.org/doi/pdf/10.1126/science.abq6100) URL https://www.science.org/doi/abs/10.1126/science.abq6100

[70] Zhou P, Chen L, Liu Y, Sochnikov I, Bollinger A T, Han M G, Zhu Y, He X, Božoviȁ I and Natelson D 2019 *Nature* **572** 493–496 ISSN 1476-4687 publisher: Nature Publishing Group URL `https://www.nature.com/articles/s41586-019-1486-7`

[71] Sampietro M, Fasoli L and Ferrari G 1999 *Review of Scientific Instruments* **70** 2520–2525 ISSN 0034-6748 (*Preprint* `https://pubs.aip.org/aip/rsi/article-pdf/70/5/2520/19091402/2520_1_online.pdf`) URL `https://doi.org/10.1063/1.1149785`

[72] Havinga E E, Buschow K H J and van Daal H J 1973 *Solid State Communications* **13** 621–627 ISSN 0038-1098 URL `https://www.sciencedirect.com/science/article/pii/S0038109873800262`

[73] van Daal H J, van Aken P B and Buschow K H J 1974 *Physics Letters A* **49** 246–248 ISSN 0375-9601 URL `https://www.sciencedirect.com/science/article/pii/0375960174908706`

[74] Cornelius A L, Lawrence J M, Ebihara T, Riseborough P S, Booth C H, Hundley M F, Pagliuso P G, Sarrao J L, Thompson J D, Jung M H, Lacerda A H and Kwei G H 2002 *Physical Review Letters* **88** 117201 ISSN 0031-9007, 1079-7114 URL `https://link.aps.org/doi/10.1103/PhysRevLett.88.117201`

[75] Chatterjee S, Sung S H, Baek D J, Kourkoutis L F, Schlom D G and Shen K M 2016 *Journal of Applied Physics* **120** 035105 ISSN 0021-8979 URL `https://doi.org/10.1063/1.4958336`

[76] Barbalas D, Chatterjee S, Schlom D G, Shen K M and Armitage N P 2021 *The European Physical Journal B* **94** 186 ISSN 1434-6036 URL `https://doi.org/10.1140/epjb/s10051-021-00191-y`

[77] Liang J, Fan D, Jiang P, Liu H and Zhao W 2017 *Intermetallics* **87** 27–30 ISSN 0966-9795 URL `https://www.sciencedirect.com/science/article/pii/S0966979516305805`

[78] Christianson A D, Fanelli V R, Lindsay L, Mu S, Rahn M C, Mazzone D G, Said A H, Ronning F, Bauer E D and Lawrence J M 2020 *Physical Review B* **102** 205135 publisher: American Physical Society URL `https://link.aps.org/doi/10.1103/PhysRevB.102.205135`

[79] Bud'ko S L, Frederick J C, Mun E D, Canfield P C and Schmiedeshoff G M 2007 *Journal of Physics: Condensed Matter* **20** 025220 URL `https://dx.doi.org/10.1088/0953-8984/20/02/025220`

[80] Kim J, Kang J S, Kang C J and Min B I 2023 *Phys. Rev. B* **107**(11) 115157 URL `https://link.aps.org/doi/10.1103/PhysRevB.107.115157`

[81] Ebihara T, Uji S, Terakura C, Terashima T, Yamamoto E, Haga Y, Inada Y and Onuki Y 2000 *Physica B: Condensed Matter* **281-282** 754–755 ISSN 0921-4526 URL `https://www.sciencedirect.com/science/article/pii/S0921452699009825`

[82] Demsar J, Kabanov V V, Alexandrov A S, Lee H J, Bauer E D, Sarrao J L and Taylor A J 2009 *Phys. Rev. B* **80**(8) 085121 URL `https://link.aps.org/doi/10.1103/PhysRevB.80.085121`

[83] Lowder D, Eichmann G, Wan Y, Rao K, Xie R, Zhang H, Chatterjee S, Shen K, Morosan E and Natelson D 2025 Quasiparticle properties below coherence onset in ybAl$_3$ nanostructures *In Submission*

[84] Imry Y 2002 *Introduction to Mesoscopic Physics* second edition, second edition ed Mesoscopic Physics and Nanotechnology (Oxford, New York: Oxford University Press) ISBN 978-0-19-850738-3

[85] Rowe D M, Kuznetsov V L, Kuznetsova L A and Min G 2002 *Journal of Physics D: Applied Physics* **35** 2183 URL `https://dx.doi.org/10.1088/0022-3727/35/17/315`

[86] Jung M H, Lawrence J M, Ebihara T, Hundley M F and Lacerda A H 2002 *Physica B: Condensed Matter* **312-313** 354–355 ISSN 0921-4526 the International Conference on Strongly Correlated Electron Systems URL `https://www.sciencedirect.com/science/article/pii/S0921452601011206`

[87] Hikami S, Larkin A I and Nagaoka Y 1980 *Progress of Theoretical Physics* **63** 707–710 ISSN 0033-068X URL `https://doi.org/10.1143/PTP.63.707`

[88] Bergmann G 1983 *Phys. Rev. B* **28**(2) 515–522 URL `https://link.aps.org/doi/10.1103/PhysRevB.28.515`

[89] Pierre F and Birge N O 2002 *Phys. Rev. Lett.* **89**(20) 206804 URL `https://link.aps.org/doi/10.1103/PhysRevLett.89.206804`

[90] Pierre F, Gougam A B, Anthore A, Pothier H, Esteve D and Birge N O 2003 *Phys. Rev. B* **68**(8) 085413 URL `https://link.aps.org/doi/10.1103/PhysRevB.68.085413`

[91] Lundeberg M B, Renard J and Folk J A 2012 *Phys. Rev. B* **86**(20) 205413 URL `https://link.aps.org/doi/10.1103/PhysRevB.86.205413`

[92] Sa B, Zhou J and Sun Z 2012 *Intermetallics* **22** 92–98 ISSN 0966-9795 URL `https://www.sciencedirect.com/science/article/pii/S0966979511003621`

[93] Očko M, Žonja S, Aviani I, Bauer E and Sarrao J 2011 *Journal of Alloys and Compounds* **509** 6999–7003 ISSN 0925-8388 URL `https://www.sciencedirect.com/science/article/pii/S0925838811008942`

[94] Allen J W and Martin R M 1982 *Phys. Rev. Lett.* **49**(15) 1106–1110 URL https://link.aps.org/doi/10.1103/PhysRevLett.49.1106

[95] Allen J W and Liu L Z 1992 *Phys. Rev. B* **46**(9) 5047–5054 URL https://link.aps.org/doi/10.1103/PhysRevB.46.5047

[96] Mazzone D G, Dzero M, Abeykoon A M, Yamaoka H, Ishii H, Hiraoka N, Rueff J P, Ablett J M, Imura K, Suzuki H S, Hancock J N and Jarrige I 2020 *Phys. Rev. Lett.* **124**(12) 125701 URL https://link.aps.org/doi/10.1103/PhysRevLett.124.125701

[97] Haule K and Birol T 2015 *Phys. Rev. Lett.* **115**(25) 256402 URL https://link.aps.org/doi/10.1103/PhysRevLett.115.256402

[98] Haule K, Yee C H and Kim K 2010 *Phys. Rev. B* **81**(19) 195107 URL https://link.aps.org/doi/10.1103/PhysRevB.81.195107

[99] Haule K DFT +embedded DMFT Functional Tutorials URL http://hauleweb.rutgers.edu/tutorials/

[100] Singh D J and Nordström L 2006 *Planewaves, Pseudopotentials and the LAPW Method* (Springer US) ISBN 978-0-387-28780-5 URL http://link.springer.com/10.1007/978-0-387-29684-5

[101] Abramovitch D J, Coulter J, Beck S and Millis A 2025 Electron-phonon coupling in correlated metals: A dynamical mean-field theory study (*Preprint* 2505.03958) URL https://arxiv.org/abs/2505.03958

[102] Chatterjee S, Ruf J P, Wei H I, Finkelstein K D, Schlom D G and Shen K M 2017 *Nature Communications* **8** 852 ISSN 2041-1723 publisher: Nature Publishing Group URL https://www.nature.com/articles/s41467-017-00946-1

[103] Čermák P, Schneidewind A, Liu B, Koza M M, Franz C, Schönmann R, Sobolev O and Pfleiderer C 2019 *Proceedings of the National Academy of Sciences* **116** 6695–6700 publisher: Proceedings of the National Academy of Sciences URL https://www.pnas.org/doi/full/10.1073/pnas.1819664116

[104] Paschen S, Friedemann S, Wirth S, Steglich F, Kirchner S and Si Q 2016 *Journal of Magnetism and Magnetic Materials* **400** 17–22 ISSN 0304-8853 proceedings of the 20th International Conference on Magnetism (Barcelona) 5-10 July 2015 URL https://www.sciencedirect.com/science/article/pii/S030488531530559X

[105] Gegenwart P, Westerkamp T, Krellner C, Tokiwa Y, Paschen S, Geibel C, Steglich F, Abrahams E and Si Q 2007 *Science* **315** 969–971 (*Preprint* https://www.science.org/doi/pdf/10.1126/science.1136020) URL https://www.science.org/doi/abs/10.1126/science.1136020

[106] Custers J, Gegenwart P, Neumaier K, Wilhelm H, Oeschler N, Ishida K, Kitaoka Y, Geibel C and Steglich F 2003 *Journal of Physics: Condensed Matter* **15** S2047 URL https://dx.doi.org/10.1088/0953-8984/15/28/324

[107] Trovarelli O, Geibel C, Mederle S, Langhammer C, Grosche F M, Gegenwart P, Lang M, Sparn G and Steglich F 2000 *Phys. Rev. Lett.* **85**(3) 626–629 URL https://link.aps.org/doi/10.1103/PhysRevLett.85.626

[108] Nguyen D, Sidorenko A, Taupin M, Knebel G, Lapertot G, Schuberth E and Paschen S 2021 *Nat Commun* **12**

[109] Custers J, Gegenwart P, Wilhelm H, Neumaier K, Tokiwa Y, Trovarelli O, Geibel C, Steglich F, Pèpin C and Coleman P 2003 *Nature* **424** 524–527

[110] Paschen S, Lühmann T, Wirth S, Gegenwart P, Trovarelli O, Geibel C, Steglich F, Coleman P and Si Q 2004 *Nature* **432** 881–885

[111] Gegenwart P, Custers J, Geibel C, Neumaier K, Tayama T, Tenya K, Trovarelli O and Steglich F 2002 *Phys. Rev. Lett.* **89**(5) 056402 URL https://link.aps.org/doi/10.1103/PhysRevLett.89.056402

[112] de Picciotto R, Reznikov M, Heiblum M, Umansky V, Bunin G and Mahalu D 1997 *Nature* **389** 162–167

[113] Saminadayar L, Glattli D C, Jin Y and Etienne B 1997 *Phys. Rev. Lett.* **79**(13) 2526–2529 URL https://link.aps.org/doi/10.1103/PhysRevLett.79.2526

[114] Delattre T, Feuillet-Palma C, Herrmann L G, Morfin P, Berrior J M, Fève G, Plaçais B, Glatti D C, Choi M S, Mora C and Kontos T 2009 *Nature Phys* **5** 208–212

[115] Zarchin O, Zaffalon M, Heiblum M, Mahalu D and Umansky V 2008 *Phys. Rev. B* **77**(24) 241303 URL https://link.aps.org/doi/10.1103/PhysRevB.77.241303

[116] Bastiaans K M, Chatzopoulos D, Ge J F, Cho D, Tromp W O, van Ruitenbeek J M, Fischer M H, de Visser P J, Thoen D J, Driessen E F C, Klapwijk T M and Allan M P 2021 *Science* **374** 608–611 (*Preprint* https://www.science.org/doi/pdf/10.1126/science.abe3987) URL https://www.science.org/doi/abs/10.1126/science.abe3987

[117] Prochaska L, Li X, MacFarland D C, Andrews A M, Bonta M, Bianco E F, Yazdi S, Schrenk W, Detz H, Limbeck A, Si Q, Ringe E, Strasser G, Kono J and Paschen S 2020 *Science* **367** 285–288 (*Preprint* https://www.science.org/doi/pdf/10.1126/science.aag1595) URL https://www.science.org/doi/abs/10.1126/science.aag1595

[118] Bakali E, Artner W, Beiser M, Bernardi J, Detz H, Eguchi G, Foelske A, Giparakis M, Herzig C, Limbeck A, Nguyen H, Prochaska L, Prokofiev A, Sauer M, Schwarz S, Schrenk W, Strasser G, Svagera R, Taupin M, Thirsfeld A, Waas M, Yan X, Zocco D, Andrews A and Paschen S 2022 *Journal of Crystal Growth* **595** 126804 ISSN 0022-0248 URL `https://www.sciencedirect.com/science/article/pii/S0022024822002895`

[119] Wu Y M, Yu J J and Raghu S 2024 *Phys. Rev. B* **110**(23) 235157 URL `https://link.aps.org/doi/10.1103/PhysRevB.110.235157`

[120] Fang Y, Mahankali M, Chen Y W L, Hu H, silke Paschen and Si Q 2025 *Nat Commun* **16** 2498

[121] Gegenwart P, Westerkamp T, Krellner C, Brando M, Tokiwa Y, Geibel C and Steglich F 2008 *Physica B: Condensed Matter* **403** 1184–1188 ISSN 0921-4526 URL `https://www.sciencedirect.com/science/article/pii/S0921452607010897`

[122] Ruddlesden S and Popper P 1957 *Acta Cryst* **10** 538–539

[123] Lester C, Ramos S, Perry R, Croft T, Laver M, Bewley R, Guidi T, Hiess A, Wildes A, Forgan E and Hayden S 2021 **12**

[124] Tamai A, Allan M P, Mercure J F, Meevasana W, Dunkel R, Lu D H, Perry R S, Mackenzie A P, Singh D J, Shen Z X and Baumberger F 2008 *Phys. Rev. Lett.* **101**(2) 026407 URL `https://link.aps.org/doi/10.1103/PhysRevLett.101.026407`

[125] Ohnishi T and Takada K 2011 *Applied Physics Express* **4** 025501 URL `https://dx.doi.org/10.1143/APEX.4.025501`

[126] Marshall P B, Kim H, Ahadi K and Stemmer S 2017 *APL Materials* **5** 096101 ISSN 2166-532X (*Preprint* `https://pubs.aip.org/aip/apm/article-pdf/doi/10.1063/1.4998772/14559614/096101_1_online.pdf`) URL `https://doi.org/10.1063/1.4998772`

[127] Kim J, Mun J, Palomares García C M, Kim B, Perry R S, Jo Y, Im H, Lee H G, Ko E K, Chang S H, Chung S B, Kim M, Robinson J W A, Yonezawa S, Maeno Y, Wang L and Noh T W 2021 *Nano Letters* **21** 4185–4192

[128] Noh T and Kim J 2022 Private communication

[129] Jones G A C, Blythe S and Ahmed H 1987 *J. Vac. Sci. Technol. B* **5** 120–123 ISSN 0734-211X URL `https://doi.org/10.1116/1.583844`

[130] 2023 UV Lithography and Semiconductor Industry URL `https://www.boydcorp.com/blog/uv-lithograph-and-seimconductor-industry.html`

[131] Shi L Y, Tagay Z, Liang J, Duong K, Wu Y, Ronning F, Schlom D G, Shen K M and Armitage N P 2025 Low energy electrodynamics and a hidden fermi liquid in the heavy-fermion cecoin$_5$ (*Preprint* 2310.10916) URL https://arxiv.org/abs/2310.10916

[132] Petrovic C, Pagliuso P G, Hundley M F, Movshovich R, Sarrao J L, Thompson J D, Fisk Z and Monthoux P 2001 *Journal of Physics: Condensed Matter* **13** L337 URL https://dx.doi.org/10.1088/0953-8984/13/17/103

[133] Jiang X, Qin M, Wei X, Xu L, Ke J, Zhu H, Zhang R, Zhao Z, Liang Q, Wei Z, Lin Z, Feng Z, Chen F, Xiong P, Yuan J, Zhu B, Li Y, Xi C, Wang Z, Yang M, Wang J, Xiang T, Hu J, Jiang K, Chen Q, Jin K and Zhao Z 2023 *Nature Physics* **19** 365–371 ISSN 1745-2481 publisher: Nature Publishing Group URL https://www.nature.com/articles/s41567-022-01894-4

Future Projects

Following the works covered in this thesis there are several other materials that would be interesting to study. Target materials are those that experience strange metallicity and heavy fermionic behavior. To that end the difficulty in doing these measurements lies in work done to grow thin films of these materials. Examples of currently available thin films include $CeCoIn_5$ and FeSe and both will be covered in more detail.

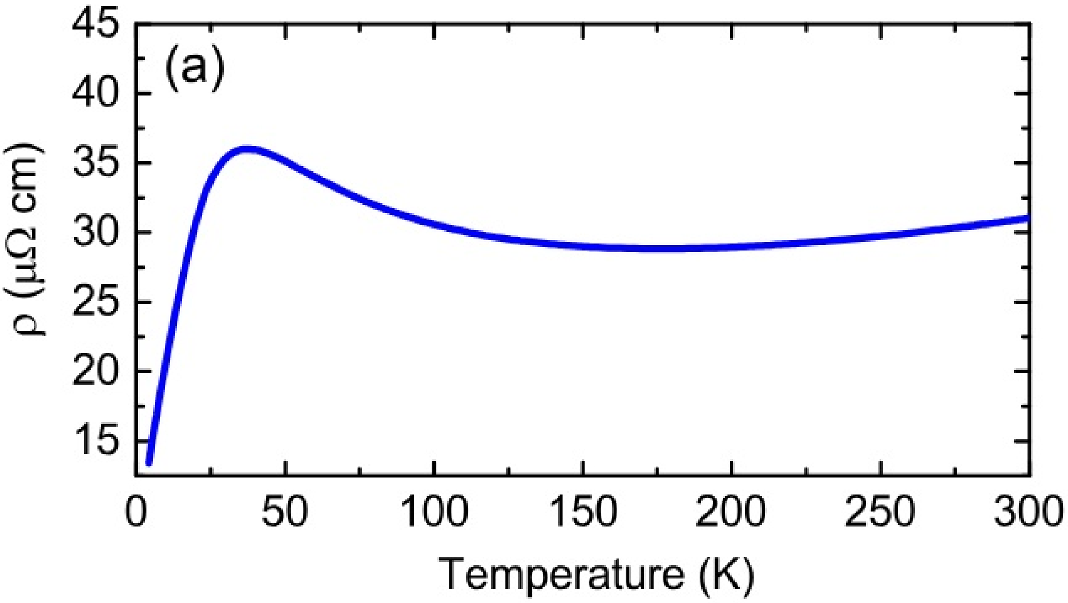

Figure A.1 : Resistivity vs. temperature of $CeCoIn_5$ showcasing the strange metal behavior below $T \approx 40$ K.
[131, Reproduced]

$CeCoIn_5$ (CCI) is an heavy fermion material that displaces unconventional superconductivity. It has been studied as a material that displays both superconductivity and QCP resulting in NFL behavior observed above the superconducting dome[131]. The superconducting onset temperature is $T_c = 2.3$ K[132] and a Kondo coherence temperature $T^* \approx 40$ K[131].

Its been in thin film form for several years and fairly recently Kyle Shen's group, who provided the $YbAl_3$ films, has published a paper on the growth of CCI films[131]. Studying CCI serves as continuation of the YRS study of a strange metal to probe the mechanisms of strange metallicity and seeks for a universal explanation by use of various examples.

FeSe is another unconventional superconductor that displays strange metallicity above the superconducting transition. FeSe displays a gate-tunable transition dependence that can tune the superconducting transition to access the strange metal behavior at lower temperature more appropriate for the noise measurements[133].

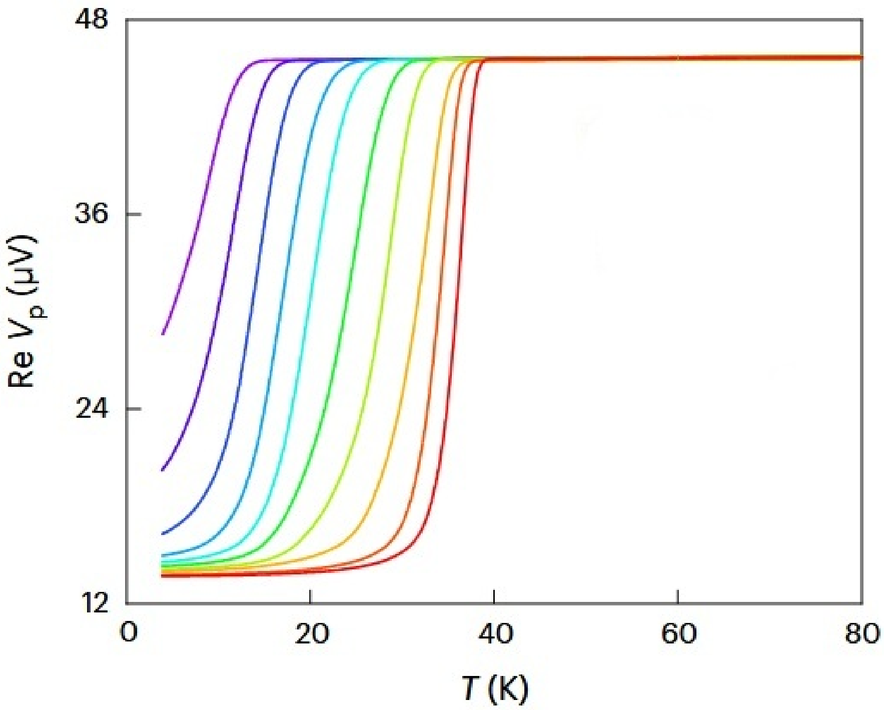

Figure A.2 : Voltage vs. temperature showcasing shifting of the superconducting transition of FeSe.

[133, Adapted]

Thin films have been grown by Nitin Samarth's group? and have been received to study this strange metal state.

Examples of useful materials to perform these studies on aren't limited to these alone. As mentioned previously the limiting factor on studies of these strongly correlated materials is more often than not is the lack of thin films available. As growth techniques and interest grows of mesoscale structures more opportunities of interesting materials will appear.

Noise Data Analysis

It is useful to cover generically how analysis of noise measurements are done in detail from the raw data taken to the actual analysis seen in $\mathrm{YbAl_3}$ and YRS. The methods will be explained generically with the specific examples of shot noise and the Γ calculations in terms of analysis given more detail as an example of two different methods of analysis.

Firstly it's useful to briefly reiterate the raw data conversion mentioned in Section 5.3.2 for a full explanation of analysis. The raw noise data recorded needs to be converted into real voltage noise data. This is done via a previously done calibration that accounts for background noise and the real gain of the system. Notably in certain situations a new calibration may need to be done in cases were the in series resistances used in the filters for applying bias become comparable to the device resistance, due to load affecting the actual gain of the amplifiers. In these situations there are two options available that work: increase the series resistances to at least an order of magnitude greater and redo the calibration with these new resistors or to simply redo a calibration on the device being measured by doing zero bias noise measurements at several temperatures with the highest temperature data point being > 200 K.

Alongside calibration and usually in the same or previous step the data needs to checked to find a flatband frequency range, usually as large of a region possible between $1/f$ and RC rolloff or any large artifact frequency. From the “flat” region there will be many peaks associated with 60 Hz frequency that need to be removed. This is done by removing all multiples of 60 from the data as well as the data point just before and after the 60 Hz peak via modulo 55 and 5 respectively. Any additional peaked regions can either be excluded from the white spectra assuming $\Delta f_{peak} \ll \Delta f_{region}$ or the peak will just become the new edge of a region if it is to large to reasonably remove.

With a flatband defined and the data properly converted into voltage noise it now needs to be averaged into a single point. Standard error is recorded alongside this for proper error management. This is repeated for every run and every voltage. All runs at the same voltage can then be further averaged together with an weighted average to account for outlier runs that had spurious peaks or unusual increases. This gives the voltage noise at each V value for analysis of trends in the noise data.

The shot noise analysis from her involves converting the voltage noise data at each V into current noise using previously recorded dV/dI data. At each V value the differential resistance needs to be found an applied to get current noise as seen applied to Eq. 4.1. The curent noise can then be taken as a function of applied current, the recorded applied voltage divided by the total resistance, and the Fano factor can then be found by fitting to Eq. 4.30.

The Γ calculations are done in a slightly different way do to the different nature of the equation. Here the voltage noise is used as a function of applied voltage to the device. The data can't be simply fitted as in the shot noise example due to having to solve the differential equation, or ideally a 5th order polynomial, seen in Eq. 4.4. A Γ has to be guessed and plugged into the equation to generate a temperature profile along the wire of the $T_e(x)$. The temperature profile is then used in conjunction with $R(T)$ data to generate a simulated JN noise as a function of V to compare to the data. Γ is swept through a range of values and can be made to determine the best fit by minimization of χ^2 between the observations O and the calculated values C with respect to the variance in the data σ.

$$\chi^2 = \sum_i \frac{(O_i - C_i)^2}{\sigma_i} \tag{B.1}$$

Following this procedure allows for proper analysis and error propagation of raw noise data taken.

Step-by-Step Noise Data Collection

This chapter covers the procedure to generically collect the noise data used in this thesis. It begins by assuming a relevant device has been inserted into the PPMS via the noise probe and the system is sat at room temperature.

1. Connection needs to be made to breakout box for the PPMS. Care should be taken to not accidentally blow up devices via static discharge. Sensitivity will heavily depend on the devices being measured and resistances.

2. Before beginning noise measurement ensure that there is plenty of room on the drive for all the data intended to be taken. Noise data files are ≈ 30 MB each and add up quickly. For example a common data collection includes ~ 7 runs at 11 biases including zero. This gives a folder size of 2.3 GB at a given temperature and field. If resistances are lower even more runs will be needed to give good data.

3. Prior to noise measurement two measurements need to be done to ensure the device is in good condition, will survive the biases applied during noise measurement, and are necessary for analysis after measurement

    (a) First the device should be cooled to ≈ 3 K while measuring Resistance. For subsequent devices its recommended to at least get $R\mathrm{v}T$ data up to at least 20-30 K depending on maximum temperature range.

    (b) Once at base temperature it's important that for every temperature for which noise will be measured a dI/dV v V curve is taken up or greater than the range of bias intended to apply to the device during noise measurement. Important to know differential resistance at each V noise is taken for analysis.

4. Relevant files should be opened for testing. The LabVIEW code which controls the noise data collection should be defined in Python code. This is true for all the Python codes and the LabVIEW codes should always be opened when in use to prevent errors. Additionally at times when a quick look in spectra is desired one can open the Picoscope software to look at the oscilloscope outputs. IMPORTANT: do NOT keep Picoscope software open when using the noise measurement LabVIEW code. Be very careful to not save or edit the noise measurement code without ensuring a backup.

5. Initial noise measurements at zero bias should be done to ensure that the spectra doesn't contain any spurious peaks

    (a) If there are spurious peaks it's good to compare to previous measurements to see if these are common peaks (such as 60 Hz). If the peaks are unique its useful to attempt to figure out if its resulting from the sample (has been seen in graphene and Josephson junctions) or something that has changed in the environment.

    (b) To test if it results from the environment it's useful to have a resistor in a box that has comparable noise value of the device (RT is the same). If it is present then its resulting from the environment and it will have to be located via systematic searching.

6. Once the spectra look good do a single run up to the highest bias and ensure the noise looks as expected. In general should see and increase of noise with bias.

7. If the spectra still looks and behaves well then Python code can be used to iterate through voltages, runs, fields, and/or temperatures. It is important to coordinate with the PPMS control computer as the data taking computer only reads temperature and field for the control computer. Time coordination

are necessary to determine how long to sit at a given temperature/field. This time can be estimated by seeing how long a single data collection takes and multiplying that time by the number of runs and biases being done and adding in any waits in the python code. Times should be given an additional buffer of 200-500 s to account for any unexpected pauses.

8. Data collection will take multiple days. It is heavily encouraged to periodically pull data out and check to make sure no errors have occurred. It is recommended to at least do this every temperature/field.

9. Following completion of data collection double check data and warmup device to remove from the PPMS taking as much care as when putting it in.